



POLITECNICO DI TORINO
Repository ISTITUZIONALE

Automated Strategies in Multimodal and Multidimensional Ultrasound Image-based Diagnosis

Original

Automated Strategies in Multimodal and Multidimensional Ultrasound Image-based Diagnosis / Caresio, Cristina. - (2018 Mar 15).

Availability:

This version is available at: 11583/2703644 since: 2018-03-16T15:32:03Z

Publisher:

Politecnico di Torino

Published

DOI:10.6092/polito/porto/2703644

Terms of use:

openAccess

This article is made available under terms and conditions as specified in the corresponding bibliographic description in the repository

Publisher copyright

(Article begins on next page)



ScuDo
Scuola di Dottorato ~ Doctoral School
WHAT YOU ARE, TAKES YOU FAR

Doctoral Dissertation
Doctoral Program in Bioengineering and Medical-Surgical Sciences (30th Cycle)

Automated strategies in multimodal and multidimensional ultrasound image-based diagnosis

Cristina Caresio

Supervisor:
Prof. F. Molinari

Doctoral Examination Committee:
Prof. C. Corsi, Referee, University of Bologna
Prof. O. Basset, Referee, University of Lyon

Politecnico di Torino
2018

Declaration

I hereby declare that, the contents and organization of this dissertation constitute my own original work and does not compromise in any way the rights of third parties, including those relating to the security of personal data.

Cristina Caresio

2018

* This dissertation is presented in partial fulfillment of the requirements for **Ph.D. degree** in the Graduate School of Politecnico di Torino (ScuDo).

Mens agitat molem.

(Virgilio, Eneide, VI, 7)

Abstract

Medical ultrasonography is an effective technique in traditional anatomical and functional diagnosis. However, it requires the visual examination by experienced clinicians, which is a laborious, time consuming and highly subjective procedure. Computer aided diagnosis (CADx) have been extensively used in clinical practice to support the interpretation of images; nevertheless, current ultrasound CADx still entail a substantial user-dependency and are unable to extract *image data* for prediction modeling.

The aim of this thesis is to propose a set of fully automated strategies to overcome the limitations of ultrasound CADx. These strategies are addressed to multiple modalities (B-Mode, Contrast-Enhanced Ultrasound-CEUS, Power Doppler-PDUS and Acoustic Angiography-AA) and dimensions (2-D and 3-D imaging). The enabling techniques presented in this work are designed, developed and quantitatively validated to efficiently improve the overall patients' diagnosis.

This work is subdivided in 2 macro-sections: in the first part, two fully automated algorithms for the reliable quantification of 2-D B-Mode ultrasound skeletal muscle architecture and morphology are proposed. In the second part, two fully automated algorithms for the objective assessment and characterization of tumors' vasculature in 3-D CEUS and PDUS thyroid tumors and preclinical AA cancer growth are presented.

In the first part, the MUSA (Muscle UltraSound Analysis) algorithm is designed to measure the muscle thickness, the fascicles length and the pennation angle; the TRAMA (TRAnsversal Muscle Analysis) algorithm is proposed to extract and analyze the Visible Cross-Sectional Area (VCSA). MUSA and TRAMA algorithms have been validated on two datasets of 200 images; automatic measurements have been compared with expert operators' manual measurements. A preliminary statistical analysis was performed to prove the ability of texture analysis on automatic VCSA in the distinction between healthy and pathological muscles.

In the second part, quantitative assessment on tumor vasculature is proposed in two automated algorithms for the objective characterization of 3-D CEUS/Power Doppler thyroid nodules and the evolution study of fibrosarcoma invasion in preclinical 3-D AA imaging.

Vasculature analysis relies on the quantification of architecture and vessels tortuosity. Vascular features obtained from CEUS and PDUS images of 20 thyroid nodules (10 benign, 10 malignant) have been used in a multivariate statistical analysis supported by histopathological results.

Vasculature parametric maps of implanted fibrosarcoma are extracted from 8 rats investigated with 3-D AA along four time points (TPs), in control and tumors areas; results have been compared with manual previous findings in a longitudinal tumor growth study.

Performance of MUSA and TRAMA algorithms results in 100% segmentation success rate. Absolute difference between manual and automatic measurements is below 2% for the muscle thickness and 4% for the VCSA (values between 5-10% are acceptable in clinical practice), suggesting that automatic and manual measurements can be used interchangeably. The texture features extraction on the automatic VCSAs reveals that texture descriptors can distinguish healthy from pathological muscles with a 100% success rate for all the four muscles.

Vascular features extracted of 20 thyroid nodules in 3-D CEUS and PDUS volumes can be used to distinguish benign from malignant tumors with 100% success rate for both ultrasound techniques. Malignant tumors present higher values of architecture and tortuosity descriptors; 3-D CEUS and PDUS imaging presents the same accuracy in the differentiation between benign and malignant nodules.

Vascular parametric maps extracted from the 8 rats along the 4 TPs in 3-D AA imaging show that parameters extracted from the control area are statistically different compared to the ones within the tumor volume. Tumor angiogenetic vessels present a smaller diameter and higher tortuosity. Tumor evolution is characterized by the significant vascular trees growth and a constant value of vessel diameter along the four TPs, confirming the previous findings.

In conclusion, the proposed automated strategies are highly performant in segmentation, features extraction, muscle disease detection and tumor vascular characterization. These techniques can be extended in the investigation of other organs, diseases and embedded in ultrasound CADx, providing a user-independent reliable diagnosis.

Contents

Chapter 1

Introduction	1
1.1 Ultrasound image-based-diagnosis.....	1
1.2 Computer-Aided Diagnosis in ultrasonography	3
1.3 Fully automated strategies in ultrasound diagnosis.....	5
1.4 Objective.....	8
1.5 Outline of the Thesis	9
1.6 References	12

Chapter 2

Automated architectural analysis in skeletal muscle ultrasound imaging	15
2.1 Introduction	16
2.2 Materials and Methods	20
2.2.1 Longitudinal Muscle Ultrasound Analysis: MUSA algorithm	20
2.2.2 Fascicles detection algorithm.....	30
2.2.3 Transversal Muscle Ultrasound Analysis: TRAMA algorithm	37
2.3 Results	50
2.3.1 Segmentation results of MUSA algorithm.....	50
2.3.2 Segmentation results of fascicles detection algorithm.....	53
2.3.3 Segmentation results of TRAMA algorithm.....	55
2.4 Discussion.....	59
2.5 Conclusion.....	61
2.2 References	62

Chapter 3

Quantitative skeletal muscle ultrasound imaging.....	67
3.1 Introduction	69
3.1 Muscle echo intensity reliability assessment on healthy controls	71
3.1.1 Materials and Methods.....	71
3.1.2 Results.....	75
3.1.3 Discussion.....	77
3.2 Quantitative muscle ultrasonography using texture analysis in healthy subjects	79
3.2.1 Materials and Methods.....	79
3.2.2 Results.....	81
3.2.2 Discussion.....	85
3.3 Quantitative muscle ultrasonography using texture analysis in healthy subjects and pathological patients	86
3.3.1 Materials and Methods.....	87
3.3.2 Results.....	89
3.3.3 Discussion.....	93
3.4 Conclusions	95
3.5 References	95

Chapter 4

Multimodal 3-D ultrasound quantitative characterization of thyroid tumors vasculature	99
4.1 Introduction	101
4.2 Materials and Methods	104
4.3 Results	117
4.4 Discussion.....	120
4.5 Conclusion.....	124
4.6 References	124

Chapter 5

Quantitative assessment of cancer growth in 3-D preclinical acoustic angiography 127

5.1 Introduction 129

5.2 Materials and Methods 132

5.2.1 Rats preparation and AA acquisition 132

5.2.2 Tumor microvasculature 3-D mapping and analysis 133

5.2.3 Statistical Analysis..... 138

5.3 Results 139

5.4 Discussion..... 143

5.5 Conclusion..... 146

5.6 References 146

Conclusions and Final Remarks 149

APPENDIX A..... 151

APPENDIX B..... 153

APPENDIX C..... 155

APPENDIX D..... 161

APPENDIX E..... 163

List of Contributions 167

Chapter 1

Introduction

1.1 Ultrasound image-based-diagnosis

Diagnostic ultrasound is a safe, effective, and non-invasive technique in the study of architecture, morphology and vasculature of soft tissues and organs in humans and animal models (from *NIH: National Institute of Biomedical Imaging and Bioengineering* <https://www.nibib.nih.gov/science-education/science-topics/ultrasound>). Ultrasound imaging implies high-frequency mechanical sound waves (above the threshold of human hearing of 20 kHz) which interact with tissues, are reflected to and then detected by the ultrasound transducer. Images are obtained from the difference of adjacent biological tissue impedance, in a way that a large difference of impedance produce higher amplitude ultrasound waves, called *echoes*.

Diagnostic ultrasound can be sub-divided into anatomical and functional imaging. Anatomical ultrasound produces images of internal organs or other structures, whereas functional ultrasound combines information of movement and velocity of tissue or blood, softness or hardness of tissues, and other physical characteristics to create “visual information maps” and investigate changes/differences in function within a structure or organ. Ultrasound assessments

can be performed using a wide variety of external (linear, convex, phased array probes) and internal transducers (transesophageal transvaginal, transrectal probes).

Thanks to its portability, convenience and the employment of non-ionizing radiations (FDA: <https://www.fda.gov/radiation-emittingproducts/radiationemittingproductsandprocedures/medicalimaging/ucml15357.htm>), ultrasound imaging is generally used in clinical practice for the evaluation, screening, diagnosis and treatment of several medical conditions. Common ultrasound procedures can be performed in different modalities (such as B-Mode, Power/Color Doppler, Contrast Enhanced imaging) and include the visualization of abdominal tissues and organs [1], [2], neck [3], breast [4], skeletal muscles [5]. Moreover, medical ultrasonography is a real-time methodology, that allows the investigation of rapid events or organs' movements, like in the case of fetal ultrasonography during pregnancy [6]–[8], fetal heart rate monitoring [9], vessels blood flow visualization [10] and echocardiography [11], [12].

Since the last two decades, traditional 2-D ultrasound imaging has been extended to the 3-D (either performed in manual or automatic scanning procedure), and, more recently, to the 4-D, namely the 3-D motion. The introduction of visualization and measurements tools integrated within ultrasound devices has considerably eased the ultrasound diagnostic procedure, giving the opportunity to revise the exam, take annotations, provide a quantitative analysis or even navigate the 3-D volumes. Nevertheless, a considerable human interaction is needed in visual examination and manual measurements; both actions require experienced users, and, due to the scale and complexity of image data, are often laborious, time consuming, highly subjective and prone of errors.

1.2 Computer-Aided Diagnosis in ultrasonography

Since 1960s, the idea of developing a computerized scheme and quantitative analysis in medical imaging that could help the radiologists in medical images visual interpretation was known and discussed in routine practice and scientific research. At that time, it was generally assumed that computers could provide an “automated diagnosis”, replacing professionals in detecting abnormalities, thanks to their ability to perform faster and more complex analyses, better than human beings. However, despite some interesting results, computer were not sufficiently powerful, advanced image-processing techniques were not available, and digital images were not easily accessible.

During 1980s, the concept of Computer-Aided Diagnosis (CADx) provided by systematic examination of large-scale data was initially introduced in relevant medical subjects, such as cardiovascular diseases [13], lung [14], [15] and breast cancers [16], to be lately extended to all other diagnostic fields; in that case, the emerging approach assumed that computer output could not substitute the radiologist’ decision, but could be used as a primary diagnosis or a second opinion.

CADx systems are based on a fundamental concept, as stated in **Computer-Aided Diagnosis in Medical Imaging: Historical Review, Current Status and Future Potential** by Doi [17]:

“Our basic strategy for development of methods and techniques for detection and quantitation of lesions in medical images has been based on the understanding of processes that would be involved in image readings by radiologists [...] We assumed that computer algorithms should be developed based on the understanding of image readings, such as how radiologists can detect certain lesions, why they may miss some abnormalities, and how they can distinguish between benign and malignant lesions.”

From this quotation, CADx development needs to meet three requirements: first, CADx should be developed following the user’s reasoning, which is based on

the experience in performing a series of supervised sequential or parallel tasks, such as information reduction, segmentation and features extraction. Second, CADx should be able to mimic the human cognitive function of recognition, with the advantage of being objective and un-biased. Lastly, CADx systems should be able to classify and distinguish a lesion or a pattern based on innumerable pre-establish rules and criteria. Regarding this last requirement, CADx must provide a significant improvement in classification performance in terms of sensitivity and specificity to be a valuable decision-support tools.

Under these assumptions, CADx have become one of the major research subjects in medical imaging and diagnostic radiology, including ultrasound imaging. While the field of medical image analysis was growing, image data sets size and methodologies/tools were developing exponentially. Several studies have suggested that the incorporating CADx into the diagnostic process can improve the performance of image diagnosis by decreasing inter-observer variation and providing the quantitative support for the clinical decision [18].

CADx are currently applied in the ultrasound detection and differential diagnosis of many different types of abnormalities in medical images, especially in the differentiation of malignancy/benignancy for tumors/lesions obtained in various examinations and in different ultrasound modalities. Ultrasound CADx have found application in liver diseases diagnosis [19], [20], in breast lesions [21], [22] thyroiditis [23] and thyroid nodules detection [24], in coronary artery disease [25], 3-D echocardiography [26] and in fetal volume measurement [27].

Regardless of the proven accuracy of the cited methodologies, CADx are not very popular in ultrasonography; in fact, this modality is highly user-dependent (there are no standard acquisition protocols), and performing image segmentation and features extraction is an arduous and challenging task [28], due to the presence of ultrasound artifacts (tissues reverberation, shadowing, air hyper-reflecting echoes) and the lower spatial resolution (compared to other diagnostic image modalities, such as Computer Tomography and Magnetic Resonance).

Ultrasound CADx still present a considerable number of weak points. In fact, CADx systems are not scalable and are single result-oriented, meaning that are designed to investigate single organs or tissue along a specific projection. Moreover, all these methods required a substantial manual operation or initialization, such as the selection of a frame, a plane and the region (ROI) or a volume of interest (VOI) where to perform the analysis. Lastly, following radiologists' lexicon, traditional CADx are unable to capture lesion heterogeneity and quantify the image "coarseness", since they are specifically designed for the extraction of *semantic attributes* (Table 1.1), namely the geometrical descriptors such as shape, size, location and tortuosity.

Semantic attributes	Agnostic texture descriptors
Shape	1 st Order Texture Statistics
Size	2 st Order Texture Statistics
Location	High-Order Texture Statistics
Tortuosity	Local Binary Patterns

Table 1. 1: Examples of semantic attributes and agnostic texture descriptors according to the differentiation of Radiomics.

1.3 Fully automated strategies in ultrasound diagnosis

In the last decade, technological and computational advances have led to the development of novel approaches in biomedical image analysis; the concept of fully automated techniques in image diagnosis have become again very popular, thanks to the introduction of new segmentation techniques [29], sophisticated pattern recognition tools and feature extraction algorithms. Those approaches go under the name of *strategies* and are designed to overcome the major limitations of traditional CADx in terms of automation, accuracy, robustness, and not as last, single result or application design-orientation and semantic attributes extraction limitation.

Image-based diagnostic strategies rely on the principle that image information can be extracted by means of a set of adaptive and scalable techniques. Each technique can be seen as a single block of processing, like an object featured by specific parameters and functions, that can be re-used in any image modality or dimension (2-D and 3-D) [30].

The usual framework is built with a sequence of blocks arranged in a pipeline and each strategy presents at least three blocks: pre-processing, segmentation, features extraction and classification. The final aim of this procedure is not only to excerpt the essential information from images, like in implicit human cognitive procedures, but also go beyond the surface and enable the conversion of images into *data*.

The pre-processing steps, in ultrasound imaging, are the most critical part in building a strategy, because all the subsequent steps directly depend on them; these steps are usually devoted to data epuration and image information reduction, such as 2-D lines of 3-D frames downsampling. Further steps of pre-processing are dedicated to image adjustment, noise reduction and artifacts identification, provided by directional filters.

Ultrasound image segmentation is then made possible with the application of single and multiscale filtering blocks, which are tailored to enhance particular structures' shapes, dimension and color intensity. This step of filtering has been shown to be extremely suitable in both 2-D and 3-D image processing because of its robustness to the residual noise. Usually, additional steps of thresholding and optimized cleaning are needed to provide the gross representation of final structures. Most of time, the segmentation needs to be guided by a *heuristic procedure*, namely “an exploratory problem solving-approach which utilizes self-education techniques, such as the evaluation of feedbacks, to improve its performance” (*source: Merriam-Webster online Dictionary*). Segmentation performance can be improved with a step of refinement, such as edges or centerline repositioning. In the case of 3-D segmentation, for example vasculature geometrical

characterization, is made possible by the application of additional steps of structure reduction, like thinning and skeletonization.

The last step of features extraction is usually applied to complete an automated strategy: common sematic features are related to shape and size (such as length, thickness, angles) and vascularity (number of 3-D structures, branching points, tortuosity), but with the high-throughput of nowadays computing, a larger number of image quantitative features can be extracted from a segmented ROI/VOI [31]. Lesions heterogeneity and coarseness can be described by the employment of *agnostic texture descriptors* (Table 1.1): these features are mathematically extracted from the image and are generally not part of the radiologists' lexicon. Agnostic features can be divided into first-, second-, or higher-order statistical outputs. First-order statistics describe the distribution of values of individual pixels/voxels without concern for spatial relationships. These are generally histogram-based methods and capture a ROI in single values for mean, standard deviation, variance, skewness (asymmetry), kurtosis (flatness) and histogram of values uniformity/randomness (entropy). Second-order statistical descriptors, firstly introduced by Haralick et al. in 1973 [32], describe the statistical interrelationships between voxels with similar (or dissimilar) contrast values. Higher-order statistical methods are able to extract repetitive or nonrepetitive patterns, such as the Run Lengths patterns proposed by Galloway in 1975 [33] or the circular Local Binary Pattern proposed by Ojala from 1996 [34], [35].

In this context, automated strategies can become the bridge technology between conventional CADx and the new concept of mineable high-dimensional data extraction, that has recently been introduced with the name of *radiomics*, and already described in **Radiomics: Images are more than pictures, they are data**, by Gillies et al [31]: in this paper, the authors claim that “biomedical images contain information that reflects underlying pathophysiology” and that “it can be revealed via quantitative image analyses”.

Radiomics is a natural extension of CADx, but unlike those systems, it provides more than a single result (such as a geometrical semantic attribute) and it is explicitly designed to extract maximal information from standard care images. Radiomics is a databases building-oriented technique in the *Big Data* framework, meaning that image data of millions of patients as well as any relevant patients' datum, will be stored, shared and subsequently mined with sophisticated bioinformatics tools to develop models that may potentially improve diagnostic, prognostic, and predictive accuracy; in few years, radiomics has already shown to be a powerful and promising tool towards the development in the field of *personalized medicine*.

Radiomics has been firstly developed in oncology and supported by many instructions and initiative (The American National Cancer Institute and the Quantitative Imaging Network); moreover, it provides quantitative image features based on intensity, shape, size and texture on tumor and intra-tumoral heterogeneity [36], [37]. Radiomics has been initially applied in tomographic tumors' studies, such as CT and MR image modalities, but it can be theoretically applicable to any kind of disease, organ and modality. So far, radiomics approach has never been extended in medical ultrasonography

1.4 Objective

The objective of this thesis is to present a set of multi-purpose and multi-modal automated strategies in the field of ultrasound based-diagnosis; the proposed approach aims to overcome the limitation of traditional CADx and become the bridge technology enabling the effective extraction of image data, in both semantic attribute and agnostic features. The described strategies can bring the radiomics discipline to be extended in medical ultrasound imaging.

The automated strategies presented in this thesis have been applied in 2-D skeletal muscle ultrasound imaging, in the investigation of muscle skeletal disorders

with the extraction of geometrical parameters and image texture descriptors. In the present study, a distinction between healthy controls and pathological endocrine patients is explored.

Other strategies have been applied in the 3-D Contrast-Enhanced, Power Doppler and Acoustic Angiography tumor the objective vasculature characterization in two tumor models (thyroid nodules and pre-clinical implanted fibrosarcoma). With the approach presented in this thesis it is possible to provide information on the overall vasculature in terms of architecture and tortuosity and to show how those features can reflect the tumor malignancy and stage.

1.5 Outline of the Thesis

Each chapter in this thesis consists of one or more published articles or a manuscript in preparation for a peer-reviewed journal. Chapter 4 is based on a conference paper and oral presentation at European Symposium on Ultrasound Contrast Imaging (ICUS) 2017. Chapter 5 is based on a published proceeding of the IEEE International Ultrasonics Symposium (IUS) 2017. All the articles have been incorporated in the thesis with minimal modification and are therefore self-contained. Further validations and supplementary research material complete each study. A list of publication can be found at the end of each chapter.

The aim of this thesis is to propose a set of fully automated and robust image processing strategies in the field of medical ultrasonography. All the proposed strategies are addressed to different ultrasound modalities (B-Mode, Contrast-Enhanced Ultrasound - CEUS, Power Doppler and Acoustic Angiography-AA), dimensions (2-D and 3-D imaging) and are built following common approaches of image processing (such as denoising and artifacts recognition, single and multiscale enhancement filtering, segmentation heuristic procedures, objects identification, structures reduction). Features extraction techniques of semantic attributes (such as distance metrics, area similarity indices, tortuosity metrics) and agnostic descriptors

(such as statistical and morphological texture features) are proposed to provide high-dimensional image data. The enabling techniques presented in this work are designed, developed and quantitatively validated to efficiently improve the overall patients' diagnosis and enable the creation of image features databases and diagnostic cut-off values.

The thesis work can be subdivided in 2 macro-sections: in the first part, three automated algorithms for the reliable quantification of 2-D B-Mode ultrasound skeletal muscle architecture and morphology are proposed. In the second part, two fully automated algorithms for the objective assessment and characterization of tumors' vasculature in 3-D CEUS and PDUS thyroid tumors and preclinical AA cancer growth are presented.

In Chapter 2, three fully automated algorithms, named MUSA (Muscle UltraSound Analysis), fascicles detection algorithm and TRAMA (TRANsversal Muscle Analysis) are proposed in the architecture investigation of four skeletal muscles (rectus femoris, vastus lateralis, tibialis anterior, medial gastrocnemius). MUSA algorithm is specifically designed to measure, in longitudinal scans, the muscle thickness, the fascicles detection algorithm provides the fascicles length and the pennation angle, while TRAMA algorithm is proposed to extract and analyze the Visible Cross-Sectional Area (VCSA), in transversal scans, of the four skeletal muscles. MUSA, the fascicles detection and TRAMA algorithms have been validated on two datasets of 200 images each; automatic measurements of muscle thickness, pennation angle, fascicles length and VSCA have been compared with expert operators' manual measurements and proven to be interchangeable.

In Chapter 3, main findings on muscle quality assessment by means of Mean Echo Intensity (MEI) and agnostic texture descriptors in healthy controls are proposed. In the last part of Chapter 3, VCSAs provided by TRAMA algorithms are used in the characterization of muscle patterns in endocrine disorders and in the comparison with healthy controls by means of quantitative statistical and morphological texture analysis.

In Chapter 4, quantitative assessment of tumor vasculature is proposed in two automated algorithms for the objective characterization of 3-D Contrast-Enhanced (CEUS) and Power Doppler (PDUS) thyroid nodules ultrasound imaging. Vasculature analysis was performed extracting architectural parameters (such as the Number of vascular Trees – NT, Number of Branches – NB and the vascular volume density- VVD) and vessels tortuosity (Distance Metric - DM, Inflection Count Metric - ICM, Sum Of Angle Metrics - SOAM). Cut-off values between benign and malignant tumors are provided, showing that vascular features extracted from the 20 thyroid nodules in 3-D CEUS and PDUS volumes can statistically distinguish benign from malignant tumors with 100% specificity and sensitivity success rate for both the ultrasound techniques, in agreement with the histopathological findings.

In Chapter 5, Vasculature parametric maps are extracted from 8 rats with implanted fibrosarcoma and investigated with 3-D AA along 4 time points (TPs), in both control and tumors areas. Results have been compared with manual previous findings in a longitudinal tumor growth study, showing that parameters extracted from the control area are statistically different compared to the ones within the tumor volume. Tumor angiogenetic vessels present a smaller diameter, higher values of NT, NB and tortuosity metrics. Moreover, the analysis of tumor growth evolution is characterized by the significant raise of NT and NB, an almost constant value of vessel diameter and a considerable drop of VVD along the four TPs. These results give insight on tumor angiogenic evolution.

Conclusions and final remarks on the work are reported at the end of the thesis.

1.6 References

- [1] A. Ntoulia, S. Anupindi, K. Darge, and S. Back, "Applications of contrast-enhanced ultrasound in the pediatric abdomen," *Abdom. Radiol.*, 2017.
- [2] V. Rafailidis, C. Fang, G. T. Yusuf, D. Y. Huang, and P. S. Sidhu, "Contrast-enhanced ultrasound (CEUS) of the abdominal vasculature," *Abdom. Radiol.*, 2017.
- [3] A. S. McQueen and K. S. Bhatia, "Head and neck ultrasound: technical advances, novel applications and the role of elastography," *Clin. Radiol.*, 2017.
- [4] Y. Guo, Y. Hu, M. Qiao, Y. Wang, J. Yu, J. Li, and C. Chang, "Radiomics Analysis on Ultrasound for Prediction of Biologic Behavior in Breast Invasive Ductal Carcinoma," *Clin. Breast Cancer*, 2017.
- [5] S. Pillen, I. M. P. Arts, and M. J. Zwarts, "Muscle ultrasound in neuromuscular disorders," *Muscle and Nerve*, pp. 679–693, 2008.
- [6] R. B. Gold, "Ultrasound Imaging During Pregnancy," *Fam. Plann. Perspect.*, vol. 16, pp. 240–243, 1984.
- [7] Swedish Council on Health Technology Assessment., "Methods of Early Prenatal Diagnosis: A Systematic Review," 2007.
- [8] G. Pagani, G. Cali, G. Acharya, I. Timor Trisch, J. Palacios-Jaraquemada, A. Familiari, D. Buca, L. Manzoli, M. E. Flacco, F. Fanfani, M. Liberati, G. Scambia, and F. D'Antonio, "Diagnostic accuracy of ultrasound in detecting the severity of abnormally invasive placentation: a systematic review and meta-analysis," *Acta Obstet. Gynecol. Scand.*, 2017.
- [9] R. Sadineni, Bs. Kumar, N. Chander, and D. Boppana, "Prenatal sonographic diagnosis of hypoplastic left heart syndrome," *Int. J. Appl. Basic Med. Res.*, vol. 7, pp. 213–215, 2017.
- [10] B. Kazmierski, C. Deurdulian, H. Tchelepi, and E. G. Grant, "Applications of contrast-enhanced ultrasound in the kidney," *Abdom. Radiol.*, 2017.
- [11] J. Öhman, V. P. Harjola, P. Karjalainen, and J. Lassus, "Rapid cardiothoracic ultrasound protocol for diagnosis of acute heart failure in the emergency department," *Eur. J. Emerg. Med.*, p. 1, 2017.
- [12] T. Nishi, K. Shibayama, M. Tabata, N. Kato, M. Noguchi, H. Okumura, Y. Kawano, D. Nakatsuka, K. Obunai, Y. Kobayashi, and H. Watanabe, "Accuracy and usefulness of aortic annular measurement using real-time three-dimensional transesophageal echocardiography: Comparison with direct surgical sizing," *J. Cardiol.*, 2017.
- [13] H. Yoshimura, M. L. Giger, K. Doi, H. MacMahon, and S. M. Montner, "Computerized scheme for the detection of pulmonary nodules. A nonlinear filtering technique," *Invest. Radiol.*, vol. 27, pp. 124–129, 1992.
- [14] M. L. Giger, K. Doi, and H. MacMahon, "Image feature analysis and computer-aided diagnosis in digital radiography. 3. Automated detection of nodules in peripheral lung fields," *Med. Phys.*, vol. 15, pp. 158–166, 1988.
- [15] H. Fujita, K. Doi, L. E. Fencil, and K. G. Chua, "Image feature analysis and computer-aided diagnosis in digital radiography. 2. Computerized determination of vessel sizes in digital subtraction angiography," *Med. Phys.*, vol. 14, pp. 549–556, 1987.
- [16] M. L. Giger, "Update on the potential of computer-aided diagnosis for breast cancer," *Future Oncol.*, vol. 6, no. 1, pp. 1–4, Jan. 2010.
- [17] K. Doi, "Computer-aided diagnosis in medical imaging: historical review, current status and future potential," *Comput. Med. Imaging Graph.*, vol. 31, no. 4–5, pp. 198–211, 2007.
- [18] J.-Z. Cheng, D. Ni, Y.-H. Chou, J. Qin, C.-M. Tiu, Y.-C. Chang, C.-S. Huang, D. Shen, and C.-M. Chen, "Computer-Aided Diagnosis with Deep Learning Architecture: Applications to Breast Lesions in US Images and Pulmonary Nodules in CT Scans," *Sci. Rep.*, vol. 6, no. 1, p. 24454, Jul. 2016.
- [19] B. Puja, M. Deepti, and A. Rupa, "Computer-aided Characterization and Diagnosis of Diffuse Liver Diseases Based on Ultrasound Imaging," *Ultrason. Imaging*, vol. 39, no. 1, pp. 33–61, 2017.

- [20] R. T. Ribeiro, R. Tato Marinho, and J. M. Sanches, "An Ultrasound-Based Computer-Aided Diagnosis Tool for Steatosis Detection," *IEEE J. Biomed. Heal. Informatics*, vol. 18, pp. 1397–1403, 2014.
- [21] E. Cho, E.-K. Kim, M. K. Song, and J. H. Yoon, "Application of Computer-Aided Diagnosis on Breast Ultrasonography: Evaluation of Diagnostic Performances and Agreement of Radiologists According to Different Levels of Experience," *J. Ultrasound Med.*, 2017.
- [22] M. H. Yap, G. Pons, J. Marti, S. Ganau, M. Sentis, R. Zwigelaar, A. K. Davison, and R. Marti, "Automated Breast Ultrasound Lesions Detection using Convolutional Neural Networks," *IEEE J. Biomed. Heal. Informatics*, 2017.
- [23] U. Acharya, S. Sree, M. Krishnan, F. Molinari, W. Zieleznik, R. Bardales, A. Witkowska, and J. Suri, "Computer-aided diagnostic system for detection of Hashimoto thyroiditis on ultrasound images from a Polish population," *J. Ultrasound Med.*, vol. 33, pp. 245–253, 2014.
- [24] J. Ma, F. Wu, T. Jiang, Q. Zhao, and D. Kong, "Ultrasound image-based thyroid nodule automatic segmentation using convolutional neural networks," *Int. J. Comput. Assist. Radiol. Surg.*, pp. 1–16, Jul. 2017.
- [25] O. Faust, U. R. Acharya, V. K. Sudarshan, R. S. Tan, C. H. Yeong, F. Molinari, and K. H. Ng, "Computer aided diagnosis of Coronary Artery Disease, Myocardial Infarction and carotid atherosclerosis using ultrasound images: A review," *Phys. Med.*, vol. 33, pp. 1–15, 2017.
- [26] X.-X. Luo, F. Fang, H.-K. So, C. Liu, M.-C. Yam, and A. P.-W. Lee, "Automated left heart chamber volumetric assessment using three-dimensional echocardiography in Chinese adolescents," *Echo Res. Pract.*, vol. 4, no. 4, pp. 53–61, Dec. 2017.
- [27] A. Maged, G. Youssef, A. hussien, H. Gaafar, M. elsherbini, R. elkomy, M. Eid, N. A. el-hamid, and A. Abdel-razek, "The role of three-dimensional ultrasonography fetal lung volume measurement in the prediction of neonatal respiratory function outcome," *J. Matern. Neonatal Med.*, vol. 2, pp. 1–121, 2017.
- [28] J. A. Noble and D. Boukerroui, "Ultrasound image segmentation: a survey," *IEEE Trans. Med. Imaging*, vol. 25, pp. 987–1010, 2006.
- [29] R. Rodríguez and R. Hernández, "An unsupervised strategy for biomedical image segmentation," *Adv. Appl. Bioinform. Chem.*, vol. 3, pp. 67–73, 2010.
- [30] A. F. Frangi, W. J. Niessen, K. L. Vincken, and M. a Viergever, "Multiscale vessel enhancement filtering," *Medial Image Comput. Comput. Invervention - MICCAI'98. Lect. Notes Comput. Sci. vol 1496*, vol. 1496, pp. 130–137, 1998.
- [31] R. J. Gillies, P. E. Kinahan, and H. Hricak, "Radiomics: Images Are More than Pictures, They Are Data," *Radiology*, vol. 278, pp. 563–577, 2016.
- [32] R. M. Haralick, K. Shanmugam, and I. Dinstein, "Textural Features for Image Classification," *IEEE Trans. Syst. Man. Cybern.*, vol. SMC-3, pp. 610–621, 1973.
- [33] M. M. Galloway, "Texture analysis using gray level run lengths," *Comput. Graph. Image Process.*, vol. 4, pp. 172–179, 1975.
- [34] T. Ojala, M. Pietikainen, and T. Maenpaa, "Multiresolution gray-scale and rotation invariant texture classification with local binary patterns," *IEEE Trans. Pattern Anal. Mach. Intell.*, vol. 24, pp. 971–987, 2002.
- [35] T. Ojala, M. Pietikainen, and D. Harwood, "A comparative study of texture measures with classification based on featured distributions," *Pattern Recognit.*, vol. 29, pp. 51–59, 1996.
- [36] F. Davnall, C. S. P. Yip, G. Ljungqvist, M. Selmi, F. Ng, B. Sanghera, B. Ganeshan, K. A. Miles, G. J. Cook, and V. Goh, "Assessment of tumor heterogeneity: an emerging imaging tool for clinical practice?," *Insights Imaging*, vol. 3, pp. 573–589, 2012.
- [37] J. P. B. O'Connor, C. J. Rose, J. C. Waterton, R. A. D. Carano, G. J. M. Parker, and A. Jackson, "Imaging intratumor heterogeneity: role in therapy response, resistance, and clinical outcome," *Clin. Cancer Res.*, vol. 21, pp. 249–257, 2015.

Chapter 2

Automated architectural analysis in skeletal muscle ultrasound imaging

Part of this chapter has been published as:

C. Caresio, M. Salvi, F. Molinari, K.M. Meiburger and M.A. Minetto, **Fully Automated Muscle Ultrasound Analysis (MUSA): Robust and Accurate Muscle Thickness Measurement.**, *Ultrasound Med. Biol.*, 2017; 43: 195–205.

2.1 Introduction

In recent years, ultrasound imaging has been proven to be an effective technique in the study of normal and pathological skeletal muscles [1]–[3]. Musculoskeletal ultrasonography enables the complete, reliable and non-invasive investigation of skeletal muscles [4], [5] and has been extensively used in both architectural and morphological muscles characterization.

The 2-D B-Mode sonographic appearance of superficial skeletal muscles is clearly distinctive and can be easily discriminated at the visual inspection [6]: in the longitudinal plane, along the principal axis, skeletal muscles are identified by the superficial and the deeper aponeuroses, two boundaries of highly reflective epimysial connective tissue. The longitudinal muscle region looks relatively darker compared to the surrounding structures (such as the subcutaneous tissue layer and the bones) and featured by a characteristic pattern formed by the presence of muscle fascicles, a bundle of perimysial connective tissue fibers organized according to a specific macroscopic architecture. Muscle fascicles are the contractile part of skeletal muscle and can be disposed in linear (i.e. medial gastrocnemius), pinnate (i.e. tibialis anterior) or triangular structure (i.e. vastus lateralis).

In the transversal plane, the perpendicular one to the principal muscle axis, the gross cross-sectional of skeletal muscles can be identified by an enclosed region with small homogeneous reflections of perymysial fibers surrounded by the echogenic epimysial layer (i.e. rectus femoris) or bone echo (i.e. biceps brachii). The shape and the dimension of this region can vary along the principal axis; in addition, on this projection, an internal fascia of connective tissue can be recognized in bi-compartmental (i.e. tibialis anterior) or bipenniform muscles (i.e. rectus femoris).

Ultrasonography allows the objective quantification of anatomical muscle parameters, which highly reflect the overall muscle health, mass and strength [7]. The link between muscle structure and function has been discussed and proved since a century [8]. Four main representative parameters of the muscle geometry

are generally considered in clinical practice and in scientific literature [9] and extracted from the two principal scanning projections:

1. muscle thickness, MT (longitudinal plane), defined as the distance between the superficial and the deeper muscle aponeurosis;
2. pennation angle, PA (longitudinal plane), a global averaged parameter that takes into account the angle formed between the deeper aponeurosis and the direction on parallel fascicles, or more specifically the fiber angle relative to the force-generating axis [10];
3. fascicles length, FL (longitudinal plane), namely the linear measurement of muscle fibers between the superficial and deep aponeurosis;
4. cross-sectional area CSA, (transversal plane), which is the muscle belly region delimited by the epimysium; this parameter has been proven to be directly proportional to the maximum tetanic tension generated by the muscle. In conventional skeletal ultrasound imaging, cross sectional area is usually measured using panoramic or Extended Field Of View (EVOF) tools [11].

In previous works, quantitative imaging has been applied in the assessment of muscle size in terms of MT and CSA [2], [11]–[14] in training adaptations (i.e., muscle hypertrophy [15], [16]), disuse atrophy [17], ageing (i.e., primary sarcopenia, [9], [18]–[20]) and pathological conditions [21]. Moreover, muscle size has been used to predict the leg skeletal muscle mass [22], in the total body fat free mass [23], [24] and in the extremity and trunk muscle volume estimation [25]–[29].

Regarding the muscle architecture, the arrangement of muscle fascicles directly influences the function of the muscle in terms of force generation [9], [30]; higher values of PA and smaller values of FL in resting conditions predict higher level of muscle strength excursion. In particular, the Architectural Gear Ratio AGR was proposed to estimate the contraction speed as the ration of muscle fiber velocity to muscle belly velocity [31]. Muscle fascicles architecture can be quantitatively

investigated using ultrasound imaging in resting conditions [32] during isometric contractions [33]–[38] and during dynamic exercise [33], [39]–[43]. For a given muscle CSA and volume, an increased PA results in a reduced FL, compromising shortening velocity and excursion range, but also allows more contractile material to be placed in parallel, increasing maximum force generation [44], [45].

Skeletal muscle ultrasound quantification is generally performed manually in the clinical practice; hence, this operation is timely and subjected to the user's experience. MT is usually obtained as the average of three measurements performed in the proximal, central, and distal positions on a single scan [3], [9], [16], [19], [27], while FL and PA are measured considering a small number of short visible fascicles [11], since longer ones require multiple scans or trigonometric estimation due to the limited field of view of conventional US imaging [38].

In recent studies, the overall muscle size, namely the Anatomical Cross-Sectional Area (ACSA), has been investigated by means of the panoramic or EFOV US imaging technique [46], [47] in hamstring muscle [48], gluteus muscle [49], vastus lateralis [50], [51] in both resting and training conditions. This technique also enables the selection of large group of skeletal muscles [52], but the acquisition involves the use of guides and operating experience. Moreover, even though the ACSA measurement is a reliable way to assess muscle size, health and strength, it requires high level of precision in the manually tracing, dedicated software tools and time. On the other hand, the analysis of muscle size and quality can be reduced to the extraction of the Visible Cross-Sectional Area (VCSA) which has been used in previous studies [21] in the assessment of skeletal muscle disorders.

To overcome the limits of the MT, FL, and PA manual measurements, several automatic or semi-automatic algorithms have been described in the last decays for the quantitative skeletal-muscle ultrasound imaging. For the MT measurements, muscle boundaries tracking has been proposed by Koo et al. [53] to track the locations of aponeuroses of the pectoralis major muscle. Wong et al. [54] identify the region of interest to measure the thickness of abdominal muscles using a

sequential quadratic programming approach (based on a novel log-Rayleigh likelihood function). In another work, The Revoting Hough Transform was applied to automatically estimate the gastrocnemius muscle thickness and the performance of two preprocessing procedures was investigated by Han et al. [55]. Finally, Ling et al. [56] proposed a method based on the lower boundary of superficial aponeurosis and upper boundary of deep aponeurosis to calculate the gastrocnemius muscle thickness.

Automatic fascicles detection has been performed, in the last years, in B-Mode ultrasound dynamic conditions. Rana et al. [57] proposed a multiscale filter approach to enhance muscle fibers structure followed by the application Radon transform and a wavelet analysis, and similar approaches have been used in other works [58], [59] in the detection of gastrocnemius fascicles muscle without the use of edge maps. More recently, Zhou et al. [60] proposed a new method based on the Re-Voting Hough transform (RVHT) in order to detect the line-like structure in muscular-skeletal images; under the assumption of straight fascicles, the RVHT approach was proven to perform better in fascicles localization since it depended on the edge map of the image. The method was improved with the detection of muscle aponeuroses and the application of the Gabor wavelets analysis in Zhou et al. [61]. Although the previous cited works were applicable in the study of muscle architecture changes during contractions, they were all developed to be specifically addressed to the study of a unique muscle, the medial gastrocnemius; in addition, all these methods required a minimal, but still needed, manual initialization, in the position of the search ROIs inside the first frame, or marking the aponeuroses. Finally, the fascicles detection has never been extended, in an automatic fashion, from the automatic extraction of muscle aponeuroses.

Besides their goodness, effectiveness and accuracy, all the previous cited methods for the MT, PA and FL measurements present a countless number of weak points, such as the manual initialization, the need of images storage for the offline processing, the low number of samples used in test and validation, and the design

oriented on a specific muscle or application, which make them unsuitable for the clinical use. Furthermore, so far, an automatic algorithm for the extraction of the ultrasound muscle ACSA or the VCSA in conventional B-Mode scans has never been proposed in literature. Finally, the major limitation of these approaches consists in the absence of a fully automated tool able to completely measure, in real time and in a single conventional scan, the 4 main skeletal muscle parameters (MT, FL, PA, VCSA) described in the previous paragraphs.

In this chapter, three innovative and robust automatic algorithms, named MUSA (Muscle UltraSound Analysis), TRAMA (Transversal Muscle Analysis) and a fascicles detection algorithm are proposed to completely characterize, with a single scan and in few seconds processing, the skeletal muscle geometry and architecture, both in longitudinal and transversal planes. MUSA algorithm and the fascicles detection algorithm are specifically designed for the geometrical muscle quantification, such as MT, PA and FL, whereas TRAMA is specifically designed for the VCSA extraction. To the best of our knowledge, these are the first validated algorithms that include the complete characterization of at least four skeletal muscles: rectus femoris, vastus lateralis tibialis anterior and medial gastrocnemius. In this context, an automatic strategy is built including scale and edge filters combined with heuristic approaches and applied in the detection of anatomical structures, such as aponeuroses and fascicles.

2.2 Materials and Methods

2.2.1 Longitudinal Muscle Ultrasound Analysis: MUSA algorithm

The content of this section is dedicated to description of the MUSA algorithm, specifically designed to automatically detect the muscle aponeuroses and fascicles along the longitudinal projection. The algorithm was developed using the Matlab (MathWorks, Natick, MA, USA) environment. The procedure is schematically

described in fig. 2.1 the detailed description of the steps is reported in the following.

Subjects and acquisition settings

A total of 50 healthy subjects without neuromuscular diseases (25 males and 25 females, mean \pm SD age: 31.0 ± 10.9 years; body mass index: 24.3 ± 4.7 kg /m²) took part as volunteers in this study. Four skeletal-muscles were investigated on the dominant side during the ultrasound session: rectus femoris, vastus lateralis, tibialis anterior, and medial gastrocnemius. The detailed explanation of the ultrasound device settings and the acquisition protocol is reported in APPENDIX A and B. One scan of each muscle was taken in the longitudinal plan, and a total of 200 images (50 subjects x 4 muscles) were captured and analyzed. The images were converted in DICOM format and then transferred to a workstation for offline processing.

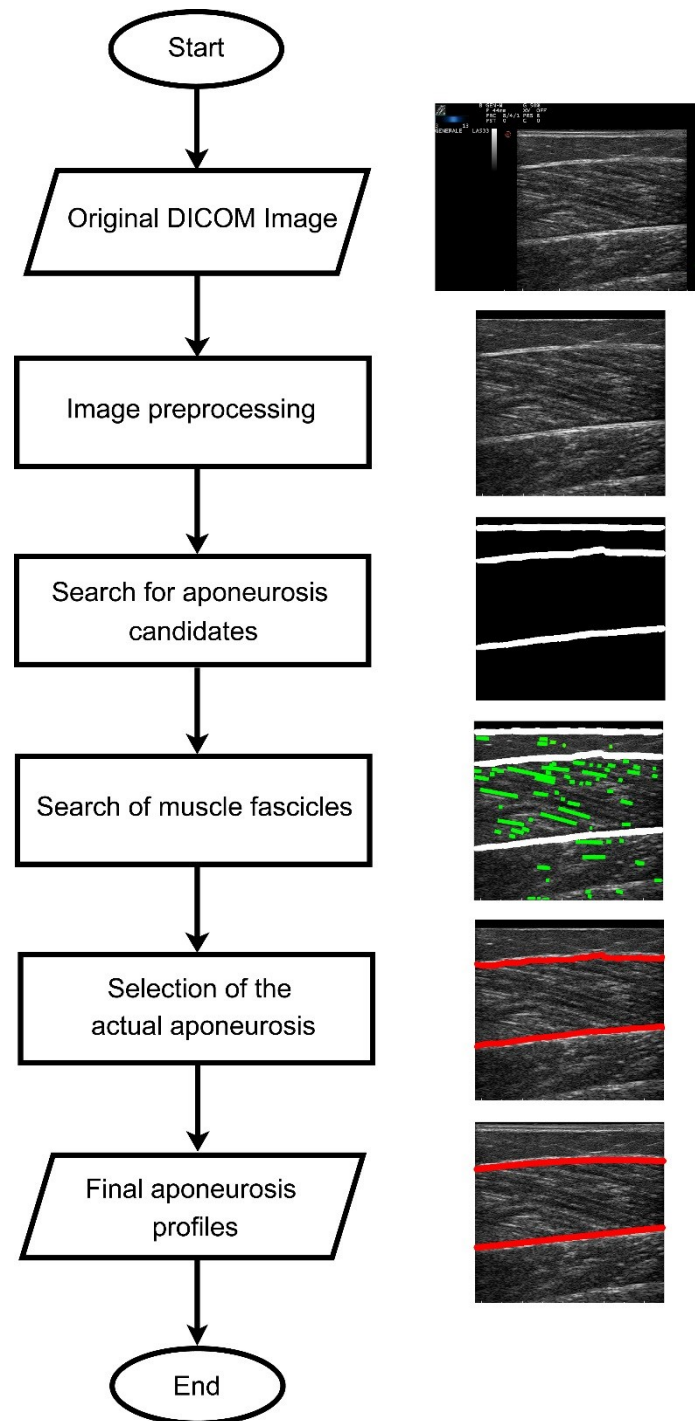


Figure 2. 1: Schematic representation of MUSA algorithm steps.

Image preprocessing

The original DICOM image (fig. 2.2.A) is automatically cropped (referring to the DICOM header tag “RegionLocation”) to maintain only the region containing the ultrasound data. The uppermost 2 mm of the image are then blackened to exclude the dead zone and the skin from further processing. The automatically cropped image can be seen in fig. 2.2.B.

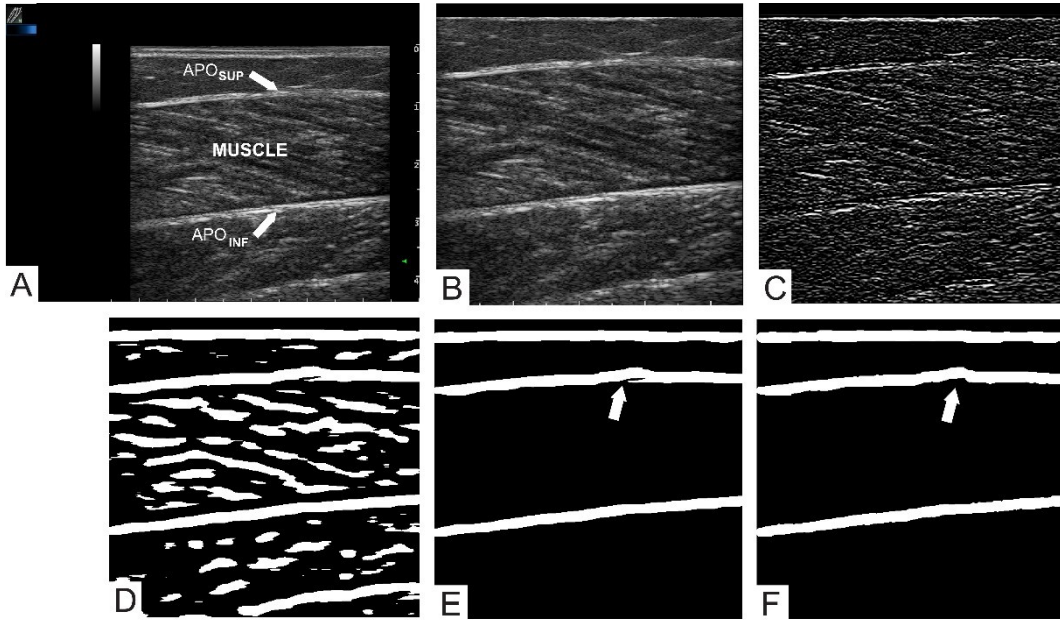


Figure 2. 2: MUSA algorithm first steps. Panel A - Original image of a representative medial gastrocnemius muscle. Panel B - automatically cropped image. Panel C - vertical Sobel of image; panel D - binary mask of the FODG filter. Panel D - FODG mask with inconsistent aponeurosis structures eliminated. Panel F - FODG mask with branch removal. In panels E and F, the arrow indicates the effect of the branch removal on the binary FODG mask. APO_{SUP} = superficial aponeurosis; APO_{INF} = deep aponeurosis

Automated search for the aponeuroses candidates

This first processing step is devoted to automatically search for the possible position of the aponeuroses inside the image. The image is first downsampled by a factor of two (i.e., the number of rows and columns of the image is halved). To enhance all the structures inside the image that are possible aponeuroses we compute the vertical Sobel gradient of the image (fig. 2.2.C) The Sobel operator

performs a 2-D spatial gradient measurement on an image and so emphasizes regions of high spatial frequency that correspond to edges.

Subsequently, we apply a vertical First-Order Derivative Gaussian (FODG) filter to the processed image. The FODG filter is obtained by the convolution of a Gaussian kernel and a simple derivative filter [62]. This filter enhances all the structures bigger than the dimension of the FODG kernel and attenuates the others. Hence, the dimension of the FODG kernel is set to 9 pixels, to ease the aponeurosis highlighting.

Finally, we threshold the FODG output to produce the binary FODG mask (fig. 2.2.D). The threshold is set the 80% of the maximum gray level of the FODG output.

The binary FODG mask represents the two muscle aponeuroses as well as other white regions representing different structures. A heuristic cleaning step is performed to remove all the structures that do not match specific conditions (i.e., that do not qualify as aponeuroses candidates). We label all the disconnected regions in fig. 2.2.D and we approximate them as ellipses. Since the structures corresponding to aponeuroses have a horizontal size similar to the size of the image, we remove all the regions with eccentricity lower than 0.995 and with a major axis shorter than 70% of the length (in pixels) of the image. The cleaned mask is shown in fig. 2.2.E. Branching and region filling is then performed to adjust the morphology of the remaining regions. The white arrow in fig. 2.2.F shows the correction made with respect to the irregularity of the superficial aponeurosis of fig. 2.2.E.

Selection of the actual aponeuroses

The binary FODG mask fig. 2.2.F often contains more candidate aponeuroses. We check the presence of muscle fascicles between each pair of candidates in order to distinguish the two actual aponeuroses from the other candidates (i.e. we check that the two aponeuroses actually delimit the muscle region). We first equalize the

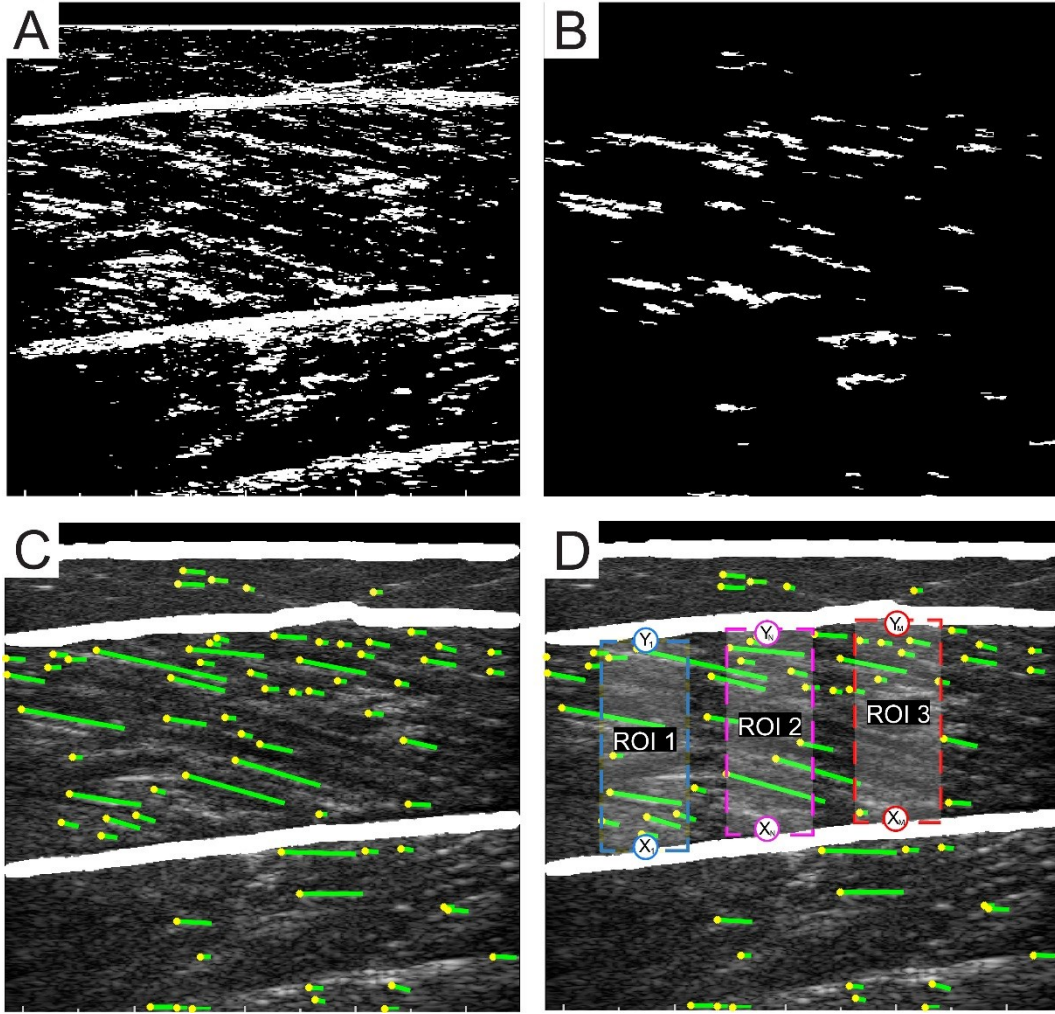


Figure 2. 3: Fascicle detection and heuristic. Panel A - Binary mask obtained with image equalization and Otsu thresholding; Panel B - cleaned fascicle mask; Panel C - Final fascicles mask overlaid on original image. The fascicles are portrayed in green, whereas the endpoints of the fascicles are in yellow; Panel D - sketch of the heuristic search. The fascicles are shown in green, the endpoints in yellow and three example ROIs are drawn in dotted rectangles.

original image and then apply a global thresholding using the Otsu's method [63] to obtain a binary mask (that will be indicated in the following as "binary fascicle mask"). Figure 2.3.A shows the binary fascicle mask where aponeuroses and fascicles are visible. The aponeuroses candidates (fig. 2.2.F) are then removed from this binary fascicle mask (fig. 2.3.B), together with all the regions having an area

lower than 10 pixels (which are likely to represent over segmentation due to speckles).

Since the muscle fascicles can be approximated by a line with a specific orientation, we applied the Standard Hough Transform [64] on the binary fascicle mask. The Standard Hough Transform uses the parametric representation of a line in polar coordinates. The variable θ is the angle of the perpendicular projection from the origin to the line measured in degrees clockwise from the positive x-axis. The angle of the line itself is $\theta+90^\circ$, also measured clockwise with respect to the positive x-axis. The range of θ for our application is $-90^\circ \leq \theta \leq 85^\circ$. Fig. 2.3.C shows the original B-mode image (background) with overlaid the binary FODG mask (white) and the detected fascicles (green lines). The uppermost endpoint of each fascicle is marked by a yellow dot.

The image is then considered column-wise. One column every ten is processed until reaching the total number of columns N , since, at this stage, we do not need the accurate profile of the aponeurosis, but only the correct aponeuroses among the possible candidates. On each i -th column, the candidates are considered starting from the deepest. We apply an iterative heuristic search made of the following steps:

1. Considering a point of the deepest candidate (marked by X_i in fig. 2.3.D), we delineate a region of interest (ROI) (blue region in fig. 2.3.D). The vertical size of the ROI corresponds to the distance of the considered point X_i from the corresponding point on the same column belonging to the closest candidate aponeurosis upwards (marked by Y_i in fig. 2.3.D). The horizontal size of the ROI is fixed to 41 pixels (corresponding to 3.8 mm). This horizontal size was selected in order to make sure that the region contained some fascicles.
2. If the vertical size of this ROI is lower than 15 mm, the two candidates are too close and they cannot be the actual aponeuroses; hence, the point on the deepest candidate is discarded and the procedure goes back to point 1).

3. If the condition at point 2) is matched, the points X_i and Y_i indicate the deep and superficial aponeurosis (that will be indicated in the following as APO_{Inf} and APO_{Sup}), respectively, only if muscle fascicles are present in between. Hence, we compute the number of fascicles endpoints (yellow dots in fig. 2.3.C) falling into the ROI. If this number is lower than 20% of the overall number of endpoints in the whole image, we consider that there is no muscle in between X_i and Y_i . The procedure then discards X_i and steps back to 1).
4. If the number of fascicle endpoints is higher than 20% of the overall number of endpoints in the image, the point X_1 is marked as the deep aponeurosis APO_{Inf} and the point Y_1 as the temporary superficial one APO_{Sup} .
5. A further control is made on the gray level of point Y_i : if the gray level of Y_i , in the original image, is lower than the 60% of the maximum gray level found along the i -th column, the index of Y_i is iteratively updated proceeding from the bottom to the top along the column, until this condition is matched.
6. The procedure iterates considering all the other columns of the image (fig. 2.3.D).

This heuristic search outputs a series of points X_i that delineate the position of the deep aponeurosis APO_{Inf} and a series of points Y_i that delineate the superficial aponeurosis APO_{Sup} . The final result of the heuristic search is represented in fig. 2.4.A. Spike detection and removal is applied to correct for possible inaccuracies and the APO_{Sup} and APO_{Inf} profiles (fig. 2.4.B).

Final aponeuroses tracing

As can be seen in fig. 2.4.B, the profile is roughly placed in correspondence of the aponeuroses, but refinement is needed. We adopt a Difference of Gaussians *DoG* filter to detect the actual edges. The *DoG* mask of an input image I can be defined as:

$$DoG = I \cdot G_1 - I \cdot G_2$$

where G_1 and G_2 are low-pass Gaussian kernels. We set for each kernel the size S (dimension in pixel) and the corresponding standard deviation σ as follows: $S_1 = 11$ pixels, $S_2 = 81$ pixels, $\sigma_1 = 101$ pixels, and $\sigma_2 = 21$ pixels. The *DoG* mask is represented in fig. 2.4.C. In the *DoG* mask, the transitions from bright to dark (i.e. from APO_{SUP} which is bright to muscle which is dark) are positive, whereas the transitions from dark to bright (i.e. from muscle to APO_{INF}) are negative. Thus, we could locate the exact position of the interface between muscle and aponeurosis in each column of the image. Figure 2.4.D reports the interpolated final profiles of the superficial and deep aponeuroses by a bicubic spline.

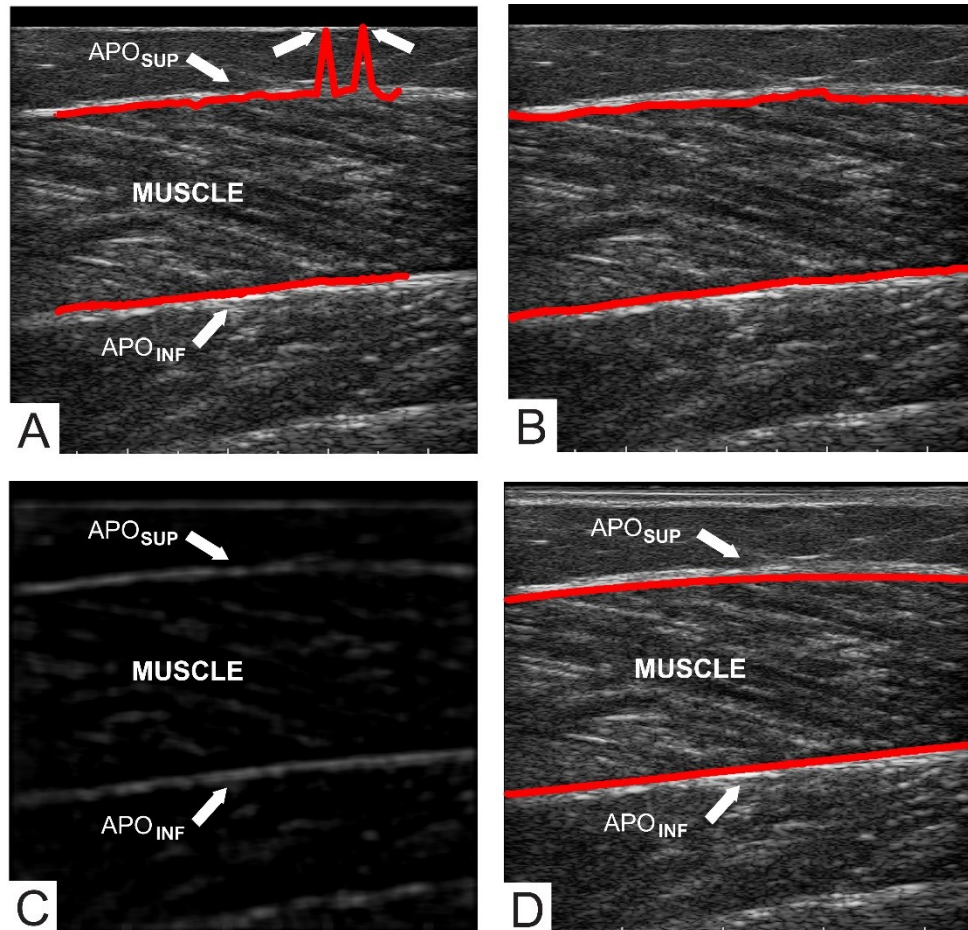


Figure 2. 4: Final profile and correct aponeurosis determination. Panel A - Profile obtained at the end of the heuristic process. The white arrow indicates the presence of spikes. Panel B - spikes removal and final trace of profile on the binary mask of the FODG filter. Panel C - application of the DoG filter on the original image. Panel D - final interpolated profiles of the superficial and deep aponeuroses.

Tibialis anterior processing

The tibialis anterior is a bicompartamental and bipennate muscle, meaning that the muscle fibers branch out at a specific angle (i.e., pennation angle), from a central intramuscular fascia to the superficial and deep aponeurosis [65]. As shown in fig. 2.5.A, the fascicles of the two compartments present opposite pennation. Our MUSA architecture is adaptable to the processing of images of multi-compartmental muscles, since its architecture can be repeated for every compartment of the muscle.

In the specific case of the tibialis anterior muscle:

1. Considering the FODG (fig. 2.5.B), the processing starts from the lower compartment. Among all candidates, the ones that are likely to correspond to the deepest aponeurosis and to the central fascia are traced (fig. 2.5.C) by applying the same strategy as described in the previous section.

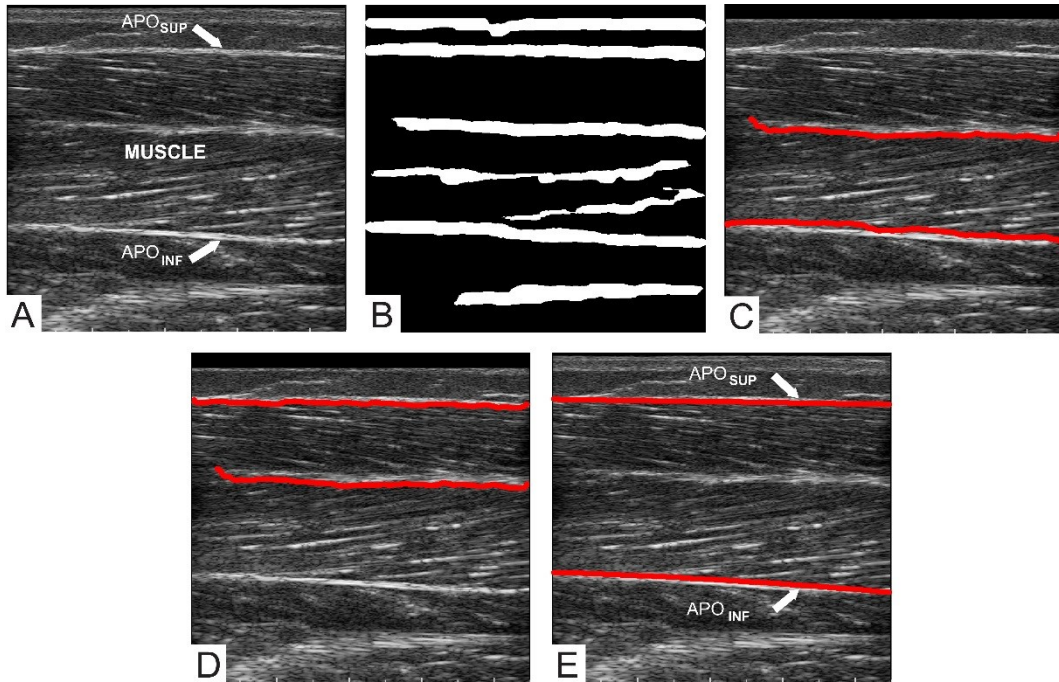


Figure 2. 5: Processing of tibialis anterior. Panel A: Example of tibialis anterior image. Panel B - binary mask of the of FODG filter for the tibialis anterior; Panel C: profiles of the deep aponeurosis and of the central aponeurosis which define the deep compartment; Panel D: profiles of superficial aponeurosis and of the central aponeurosis which define the superficial compartment; Panel E: final interpolated profiles of the superficial and deep aponeuroses for the tibialis anterior.

2. The central fascia of the tibialis anterior muscle defines the bottom limit of the upper compartment. MUSA is then applied from this profile upwards, to detect the superficial aponeurosis (fig.2.5.D).
3. Once the deep and superficial aponeurosis are located, the final profiles are obtained by using the *DoG* mask (fig. 2.5.E).

Since the pennation changes between the two compartments, the range of θ for the Standard Hough Transform has been chosen as $-90^\circ \leq \theta \leq 85^\circ$ for the upper compartment and as $95^\circ \leq \theta \leq 260^\circ$ for the lower compartment.

2.2.2 Fascicles detection algorithm

In this section, a fascicle detection algorithm is proposed, and a preliminary validation of the algorithm, based on a reduced dataset of images, is reported.

Images data set

Thirty images of test (10 of vastus lateralis, 10 of tibialis anterior and 10 of medial gastrocnemius) were selected from the previous dataset of 200 images used to test and validate the MT extraction of the MUSA algorithm. Rectus femoris images of MUSA dataset were excluded from the study because the pennation of this muscle is not visible in the projection used for the MT measurement. We make sure that the selected images contained at least 3 fascicles at the visual inspection. Since the manual measurement of PA and FL requires, for each muscle, from 10 (vastus lateralis, medial gastrocnemius) to 15 minutes (tibialis anterior), the number of images was chosen to keep the validation study timely feasible.

Fascicles detection algorithm

The complete description of the algorithm is presented in the block diagram in fig. 2.6. The fascicles detection algorithm enables the pennation angle (PA) and fascicle length (FL) measurement of skeletal muscle with visible fascicles at the

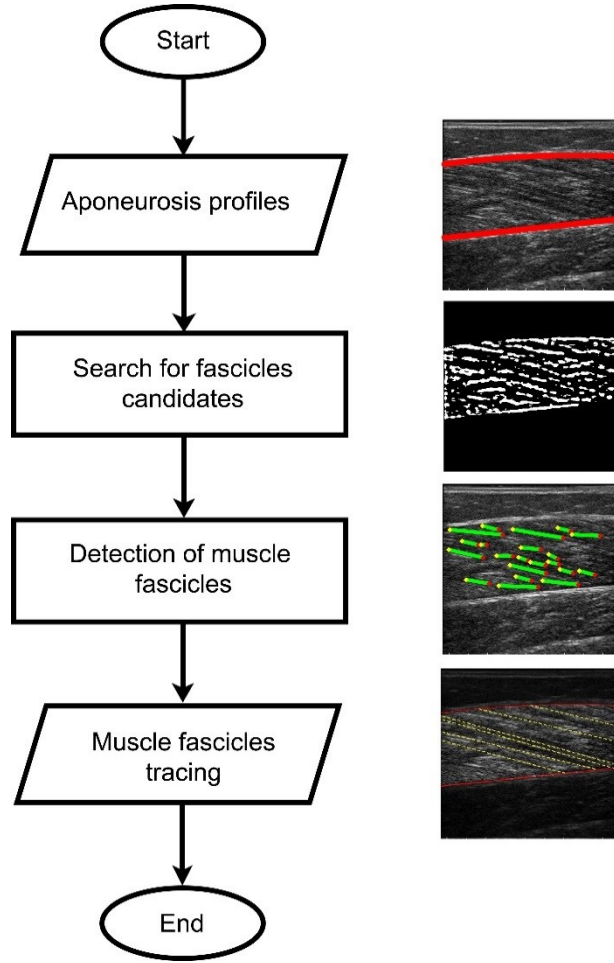


Figure 2. 6: Schematic representation of the Fascicles detection algorithm

ultrasound inspection: this method has been specifically implemented for the architectural characterization of vastus lateralis, tibialis anterior and medial gastrocnemius.

From this point on, the searching area is reduced only to the region delimited by the aponeuroses, which contains fascicles (Fig 2.7.A). The image is filter with an Absolute Difference of Gaussians (*ADoG*); The *ADoG* mask of the input image is defined as the DoG in the previous section as:

$$ADoG = |I \cdot G_1 - I \cdot G_2|$$

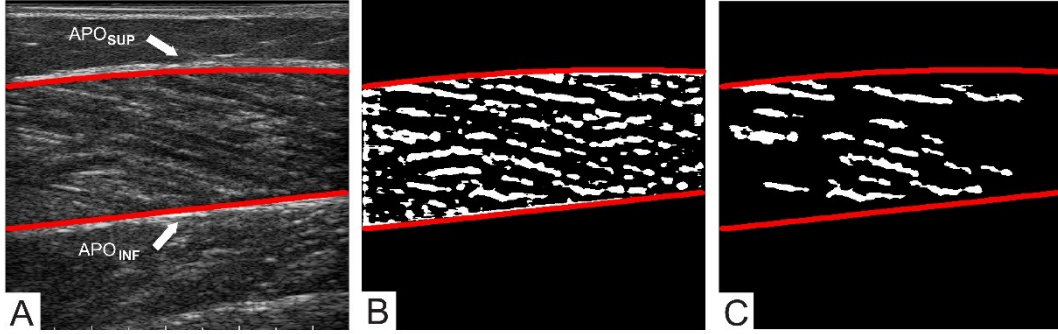


Figure 2. 7: Initial steps of the fascicles detection algorithm. Panel A: Selection of the muscle longitudinal area from MUSA algorithm. Panel B : Binary fascicles mask. Panel C: Structure cleaning on the binary fascicles mask.

where G_1 and G_2 are as before low-pass Gaussian kernels. In this case the size S and the standard deviation σ where fixed as $S1 = 9$ pixels, $S2 = 31$ pixels, $\sigma_1 = \sigma_2 = 11$ pixels. These dimensions where chosen as optimal to limit the search to specific elements dimension in any direction. A threshold of 15 % of the maximum gray value is imposed to generate a new binary fascicles mask (fig 2.7.B). A heuristic cleaning is applied on this mask to delete all the possible structures that have size and shape not referable to the anatomy of fascicles: in this specific case structure with less than 15 pixels and eccentricity lower than 0.97 are deleted (fig 2.7.C). Under the assumption that fascicles can be modeled as straight segments (fig. 2.8.A), the Hough transform is applied considering a range of possible angles between $-80^\circ - \alpha \leq \theta \leq 89^\circ - \alpha$, where α is the angle between the muscle centerline and the absolute reference system: this choice as been made to prevent the detection of major axis structures with less than 10° slope respect to the muscle inclination in the image.

For each segment identified by the Hough transform (in green), length, orientation, initial point (in yellow) and end point (in red) are considered (fig. 2.8.B). A collinearity set of rules is applied to perform the fascicles segments union. Two segments can be connected if all these conditions are satisfied:

- one of the two segments is located in the upper left corner respect to the other;

- their extensions intersect each other within the image. Parallel segments on different axes are certainly not collinear;
- The orientation of the two segments is similar and the difference in orientation between the two segments is smaller than 5° ;
- The straight line joining the segments has an orientation between the slope of the two.

The single connective segment starts from the initial point of the upper segment and ends with the endpoint of the lower one. This procedure is repeated iteratively till no more segments can be joined. An example of application of these criteria is shown in fig. 2.8.C.

Subsequently, connected segments can be separate in two groups, the ones corresponding to muscle fascicles and the one due to the presence of multiple

reflection of aponeuroses, big vessels walls or over-segmentation. Fascicles and spurious structures have usually a clear different orientation. A deterministic clustering analysis is then implemented according to the following criterion: two or more objects belong to the same cluster if they have similar orientation. Two segments with bigger and smaller absolute angle slope are taken as reference elements of the two clusters, respectively. For each remaining segment, the difference between its slope and the two references is calculated: the segment is then assigned to the cluster whose difference is smaller. At the end of this procedure, the cluster with the higher number of collinear segments is chosen as it likely contains all the visible fascicles axis. The result of this selection is shown in fig. 2.8.D.

Since two fascicles and their line extensions do not anatomically intersect each other within the muscle, a further step of processing is needed: in this case, the segment whose orientation differs most from the median value of the group is discarded (fig. 2.8.E).

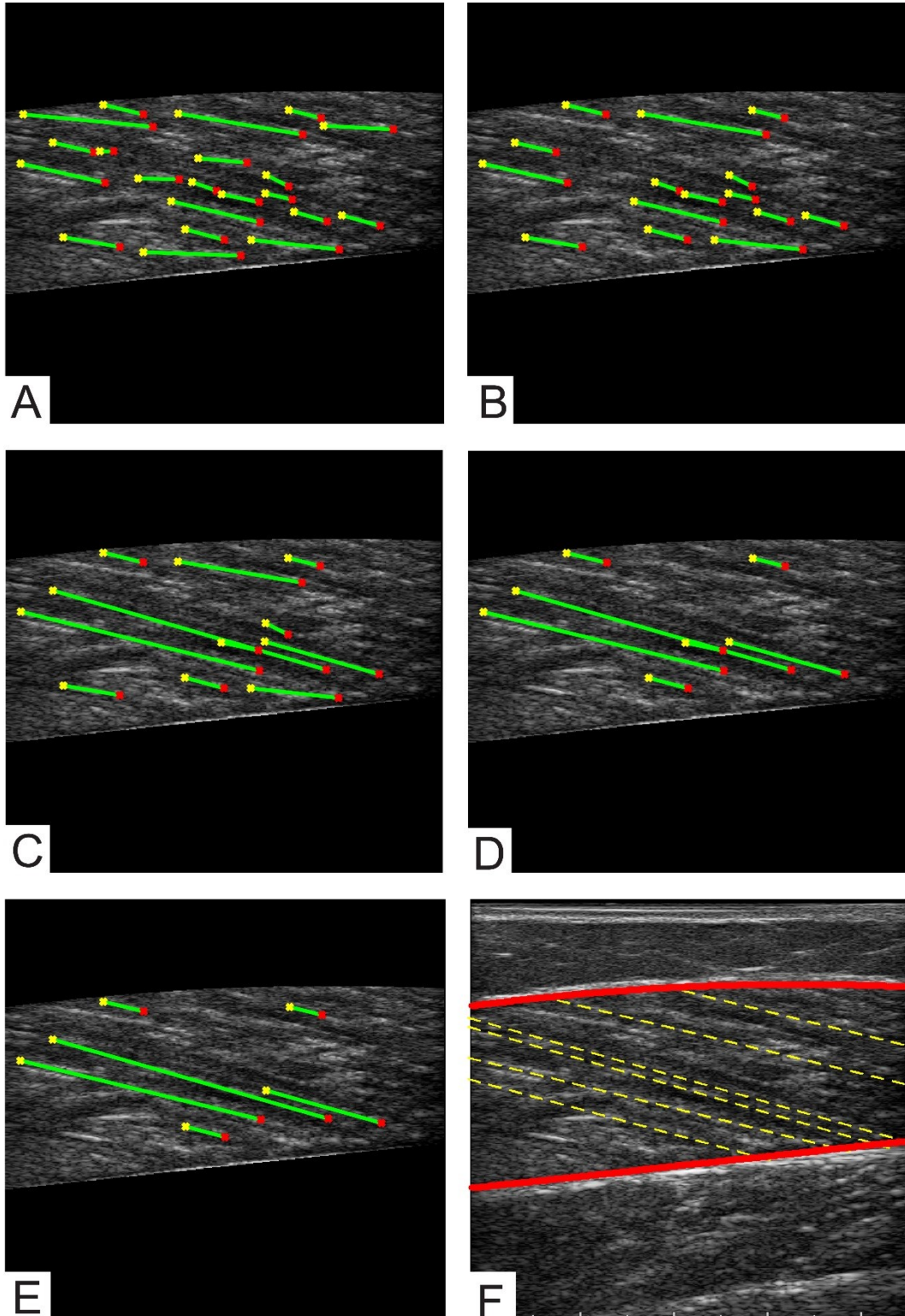


Figure 2. 8: Fascicles search processing- Panel A – Fascicles are modeled as straight lines with the application of the Hough transform. Panel B – First cleaning step. Panel C – Collinearity rules application for segments union. Panel D – Results after segments clustering. Panel E – Postprocessing and cleaning of intersecting fascicles. Panel F – Final result of the fascicles detection.

Finally, the fascicles segments are extended along the entire region of the muscle in order to measure PA and FL. The final result is represented in fig 2.8.F.

The fascicle detection algorithm has been also adjusted for the computation of PA and FL in tibialis anterior images, and more generically on image of bipennate skeletal muscle; in this case the two compartments are processed separately to identify the fascicles on both areas.

Starting from the original image (fig. 2.9.A) the processing can be divided into five steps:

1. The image is up-to-down flipped and clipped between the previously found superficial aponeurosis and intermediate fascia;
2. Fascicle detection algorithm is applied on this region (fig. 2.9.B);
3. The image is left-to-right flipped and clipped between the intermediate fascial and the deep aponeurosis
4. Fascicle detection algorithm is run on this region (fig. 2.9.C);
5. The image is recomposed and lines from the two compartments are merged.
6. Specifically, for the image used as example, the result provided to the user is shown in fig. 2.9.D

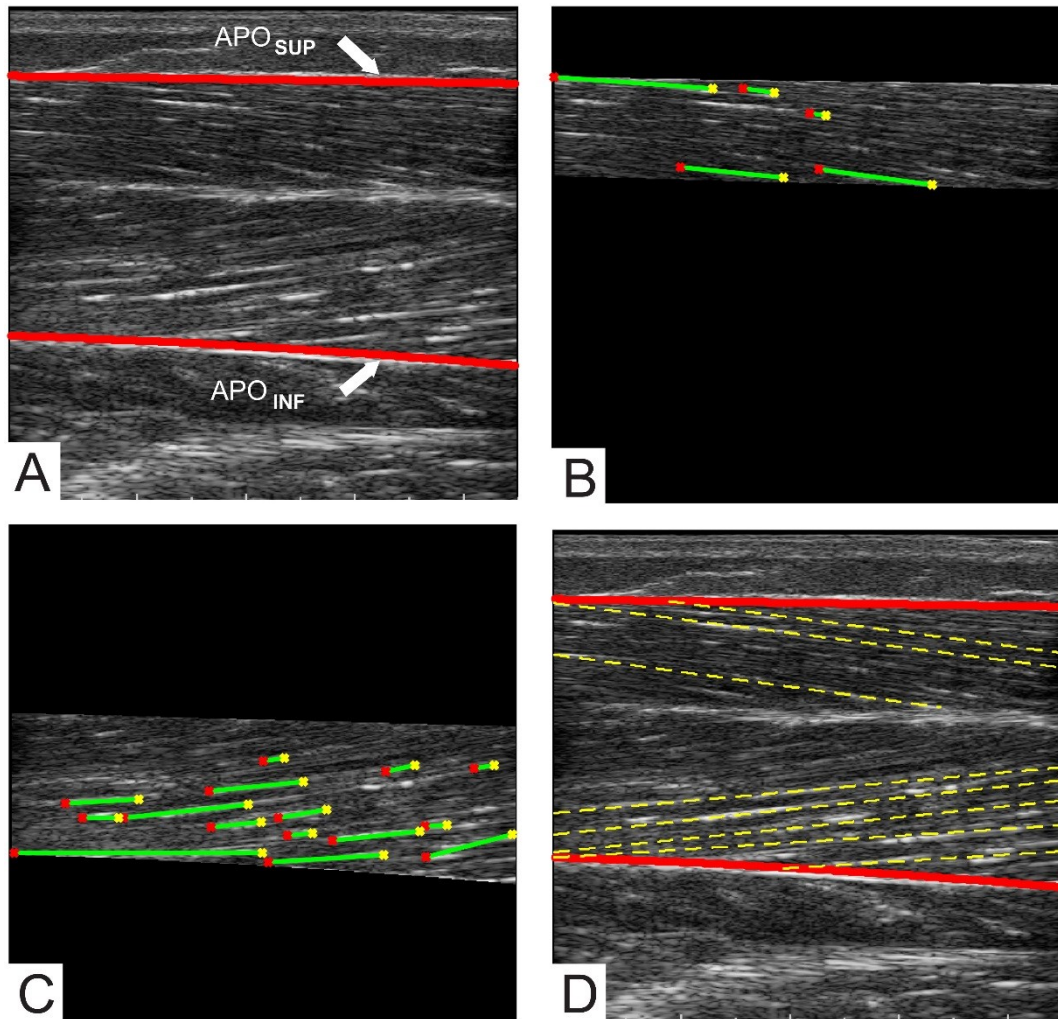


Figure 2. 9: Panel A – Selection of the searching area for the tibialis anterior. Panel B – Fascicles detection algorithm applied on the upper compartment. Panel C - Fascicles detection algorithm applied on the deep compartment. Panel D – Final result of the fascicles detection algorithm on the tibialis anterior.

2.2.3 Transversal Muscle Ultrasound Analysis: TRAMA algorithm

In the following section, an automated algorithm, named “TRansversal Architecture Muscle Analysis” (TRAMA) is presented: this method has been developed as an extension of the MUSA algorithm for the automatic segmentation of the Visible Cross-Sectional Area (VCSA), along the transversal plane, of four skeletal muscles (rectus femoris, vastus lateralis, medial gastrocnemius and tibialis anterior).

Subjects and acquisition settings

A total of 200 images (50 for each muscle) were acquired from 116 subjects (56 males and 60 females, mean \pm SD age: 35.3 ± 14.4 years; body mass index: 25.2 ± 5.4 kg/m²) 58 subjects were healthy, 58 patients present endocrine disorders or were under hormone therapy. Among the pathological patients, 17 were affected by Acromegaly, 16 by GID (Gender Identity Disorder), 9 by Cushing’s Syndrome, 7 with GHD (Growth Hormone Deficiency), 5 by Diabetes and 4 by Obesity. Four skeletal-muscles were investigated on the dominant side during the ultrasound session: rectus femoris (29 controls, 21 patients, 21 females, 29 males), vastus lateralis (36 controls, 14 patients, 21 females, 29 males), tibialis anterior (20 controls, 30 patients, 28 females, 22 males), and medial gastrocnemius (29 controls, 21 patients, 24 females, 26 males). The detailed explanation of the ultrasound device settings and acquisition protocol is reported in APPENDIX A and B. One scan of each muscle was taken in the transversal plan, and a total of 200 images were captured and analyzed. The images were converted in DICOM format and then transferred to a workstation for offline processing.

TRAMA algorithm for the VCSA segmentation

The TRAMA algorithm follows the same approach used in the MUSA algorithm. The procedure is depicted schematically in fig.2.10 and presented in the following.

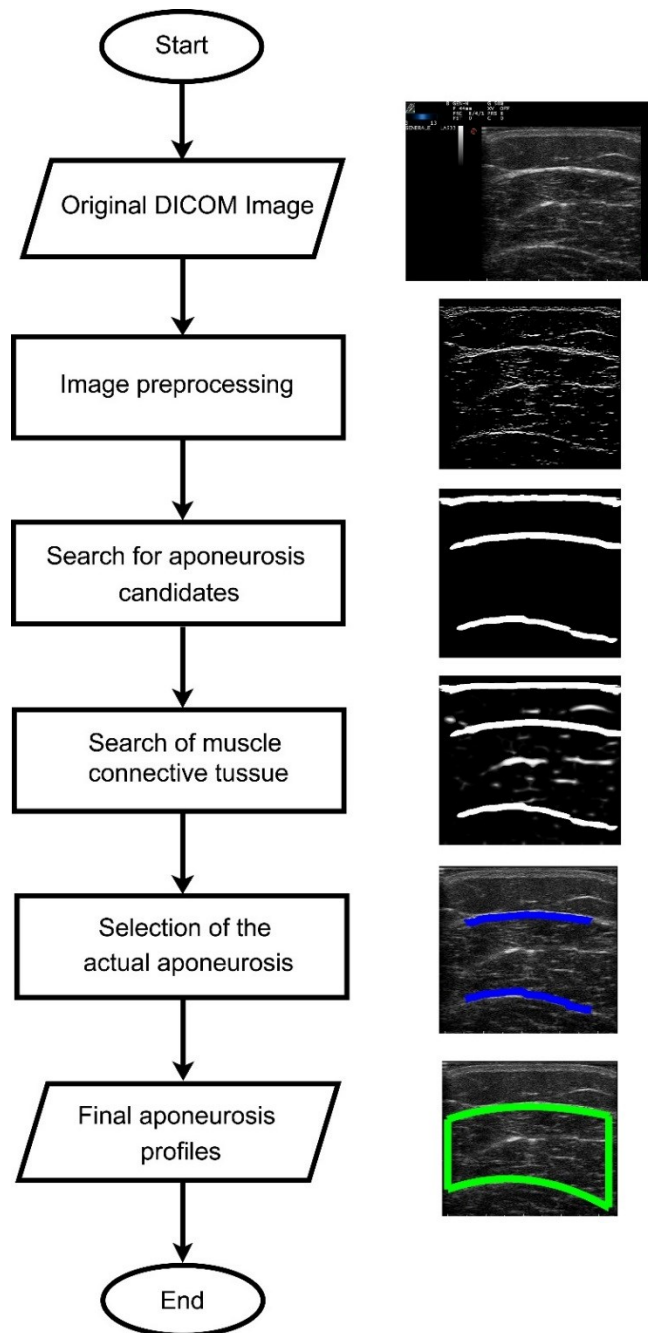


Figure 2. 10:Schematic representation of TRAMA algorithm.

After the original DICOM image cropping (fig 2.11.A), blackening of the first uppermost 2 mm of the dead zone (fig 2.11.B) and the column downsampling of a factor of two, the vertical Sobel gradient of the transversal image is calculated (fig 2.11.C) to ease the aponeuroses search. The same vertical first order derivative Gaussian Filter (FODG) presented in the previous section is applied, with pixel dimension of 9, to enhance the aponeuroses. From this point on, the computation of the VCSA differentiates between mono-compartmental muscles (rectus femoris, vastus lateralis and medial gastrocnemius) and bicompartamental, as the tibialis anterior. In the following, the mono-compartmental muscles processing is described.

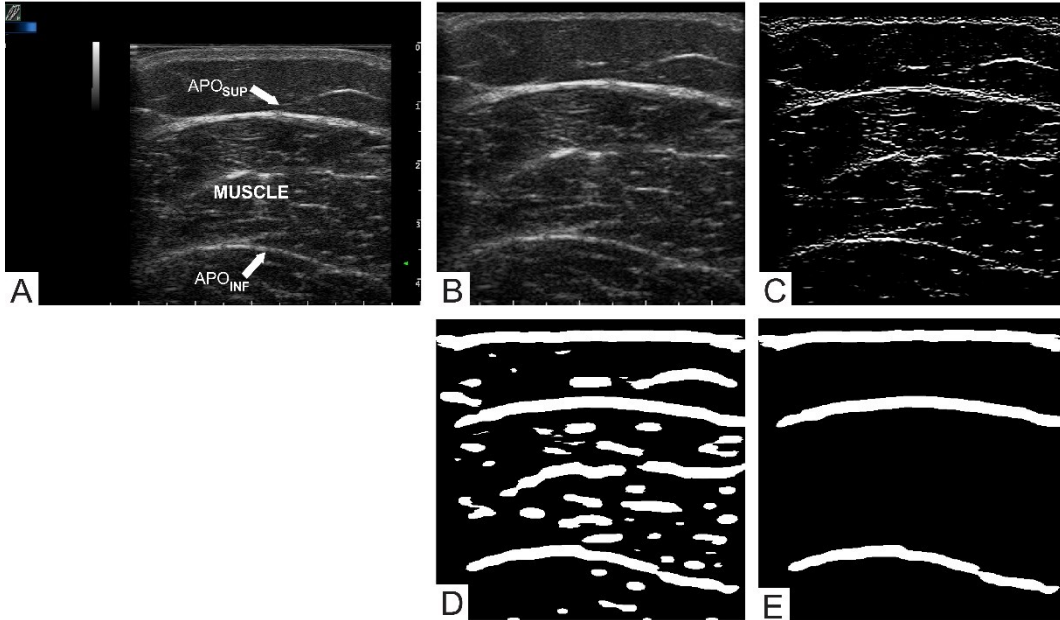


Figure 2. 11: Processing steps of TRAMA algorithm. Panel A – Original DICOM image. Panel B – Image Cropping. Panel C – Vertical Sobel of the image. Panel D – Binary mask of the FODG filter. Panel E – Cleaned FODG mask.

A final FODG mask is generate applying a threshold set at the 80% of the maximum FODG gray level to the FODG output. Figure 2.11.D shows the binary FODG mask in which aponeuroses as well as other structures are identified. Assuming that the aponeuroses have the horizontal size similar to the size of the image, the algorithm labels and approximates all the regions to ellipses to perform a heuristic cleaning; this procedure is applied to delete structures with eccentricity

lower than 0.995 and major axis length shorter than 60% of the image column width. The morphology of the remaining structures is then adjusted with a region filling and edges smoothing (fig 2.11.F).

Since the final FODG binary mask can contain more than two candidate aponeuroses, we check the presence of hyperechoic spots or connective tissue fibers delimited by each pair of borders. The detection of fibrous connective structures is enabled by the application of a multiscale filter. The multiscale approach has been chosen for its intrinsic versatility in the detection of specific shapes and dimensions within an image, according to the choice of parameters values. The implementation of the filter has been taken from Frangi et al. [66] and defined as:

$$V_{\sigma} = \begin{cases} 0 & \text{if } \lambda_2 > 0 \\ e^{\left(-\frac{R_b^2}{2\beta^2}\right)} \left(1 - e^{\left(-\frac{S^2}{2c^2}\right)}\right) & \text{in all other case.} \end{cases}$$

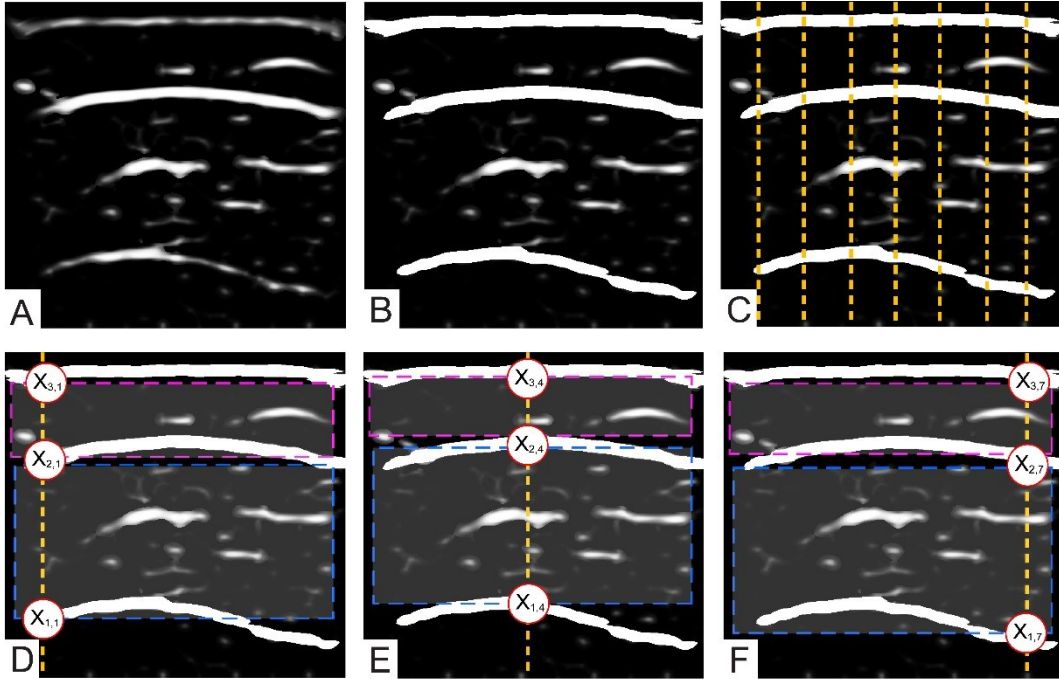


Figure 2. 12: TRAMA heuristic process. Panel A – Fibers mask. Panel B – FODG mask merged with the fibers mask. Panel C – Lines (in yellow) where the heuristic process is performed. Panel D, E, F – Three steps the heuristic procedure, in which 2 ROIs are selected and compared.

where λ_1, λ_2 are the eigenvalues extracted from the Hessian matrix parameters, β and c are thresholds which control the sensitivity of the filter to the measure of $R_b = \frac{|\lambda_1|}{\sqrt{\lambda_2}}$ (blob-like structure) and $S = \sqrt{\lambda_1 + \lambda_2}$ (second order structureness). In this algorithm, the size of the second derivative Gaussian kernel is iteratively computed according to the chosen σ values as a $3\sigma \times 3\sigma$ grid. Possible values of sigma range between 6 – 10 with step size of 2, to reduce the computational cost and optimize the filter response to the structures scale of interest. For this application, β was chosen equal to 0.5 and c equal to 15. The output of the multiscale filtering, called “fibers mask” (fig 2.12.A), is subsequently merged with the FODG mask (fig. 2.12.B).

The new image is processed column-wise and 7 columns between the 12% and 88% with a step of 12% of the entire image width are considered (fig. 2.12.C). This choice has been made to avoid the bilateral 12% of the image where the probe-skin contact along the transversal plane is not usually optimal. Thanks to the goodness of the preprocessing, a quick heuristic search is performed as follows:

1. Starting from the deepest candidate, the algorithm identifies and enumerates all the structures intersected by the corresponding column (fig. 2.12.D). Column points are labelled as $X_{m,n}$, where $m = 1 : \text{Number of candidates aponeurosis}$ and $n = 1 : 7$ according to the column position in the image; the distance between subsequent couples of points, defined as $d = |X_{(m+1),n} - X_{m,n}|$, is taken into account.
2. If there is only one point along the column, the line is discarded, and the analysis moves forward selecting the closest column, with at least two candidate points;
3. If d is higher than 15 mm, the two points are recorded to label all the possible candidate aponeuroses; if no points couple meets this condition, the column is discarded and the analysis steps back to 2);

4. If the condition at step 3 is met and there is only one pair of points, the two points are indicated the deep and the superficial aponeurosis (labelled as APO_{inf} and APO_{sup} in the following) and the analysis proceeds;
5. If multiple couples of points have been considered at step 3, then a further control is performed. Since the candidate aponeuroses enclose muscle with visible spots of connective tissue, a set of regions of interest (defined as $ROI_{((m+1) - m)}$ and referred to each couple of points, is considered: each ROI has height equal to d and width equal to the image width (fig. 2.12.D). The number of connective structures highlighted by the fibers mask and enclosed by the ROIs is then calculated and saved.
6. The pair of points referred to the ROI with the highest number of connective structure indicates the candidate aponeuroses, for that column, as APO_{inf} and APO_{sup} .

At the end of the heuristic process, a voting procedure identifies the highest number of structures occurrences indicated by the pairs of points, selecting the final superficial and deep aponeurosis, as showed in fig. 2.13.A. The final aponeuroses tracing is depicted in fig. 2.13.B and follows the same method described in the MUSA algorithm.

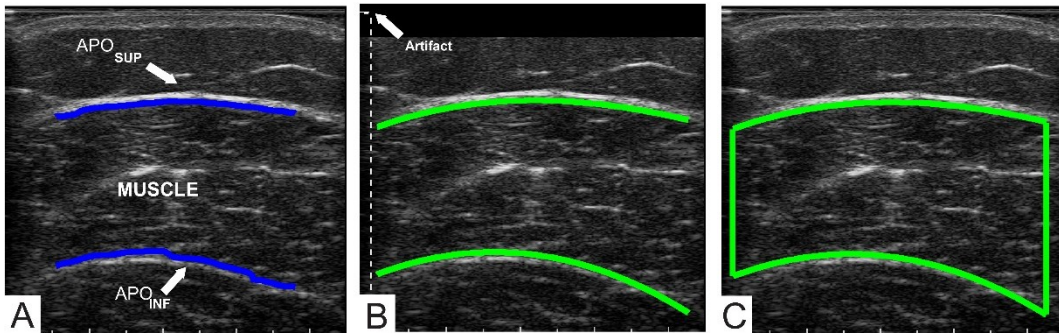


Figure 2. 13: Refinement and VCSA segmentation. Panel A – Profiles obtained at the end of the heuristic process. Panel B – Final tracing of aponeuroses profiles, considering the artifact. Panel C – VCSA muscle result.

Once the interpolated aponeurosis profiles are recognized and traced, a further step of profiles union is needed for the automatically VCSA segmentation. In the case of processing of rectus femoris, vastus lateralis and medial gastrocnemius the segmentation is described in the following.

As previously mentioned, the uppermost 2 mm part of the image, containing the dead zone, is usually discarded from the analysis; along the transversal projection, the anatomical curvature of limbs can reduce the probe-skin contact, and this region displays border effect artifacts, such as white multiple reflections due to air acoustic waves reverberation (fig. 2.13.B). The underlying scanning region is then not suitable for VCSA tracing, since it is featured by an acoustic shadowing effect, impeding the correct shapes' recognition. Therefore, the uppermost 2 mm part of the original image is processed to identify the border regions limits to exclude the underlying scanning area from the computation of the VCSA. This operation is made possible using a simple global thresholding set at the 95% of the maximum gray-level of the uppermost region (fig 2.13.B): once the first artifact strip from the top is detected, all the columns crossed by the artifact are excluded from VCSA tracing and the correct extreme points of the superior profile are selected. If the contact between probe and skin is good, the extreme points of the superior profile is fixed by default at 5% and 95% of the total width of image. The final VCSA is illustrated in fig. 2.13.C.

Tibialis anterior processing

The VCSA extraction for the tibialis anterior muscle is based on a different processing and optimized search of muscle borders, as it will be presented in the following. The transversal ultrasound image of this muscle presents a specific shape

that reminds a sector of a circular crown (fig. 2.14.A), whose limits are usually very clear at the ultrasound examination. For the description of this method a global XY coordinates reference system is taken into account according to the scheme

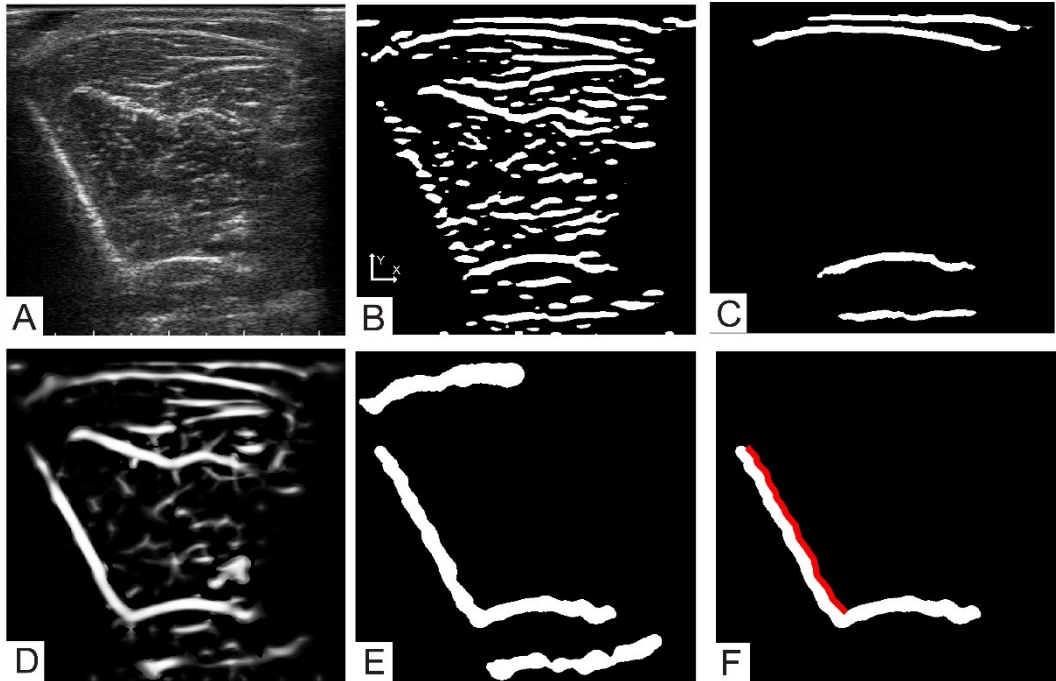


Figure 2. 14: VCSA extraction of tibialis anterior. Panel A – Original Image. Panel B – FODG mask. Panel C - FODG mask after heuristic cleaning. Panel D – Multiscale filtering. Panel E - *L-shape* mask – Panel F – Identification of the *L-shape* and extraction of its vertical profile (in red).

reported in fig.2.14.B After the application of the FODG filter, the FODG binary mask is obtained with an initial thresholding at the 80% of the maximum gray level FODG output (fig. 2.14.B); the mask is then split in two halves along the Y axis and the heuristic cleaning is applied separately on the top half and the bottom half of the image. Structures with major axis length shorter than the 60% and 20% of the image width for the top and the bottom parts respectively are deleted, in order to preserve the anatomic aponeuroses shapes of the tibialis anterior (fig. 2.14.C).

Parallely, the original image is processed with the same multiscale filter presented at the beginning of this session (fig. 2.14.D): in this case, the application of this kernel leads to the identification of the iper-reflective tibia bone interface. The multiscale filtering approach is particularly suitable in the detection of the interface's thickness, which usually present an irregular profile.

Since the tibia bone border is represented, for ultrasound scanning convention (see APPENDIX B), on the bottom left corner of the image, the first upper right

quarter of the filtered image is deleted. The filtered image is then globally thresholded and the cleaning structures step is applied.

The thresholded image presents, in correspondence to the tibia bone interface, a L-shaped structure which also includes the deeper aponeurosis. This mask is named “L-shape binary mask” (fig. 2.14.E).

The *L-shape* structure is selected, firstly, considering the 3 biggest connected structures of the mask. Then, a second criterion is applied to find, among these remaining structures, the one with the biggest bounding box. Once the *L-shaped* structure is identified, the binary mask is processed row-wise to find its vertical profile, in fig. 2.14.F.

Considering this profile in fig 2.15.A, the first point with the highest Y-coordinate is labelled as C, while the last point, namely the interception between the interface and the deep aponeurosis, is marked as D. To ease the recognition of the aponeuroses profiles, the L-shape structure profile, points C and D are reported on the FODG mask. Y-coordinates of points C and D are projected on the central vertical axis of the image, identifying the points C' and D' (fig 2.15.A).

A candidate aponeurosis can be identified as the deep aponeurosis if those two conditions are simultaneously met:

- It is the closest structure to point C' along the vertical axis;
- It intercepts the *L-shape* structure along the horizontal axis.

Once the deep aponeurosis is identified, point B is placed on its superior profile. Subsequently, the distance between C' and B is computed and the search of the superficial aponeurosis is carried out along the vertical central axis. The superficial aponeurosis, labelled by point A (fig 2.15.A) is identified when two conditions are simultaneously met:

- The distance between B and A is higher than 15 mm;
- The distance between B and A is lower than $\frac{3}{2}$ of the distance between C' and B.

From the FODG mask, the right extreme point of the deep aponeurosis, called E, the left and the right extreme points of the superficial aponeurosis named F and G respectively, are considered (fig. 2.15.B).

The lateral interface, the deep and the superficial aponeurosis profiles are interpolated with the application of the *DoG* filter. The lateral and the deep aponeurosis profiles are prolonged to their interception at point H (fig. 2.15.C). To close the tibialis anterior VCSA, the same previously illustrated criteria with the use of the uppermost dead region are applied to find the superficial aponeurosis

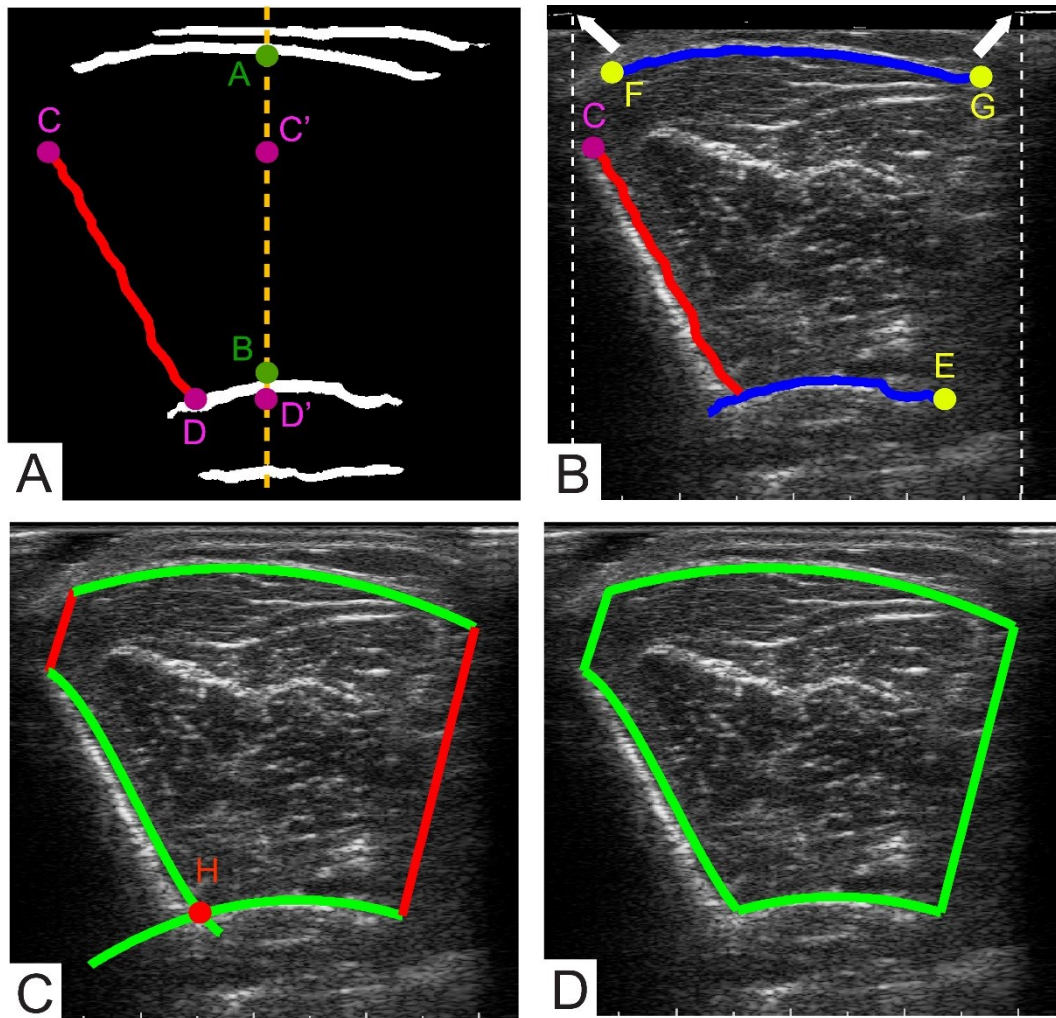


Figure 2. 15: VCSA segmentation of tibialis anterior. Panel A – Identification of point C, D and their projection C', D'. Selection of point A and B according to the distance rules. Panel B – Identification of point E, F, G, on the upper and deep aponeuroses. Panel C -Interpolation, extension of aponeuroses profiles, identification of point H and lines union (in red)- Panel D – Final VCSA selection.

extreme points: point F is connected to the point C on the lateral profile, while point G to point E of the deep aponeurosis, both with a straight line. The position of point F and G are both tuned by the position of the artifact in the dead zone, as previously described. The final result of segmentation is shown in fig.2.15.D.

Performance metric and statistics of the MUSA algorithm

MUSA was tested on the whole database of 200 B-mode ultrasound images. The automatic muscle thickness measurement was obtained by the centerline distance metric. This distance metric has previously been used for thickness measurements [67], [68] and consists in initially determining the centerline between two boundaries. Then, for each point of the centerline, a chord perpendicular to it is plotted. The length of this chord is the measure of muscle thickness in that point. The average distance for all the chords along the centerline is the final centerline distance metric.

In addition to the automatic analysis of muscle thickness, three experienced operators independently and manually measured the muscle thickness in the same 200 images. The manual measurements were performed using the software ImageJ (National Institutes of Health, Bethesda, MD): the operators manually placed five segments between the two muscle aponeuroses at around 10%, 30%, 50%, 70% and 90% of the entire length of the muscle profile in the image. The Euclidean distance between the end points of each segment was calculated and the final manual measurement was obtained as the average of these five distances.

The automatic muscle thickness measurements were compared to the manual measurements obtained by the three operators for each muscle. The comparison was performed by using the Kruskal-Wallis ANOVA (followed by Dunn's post hoc test) and the intra-class correlation coefficient ICC(2,1). To assess the existence of a statistical dependence between manual and automatic measurements, a correlation analysis between the differences and averages of the two measurement methods was also performed using the Spearman test.

Performance metric and statistics of fascicles detection algorithm

The entire set of 30 images was used to validate the fascicle detection algorithm for the extraction and computation of PA and FL. Fascicle detection was applied on single-compartmental ultrasound muscle images (vastus lateralis and medial gastrocnemius) and bicompartamental muscle (tibialis anterior). An example of fascicles detection after the MUSA algorithm processing is presented in fig. 2.16.A. PA is measured as the angle between the fascicle and the deep aponeurosis, whereas FL is calculated as the length between the deep and superficial aponeuroses. To make the estimation of PA and FL reliable, at least 3 fascicles are automatically extracted from the image and the mean \pm standard deviation (SD) values were considered. Moreover, in the automatic algorithm, only fascicles visible for more than the 40% of their entire length were considered in the computation of PA, while only fascicles visible for more than 20% of their length are considered for the estimation of FL.

An experienced blind operator manually extracted three fascicles from single-compartmental muscles and six fascicles from bicompartamental (three for each compartmental); FL and PA measurements were performed using ImageJ. No rule was imposed in the manual selection of fascicles, and the operator could extend the visible aponeuroses profiles on both side to find the “out of image” fascicle’s distal and proximal insertions, as shown in fig. 2.16.B.

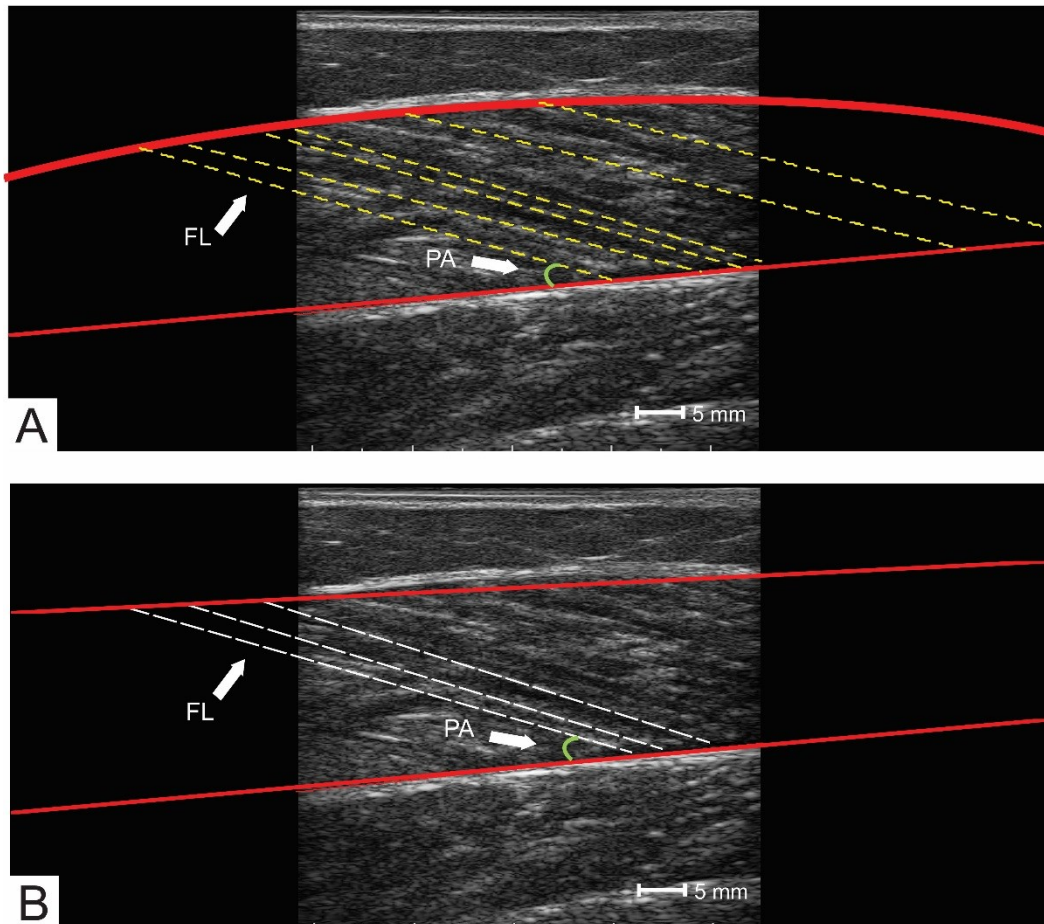


Figure 2. 16: Examples and difference between fascicles length and pennation angle measurements in: Panel A - Automatic approach. Panel B - Manual approach.

Mean values of the overall FL and PA were reported for each image for both the manual and the automatic measurement. The comparison was performed by using the Mann-Whitney U test and the intra-class correlation coefficient ICC (2,1). Manual and automatic measurements were compared performing a correlation

analysis (Spearman test) between the differences and averages of the two measurement methods.

Performance metric and statistics of TRAMA algorithm

TRAMA algorithm was tested on a set of 200 B-mode ultrasound images of rectus femoris, vastus lateralis, tibialis anterior and medial gastrocnemius. To validate this method, two experienced operators manually traced the muscle VCSA profile with a custom written Matlab routine in the same dataset of 200 images.

Mean values and standar deviation of the VCSA were reported for each image for both the manual and the automatic measurement.

The automatic VCSA profiles and area were compared to the manual profiles obtained by the two operators for each muscle. The comparison was performed applying the Dice [69] and Jaccard [70] similarity coefficients for the areas overlapping and measuring the Absolute Error (AE).

The existence of a statistical dependence between the two data sets was assessed by a correlation analysis between the differences and averages of the two measurement methods performing the Spearman test.

2.3 Results

2.3.1 Segmentation results of MUSA algorithm

The MUSA algorithm detected the aponeurosis profiles, and therefore automatically calculated the muscle thickness, in the whole database of 200 images (100% segmentation success rate).

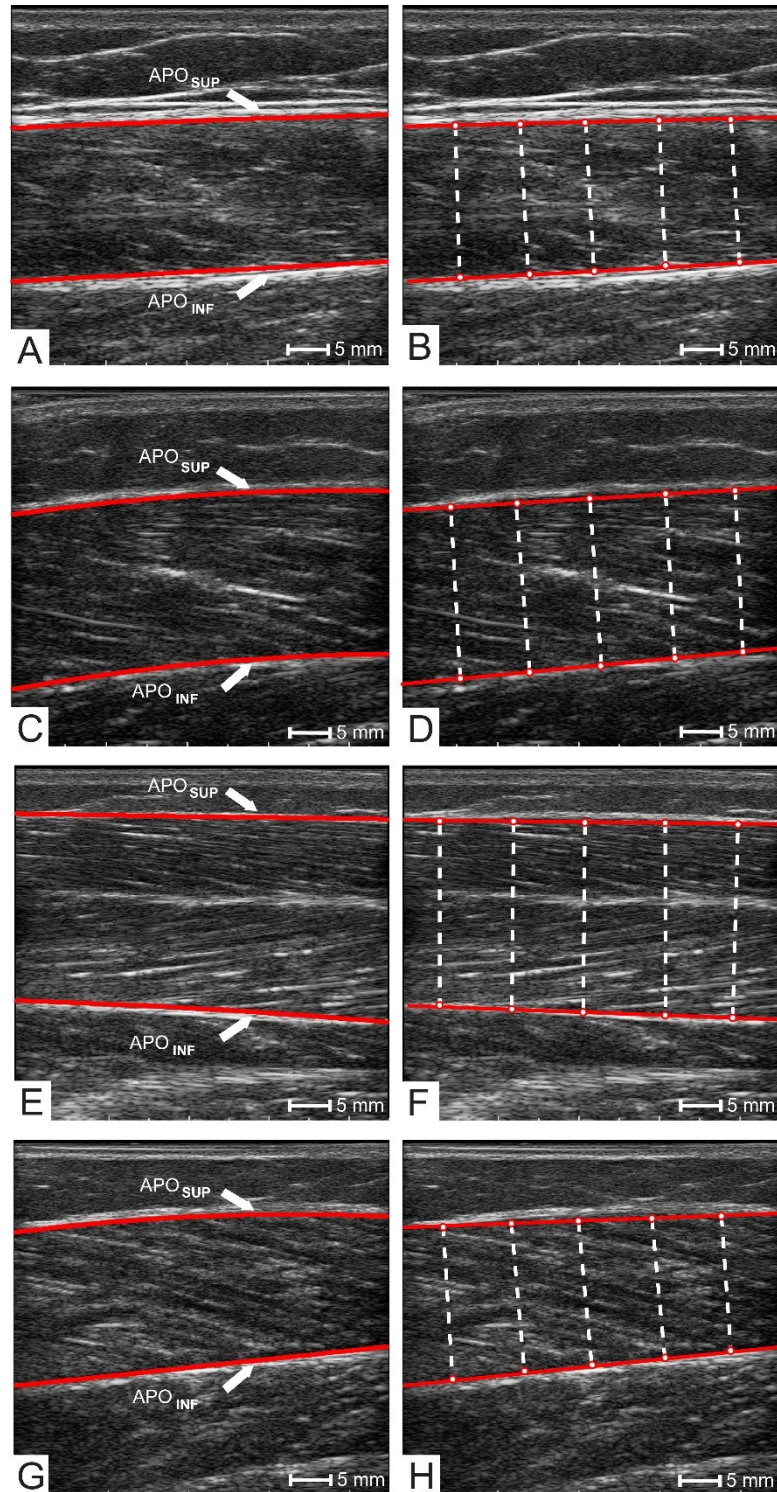


Figure 2.17: Examples of automatic thickness measurement (left panels, A, C, E, G) and manual thickness measurement (performed by one of the three operators - right panels, B, D, F, H) in the four investigated muscles (A and B: rectus femoris, C and D: vastus lateralis, E and F: tibialis anterior, G and H: medial gastrocnemius).

Performance evaluation of MUSA algorithm

Fig. 2.17 shows a representative comparison between the automatic thickness measurement (left panels) and the manual thickness measurement (performed by one of the three operators - right panels) in rectus femoris (fig. 2.17.A – 2.17.B: 18.55 mm vs 19.23 mm), vastus lateralis (fig 2.17.C – 2.17.D: 20.69 mm vs 21.36 mm), tibialis anterior (fig 2.17.E – 2.17.F: 24.11 mm vs 23.96 mm), and medial gastrocnemius muscle (fig 2.17.G – 2.17.H: 18.33 mm vs 18.71 mm). The difference between the automatic and the manual measurement was in the range 0.15 – 0.68 mm (respectively: 0.68 mm for rectus femoris, 0.67 mm for vastus lateralis, 0.15 mm for tibialis anterior, 0.38 mm for medial gastrocnemius).

Table 2.1 showed comparable results obtained by manual and automatic measurements. In fact, no significant differences between the former and the latter measurement were observed for rectus femoris ($P = 0.63$), vastus lateralis ($P = 0.70$), tibialis anterior ($P = 0.85$), and medial gastrocnemius ($P = 0.23$).

The results of the ICC were excellent (range of ICCs: 0.98-0.99) for all muscles both among the three operators and between the manual and automatic measurements.

Muscle	Operator 1 (mm)	Operator 2 (mm)	Operator 3 (mm)	MUSA (mm)
Rectus femoris	22.3 ± 3.8	22.4 ± 3.7	21.7 ± 3.7	21.8 ± 3.8
Vastus lateralis	21.9 ± 4.0	22.0 ± 4.0	21.4 ± 4.0	21.3 ± 4.0
Tibialis anterior	28.2 ± 3.6	28.0 ± 3.6	27.6 ± 3.5	27.9 ± 3.7
Medial gastrocnemius	19.9 ± 3.1	20.0 ± 3.0	19.3 ± 3.1	19.4 ± 3.1

Table 2. 1: Muscle thickness measurements (mean ± SDs) obtained by each of the three operators and by MUSA algorithm for the four considered muscles.

Spearman correlation analysis shows that mean differences between the automatic and manual measurements in the range 0.06 – 0.45 mm and most of the differences between the 95% limits of agreement, thus suggesting that the two measurement methods can be used interchangeably; moreover, no significant

correlation between the differences and means of the two measurements in each of the four muscles (rectus femoris: $R = -0.08$, $P = 0.55$; vastus lateralis: $R = -0.006$, $P = 0.96$; tibialis anterior: $R = -0.15$, $P = 0.29$; medial gastrocnemius: $R = -0.09$, $P = 0.55$), thus indicating that the accuracy of the automatic measurement was not related to the magnitude of the thickness value.

2.3.2 Segmentation results of fascicle detection algorithm

Fig 2.18 shows a representative example of automatic and manual fascicle detection performed on medial gastrocnemius muscle (fig 2.18.A – 2.18.D: FL: 51.4 mm vs 56.9 mm, PA: 26.4° vs 22.5°), tibialis anterior (fig 2.18.B – 2.18.E: FL: 111.3 mm vs 92.9 mm, PA: 3.3° vs 6.4° , upper compartment, FL: 75.9 mm vs 84.4 mm, PA: 12.5° vs 12.0° lower compartment), and vastus lateralis (fig 2.18.C – 2.18.D: FL: 73.0 mm vs 68.7 mm, PA: 11.8° vs 12.9°).

The analysis on the measurements of PA and FL showed, in Table 2.2, comparable results obtained by manual and automatic measurements for all the comparisons in the FL measurements ($P > 0.5$) while all the comparisons were significantly different for PA measurements ($p < 0.05$). The difference between manual and automatic measurements ranged between 2.30 - 35 mm for the FL and $0.5 - 5.65^\circ$ for the PA.

The results of the ICC analysis demonstrate that the agreement was between medium and poor (range of ICCs for FL: 0.75 - 0.35, for PA: 0.56 – 0.2). This finding suggests that the automatic and the manual measurement are not interchangeable when fascicles are detected using different approaches; in addition, fascicles detected by the automatic system are always different from the ones detected by the operator.

Muscle	Fascicles Length		Pennation Angle	
	Automatic (mm)	Manual (mm)	Automatic (°)	Manual (°)
Vastus lateralis	92.3 \pm 15.1	86.5 \pm 16.4	13.3 \pm 2.4	16.1 \pm 2.8
Tibialis anterior (sup)	87.4 \pm 11.7	89.0 \pm 18.3	11.6 \pm 2.8	13.2 \pm 2.7
Tibialis anterior (inf)	85.5 \pm 18.3	81.7 \pm 15.8	5.5 \pm 2.0	8.0 \pm 1.8
Medial gastrocnemius	60.6 \pm 9.3	50.4 \pm 9.3	19.8 \pm 4.4	22.4 \pm 2.8

Table 2. 2: Fascicles length and pennation angle measurements (mean \pm SDs) obtained by the manual operator and by the fascicles detection algorithm for the four considered muscles.

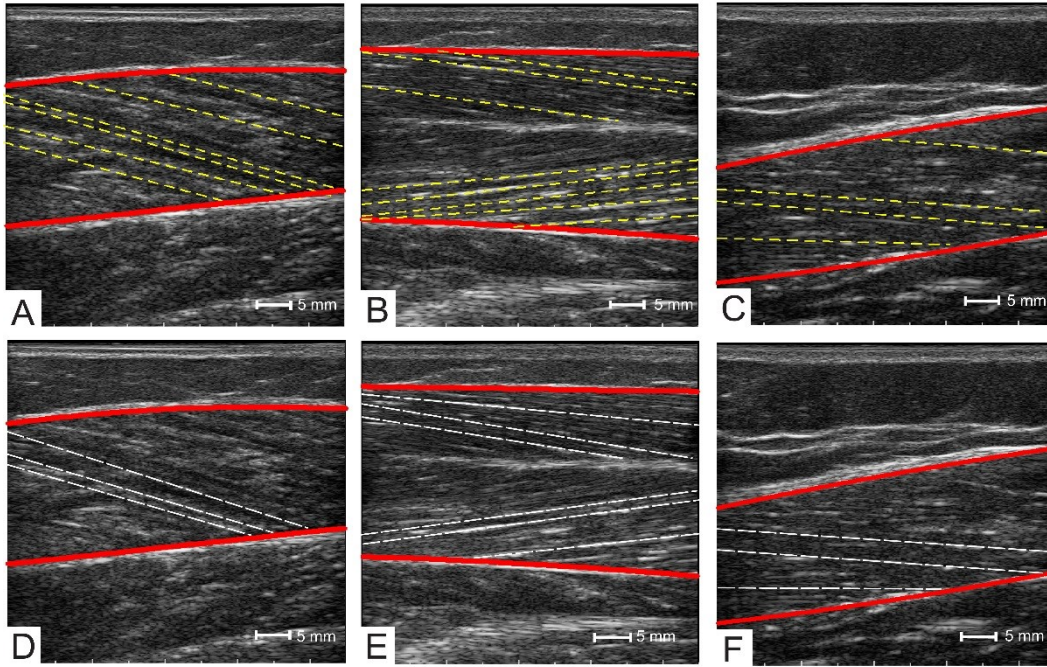


Figure 2. 18: Examples of automatic (upper panels, A, B, C) and manual fascicles detection (lower panels, D, E, F) in the three investigated muscles (A and D: medial gastrocnemius, B and E tibialis anterior, C and F, vastus lateralis).

From the Spearman test, no significant correlation between the differences and means of the two measurements in each of the three muscles (vastus lateralis: PA, $R = -0.27$, $P = 0.44$, FL, $R = 0.07$, $P = 0.83$; tibialis anterior, inferior part : PA, $R = -0.10$, $P = 0.49$, FL, $R = -0.03$, $P = 0.94$; tibialis anterior, superior part : PA, $R = 0.24$, $P = 0.78$, FL, $R = 0.07$, $P = 0.27$; medial gastrocnemius: PA, $R = 0.17$, $P = 0.63$, FL, $R = -0.04$, $P = 0.91$), indicating that the accuracy of the automatic measurement was not related to the fascicles of orientation.

2.3.3 Segmentation results of TRAMA algorithm

The TRAMA algorithm automatically calculated the VCSA, in the whole database of 200 images, with 100% segmentation success rate.

Performance evaluation of TRAMA algorithm

Fig 2.19 shows a representative comparison between the automatic VCSA tracing (left panels) and the manual tracing (performed by one of the two readers, on the right panels) in rectus femoris (fig. 2.19.A – 2.19.B: 865.5 mm^2 vs 886.2 mm^2), vastus lateralis (fig 2.19.C – 2.19.D: 874.8 mm^2 vs 912.3 mm^2), tibialis anterior (fig 2.19.E – 2.19.F: 823.3 mm^2 vs 853.03 mm^2), and medial gastrocnemius muscle (fig 2.19.G – 2.19.H: 845.9 mm^2 vs 868.8 mm^2). The Absolute Error between automatic and the mean of the operators' measurement was in the range $26.6 - 41.1 \text{ mm}^2$ (respectively: 30.6 mm^2 for rectus femoris, 26.6 mm^2 for vastus lateralis, 34.3 mm^2 for tibialis anterior, 41.1 mm^2 for medial gastrocnemius).

Muscle	Operator 1 (mm²)	Operator 2 (mm²)	Mean of Operators (mm²)	TRAMA (mm²)
Rectus femoris	822.0 ± 159.1	796.5 ± 151.1	809.2 ± 154.8	839.8 ± 158.6
Vastus lateralis	864.4 ± 148.3	871.5 ± 136.3	867.9 ± 141.4	894.5 ± 145.9
Tibialis anterior	787.2 ± 144.2	782.5 ± 151.8	784.8 ± 147.0	819.1 ± 151.6
Medial gastrocnemius	771.5 ± 127.9	736.5 ± 124.7	754.0 ± 125.4	795.2 ± 123.1

Table 2. 3 VCSA measurements (mean ± SDs) obtained by each of the two operators and the TRAMA algorithm.

Comparable results can be found in the analysis of the group data (Table 2.3) between manual and automatic segmentations. In fact, no significant differences between the operators and TRAMA algorithm were observed for rectus femoris ($P = 0.32$), vastus lateralis ($P = 0.34$), tibialis anterior ($P = 0.14$), and medial gastrocnemius ($P = 0.10$).

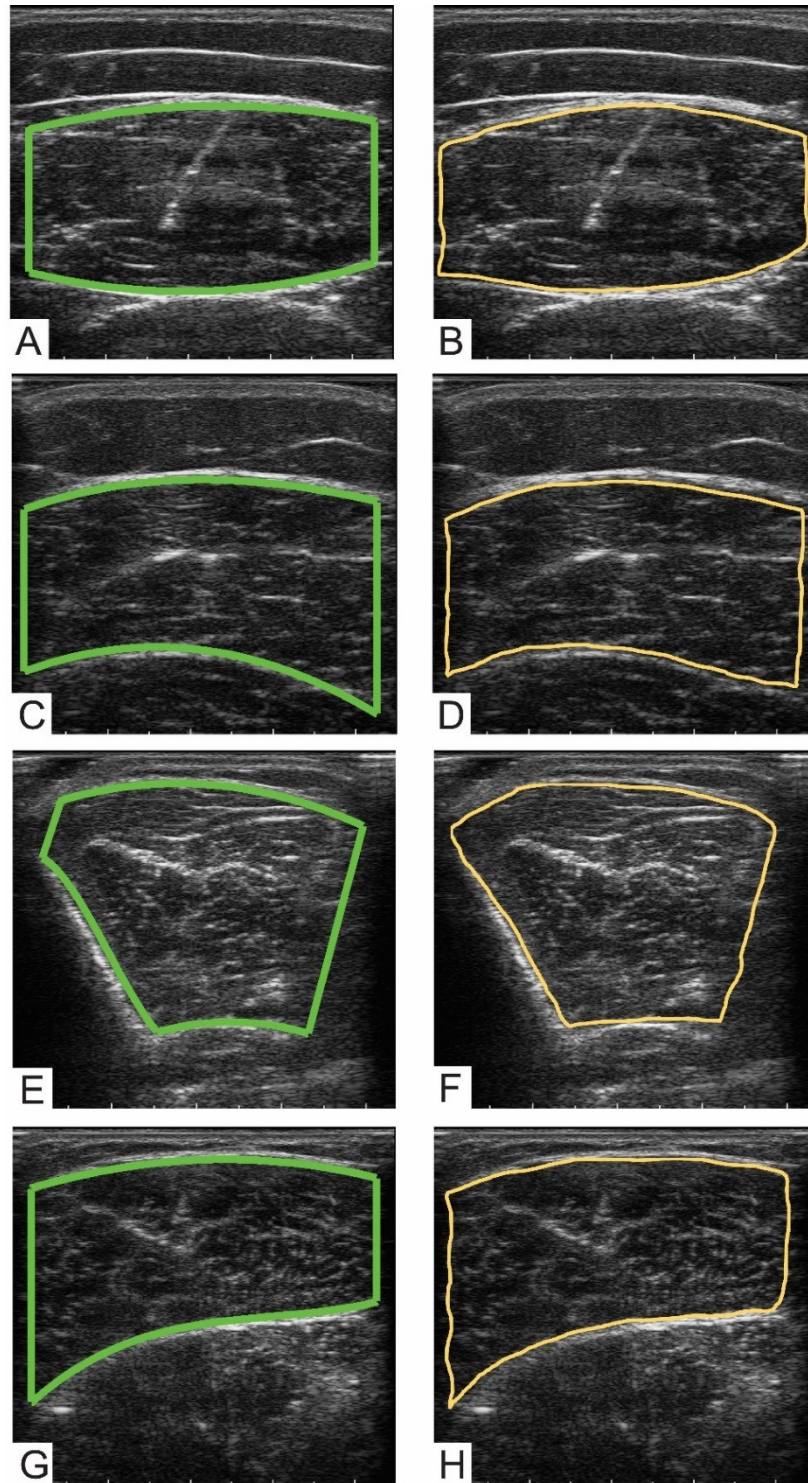


Figure 2. 19: Examples of automatic VCSA measurement (left panels, A, C, E, G) and manual VCSA measurement (performed by one of the three operators - right panels, B, D, F, H) in the four investigated muscles (A and B: rectus femoris, C and D: vastus lateralis, E and F tibialis anterior, G and H medial gastrocnemius).

Muscle	Op1 vs Op 2		Op1 vs TRAMA		Op2 vs TRAMA	
	D	J	D	J	D	J
Rectus femoris	0,95	0,91	0,96	0,93	0,94	0,89
Vastus lateralis	0,96	0,93	0,97	0,94	0,96	0,92
Tibialis anterior	0,95	0,91	0,96	0,92	0,94	0,90
Medial gastrocnemius	0,95	0,92	0,96	0,93	0,95	0,91

Table 2. 4: Dice (D) and Jaccard (J) indices calculated for the comparisons between the two operators and TRAMA algorithm.

Dice and Jaccard similarity indices results are reported in Table 2.4 and show how manual and TRAMA automatic tracing were in excellent agreement (range of Dice's index: 0.94-0.97, range of Jaccard's index: 0.89-0.94) for all muscles and among the two readers.

Spearman test between the mean differences between the automatic and manual measurements suggests that the two segmentation methods can be used interchangeably, since no significant correlation between the differences and means of the two measurements in each of the four muscles (rectus femoris: $R = -0.20$, $P = 0.30$; vastus lateralis: $R = 0.19$, $P = 0.18$; tibialis anterior: $R = 0.12$, $P = 0.40$; medial gastrocnemius: $R = 0.15$, $P = 0.28$), indicating that the accuracy of the automatic segmentation does not depend on the VCSA size.

2.4 Discussion

In this chapter, three fully automatic methods for the measurement of MT, PA, FL and VCSA in musculoskeletal images acquired in the longitudinal plane (i.e., with the probe aligned to the muscle fibers' direction) and in the transversal plane (on the muscle belly) are presented.

The proposed techniques did not require the user interaction and are able to automatically detect different muscles, defining their superficial and deep aponeuroses (MUSA algorithm), fascicles length and pennation angle and the visible cross-sectional area (TRAMA algorithm) in two databases of 200 images. Fascicles detection tool has been validated on a set of 30 longitudinal scans of vastus lateralis, tibialis anterior and medial gastrocnemius muscles (100% segmentation success rate).

The automatic segmentation and quantification of muscle US parameters is a challenging operation, due to the muscle variable in shape and direction, different depth in the images, age and health status of the investigated subject.

The observed robustness of MUSA and TRAMA in skeletal muscle US image segmentation and fascicle detection is mainly due to the use of scale and multi-scale filters (FODG, *DoG*, *ADoG*). In fact, first-order derivative of the Gaussian kernels are able to selectively enhance muscles' profiles without enhancing noise, with very low computational cost. The size and values of the kernel were optimized to match the anatomical size of muscle aponeuroses, fascicles and bone interface (in the tibialis anterior transversal projection).

The comparison between the manual and automatic measurements in MUSA and TRAMA algorithms with the Absolute Error (AE) showed that the mean differences between the former and the latter was below 0.5 mm for MT (AE 2%), and below 42 mm² for the VCSA (AE: 4%), also confirmed by the excellent results of Dice and Jaccard indices. From a clinical point of view, these AEs can be considered irrelevant. In fact, a percentage reduction of AEs in the range 5-10% is required to identify a condition of muscle hypotrophy, while a percentage reduction

above 10% is required to identify a condition of muscle atrophy [18].

Four superficial muscles (rectus femoris, vastus lateralis, tibialis anterior and medial gastrocnemius) were examined in this study as being the most informative for the investigation of neuromuscular disorders and sarcopenia [18], [21], [71]. Future studies are required to test the accuracy and reliability of the MUSA and TRAMA algorithm in the MT, PA, FL, and VCSA extraction for other skeletal muscles. However, from a technical point of view, both algorithms can be used to detect the aponeuroses and borders of any muscle.

MUSA and TRAMA are the first fully-automated systems capable for processing images of muscles with multiple aponeuroses and specific transversal shape of muscles (e.g. tibialis anterior). Being totally automated, these methods could also be used in future works to initialize muscle architectural parameters measurements in dynamic conditions or the PCSA in EVOF acquisitions.

In this work, a fascicles detection algorithm was also proposed, and, to the best of our knowledge, this is the first completely automated algorithm able to measure FL and PA on single and bi-compartmental skeletal muscles that has been manually validated. In previous papers, the validation of FL and PA was briefly conducted on synthetic images [57] and in dynamic conditions [61]; data were reported on Bland-Altman plot without showing the mean values of manual and automatic measurements. Our preliminary results suggest that the automatic and manual measurements are not interchangeable, since the ICC(2,1) show medium and poor values, with an absolute mean difference of 3.41° (AE: 24%) for PA and 11.0 mm for FL (AE: 13%). Our preliminary findings lead to multiple remarks. The automatic fascicle detection is the most challenging task in ultrasound skeletal muscle segmentation. Fascicles show a fading and discontinuous pattern which can be recognized, not effortlessly, by the human perception. For this reason, the fascicle detection algorithm needs to be revised and retested on a higher number of images to improve the overall performance, in particular, in the PA computation. The variability between the automatic and manual measurements is affected by

many conditioning factors, in particular the number of detected fascicles, the portion of fascicles that needs to be prolonged out of the image and the interpolation of curved aponeuroses: a small variation of one of these factors can easily lead to an error of 3-4° in the computation of PA and up to 20 mm for FL.

In the future, further improvements could be specifically addressed in the detection of curved fascicles, considering curvilinear Hough Transform model.

2.5 Conclusion

In this Chapter, MUSA, the fascicles detection algorithm and TRAMA are presented as first fully-automated algorithms that can process images of different skeletal muscles such as rectus femoris, vastus lateralis, medial gastrocnemius, and the tibialis anterior, which presents two compartments in longitudinal projection and a particular shape in the transversal plane. This work proves that the automatic and manual measurement methods could be used interchangeably, considerably reducing the user-dependency of measurements.

Recently, MUSA algorithm has been coupled, by means of dedicated application programming interfaces (API), with a portable pc-based ultrasound device in real-time acquisition and processing of skeletal muscles images. SmartUs ultrasound device (Telemed, Vilnius, Lithuania) equipped with a linear-array transducer (code L12-5L40N) with a variable frequency band (5-12 MHz, selected preferred frequency 9 MHz) was used for this purpose and enthusiastic feedbacks have been received during live DEMO sessions (EXPO Matlab 2016, Milan, Italy)

2.2 References

- [1] P. Fish, *Physics and Instrumentation of Diagnostic Medical Ultrasound*. Wiley, 1990.
- [2] N. D. Reeves, C. N. Maganaris, and M. V. Narici, "Ultrasonographic assessment of human skeletal muscle size," *Eur J App Physiol*, vol. 91, pp. 116–118, 2004.
- [3] C. Caresio, F. Molinari, G. Emanuel, and M. A. Minetto, "Muscle echo intensity: reliability and conditioning factors," *Clin. Physiol. Funct. Imaging*, vol. 35, pp. 393–403, 2015.
- [4] A. Pretorius and J. K. Keating, "Validity of real time ultrasound for measuring skeletal muscle size," *Phys Ther Rev.*, vol. 13, pp. 415–426, 2008.
- [5] C. V. Ruas, R. S. Pinto, C. D. Lima, and P. B. Costa, "Test-Retest Reliability of Muscle Thickness, Echo-Intensity and Cross Sectional Area of Quadriceps and Hamstrings Muscle Groups Using B-mode Ultrasound," *Int. J. Kinesiol. Sport. Sci.*, vol. 5, pp. 35–41, 2017.
- [6] S. Pillen, "Skeletal muscle ultrasound," *Eur. J. Transl. Myol.*, vol. 1, pp. 145–155, 2010.
- [7] C. Gans and W. Bock, "The functional significance of muscle architecture – a theoretical analysis," *Ergeb Anat Entwicklungsgesch*, vol. 38, pp. 115–142, 1965.
- [8] T. Kardel, "Willis and Steno on muscles: rediscovery of a 17th-century biological theory," *J Hist Neurosci*, vol. 5, pp. 100–107, 1996.
- [9] R. a Atkinson, U. Srinivas-Shankar, S. a Roberts, M. J. Connolly, J. E. Adams, J. a Oldham, F. C. W. Wu, O. R. Seynnes, C. E. H. Stewart, C. N. Maganaris, and M. V. Narici, "Effects of testosterone on skeletal muscle architecture in intermediate-frail and frail elderly men," *J. Gerontol. A. Biol. Sci. Med. Sci.*, vol. 65, pp. 1215–1219, 2010.
- [10] R. Lieber, *Skeletal Muscle Structure and Function: Implications for Rehabilitation and Sports Medicine*. Williams & Wilkins, 1992.
- [11] M. Noorkoiv, A. Stavnsbo, P. Aagaard, and A. J. Blazevich, "In vivo assessment of muscle fascicle length by extended field-of-view ultrasonography," vol. 109, pp. 1974–1979, 2010.
- [12] R. R. Scholten, S. Pillen, and A. Verrips, "Quantitative ultrasonography of skeletal muscles in children: normale value," vol. 27, pp. 693–698, 2003.
- [13] I. M. P. Arts, S. Pillen, H. J. Schelhaas, S. Overeem, and M. J. Zwarts, "Normal values for quantitative muscle ultrasonography in adults," *Muscle and Nerve*, vol. 41, pp. 32–41, 2010.
- [14] J. G. Rosenberg, E. D. Ryan, D. Ph, E. J. Sobolewski, J. Michael, B. J. Thompson, G. E. King, and E. D. Ryan, "Reliability of Panoramic Ultrasound Imaging to Simultaneously Examine Muscle Size and Quality of the Medial Gastrocnemius," *Muscle and Nerve*, vol. 49, pp. 736–740, 2014.
- [15] M. V. Narici, M. Flueck, A. Koesters, M. Gimpl, A. Reifberger, O. R. Seynnes, J. Niebauer, J. Rittweger, and E. Mueller, "Skeletal muscle remodeling in response to alpine skiing training in older individuals," *Scand. J. Med. Sci. Sport.*, vol. 21, pp. 23–28, 2011.
- [16] O. R. Seynnes, S. Kamandulis, R. Kairaitis, C. Helland, E.-L. Campbell, M. Brazaitis, A. Skurvydas, and M. V. Narici, "Effect of androgenic-anabolic steroids and heavy strength training on patellar tendon morphological and mechanical properties," *J. Appl. Physiol.*, vol. 115, pp. 84–9, 2013.
- [17] M. D. de Boer, O. R. Seynnes, P. E. di Prampero, R. Pišot, I. B. Mekjavić, G. Biolo, and M. V. Narici, "Effect of 5 weeks horizontal bed rest on human muscle thickness and architecture of weight bearing and non-weight bearing muscles," in *European Journal of Applied Physiology*, 2008, vol. 104, no. 2, pp. 401–407.
- [18] M. A. Minetto, C. Caresio, T. Menapace, A. Hajdarevic, A. Marchini, F. Molinari, and N. A. Maffiuletti, "Ultrasound-Based Detection of Low Muscle Mass for Diagnosis of Sarcopenia in Older Adults," *PM R*, vol. 8, pp. 453–462, 2016.
- [19] M. V. Narici, C. N. Maganaris, N. D. Reeves, and P. Capodaglio, "Effect of aging on human muscle architecture," *J. Appl. Physiol.*, vol. 95, pp. 2229–2234, 2003.

- [20] S. M. Agyapong-Badu S, Warner M, Samuel D, Narici M, Cooper C, “Anterior thigh composition measured using ultrasound imaging to quantify relative thickness of muscle and non-contractile tissue: a potential biomarker for musculoskeletal health,” *Physiol. Meas.*, vol. 35, p. 2165, 2014.
- [21] S. Pillen, I. M. P. Arts, and M. J. Zwarts, “Muscle ultrasound in neuromuscular disorders,” *Muscle and Nerve*. pp. 679–693, 2008.
- [22] Y. Takai, M. Ohta, R. Akagi, E. Kato, T. Wakahara, Y. Kawakami, T. Fukunaga, and H. Kanehisa, “Validity of ultrasound muscle thickness measurements for predicting leg skeletal muscle mass in healthy Japanese middle-aged and older individuals,” *J. Physiol. Anthropol.*, vol. 32, p. 12, 2013.
- [23] T. Abe, J. P. Loenneke, K. C. Young, R. S. Thiebaud, V. K. Nahar, K. M. Hollaway, C. D. Stover, M. A. Ford, M. A. Bass, and M. Loftin, “Validity of Ultrasound Prediction Equations for Total and Regional Muscularity in Middle-aged and Older Men and Women,” *Ultrasound Med. Biol.*, vol. 41, pp. 557–564, 2015.
- [24] Y. Takai, M. Ohta, R. Akagi, E. Kato, T. Wakahara, Y. Kawakami, T. Fukunaga, and H. Kanehisa, “Applicability of ultrasound muscle thickness measurements for predicting fat-free mass in elderly population,” *J. Nutr. Heal. Aging*, vol. 18, pp. 579–585, 2014.
- [25] T. Abe, J. P. Loenneke, and R. S. Thiebaud, “Ultrasound assessment of hamstring muscle size using posterior thigh muscle thickness,” *Clin. Physiol. Funct. Imaging*, vol. 36, pp. 206–210, 2016.
- [26] R. Akagi, Y. Takai, E. Kato, T. Wakahara, M. Ohta, H. Kanehisa, T. Fukunaga, and Y. Kawakami, “Development of an equation to predict muscle volume of elbow flexors for men and women with a wide range of age,” *Eur. J. Appl. Physiol.*, vol. 108, pp. 689–694, 2010.
- [27] J. I. Esformes, M. V. Narici, and C. N. Maganaris, “Measurement of human muscle volume using ultrasonography,” *Eur. J. Appl. Physiol.*, vol. 87, pp. 90–92, 2002.
- [28] M. Ogawa, N. Mitsukawa, M. G. Bembien, and T. Abe, “Ultrasound assessment of adductor muscle size using muscle thickness of the thigh,” *J. Sport Rehabil.*, vol. 21, pp. 244–8, 2012.
- [29] Y. Takai, Y. Katsumata, Y. Kawakami, H. Kanehisa, and T. Fukunaga, “Ultrasound method for estimating the cross-sectional area of the psoas major muscle,” *Med. Sci. Sports Exerc.*, vol. 43, pp. 2000–2004, 2011.
- [30] R. Lieber and J. Fridén, “Functional and clinical significance of skeletal muscle architecture,” *Muscle and Nerve*, vol. 23, pp. 1647–1666, 2000.
- [31] E. Azizi, E. Brainerd, and T. Roberts, “Variable gearing in pennate muscles,” *Proc Natl Acad Sci US A*, vol. 105, pp. 1745–1750, 2008.
- [32] M. V. Narici, T. Binzoni, E. Hiltbrand, J. Fasel, F. Terrier, R. Fisiologia, T. Biomediche, and C. Nazionale, “In vivo human gastrocnemius architecture with changing joint angle at rest and during graded isometric contraction,” vol. 496, pp. 287–297, 1996.
- [33] M. Ito, Y. Kawakami, Y. Ichinose, S. Fukashiro, and T. Fukunaga, “Nonisometric behavior of fascicles during isometric contractions of human muscles,” *J. Appl. Physiol.*, vol. 85, pp. 1230–1235, 1998.
- [34] Y. Kawakami, T. Abe, and T. Fukunaga, “Muscle–fiber pennation angles are greater in hypertrophied than in normal muscles,” *J. Appl. Physiol.*, vol. 74, pp. 2740–2744, 1998.
- [35] C. N. Maganaris, V. Baltzopoulos, and A. J. Sargeant, “measurements of the triceps surae complex architecture in man : implications for muscle function,” *J. Physiol.*, vol. 512, pp. 603–614, 1998.
- [36] T. Fukunaga, Y. Ichinose, M. Ito, Y. Kawakami, and S. Fukashiro, “Determination of fascicle length and pennation in a contracting human muscle in vivo,” *J. Appl. Physiol.*, vol. 82, pp. 354–358, 1997.
- [37] T. Fukunaga, Y. Kawakami, S. Kuni, K. Funato, and S. Fukashiro, “Muscle architecture and function in humans,” *J. Biomech.*, vol. 30, pp. 457–463, 1997.
- [38] A. J. Blazevich, N. D. Gill, and S. Zhou, “Intra- and intermuscular variation in human quadriceps femoris architecture assessed in vivo,” *J. Anat.*, vol. 209, pp. 289–310, 2006.
- [39] M. Ishikawa, T. Finni, and P. . Komi, “Behaviour of vastus lateralis muscle during high intensity SSC

- exercise in vivo.” . *Acta Physiol. Scand.*, vol. 178, pp. 205–213, 2004.
- [40] S. Kurokawa, T. Fukunaga, and S. Fukashiro, “Behavior of fascicles and tendinous structures of human gastrocnemius during vertical jumping,” *J. Appl. Physiol.*, vol. 80, pp. 1349–1358, 2001.
 - [41] Y. Ichinose, Y. Kawakami, M. Ito, H. Kaneshia, and T. Fukunga, “In vivo estimation of contraction velocity of human vastus lateralis muscle during “isokinetic” contraction,” . *J. Appl. Physiol.*, vol. 88, pp. 851–856, 2000.
 - [42] T. Muraoka, Y. Kawakami, M. Tachi, and T. Funkunga, “Muscle fiber and tendon length changes in the human vastus lateralis during slow pedaling,” *J. Appl. Physiol.*, vol. 91, pp. 2035–2040, 2001.
 - [43] J. Wakeling, K. Uehli, and A. Rozitis, “Muscle fibre recruitment can respond to the mechanics of the muscle contraction,” *J. R. Soc. Interface*, vol. 3, pp. 533–544, 2006.
 - [44] R. M. Alexander and A. Vernon, “The dimension of knee and ankle muscles and the forces they exert,” *J. Hum. Mov. Stud.*, vol. 1, pp. 115–123, 1975.
 - [45] C. Gans, “Fiber architecture and muscle function,” *Exerc. Sport. Sci. Rev.*, vol. 10, pp. 160–207, 1982.
 - [46] J. Ahtiainen, M. Hoffren, J. Hulmi, M. Pietikainen, A. Mero, J. Avela, and K. Hakkinen, “Panoramic ultrasonography is a valid method to measure changes in skeletal muscle cross-sectional area,” *Eur J Appl Physiol*, vol. 108, pp. 273–279, 2010.
 - [47] J. M. Scott, D. S. Martin, R. Ploutz-snyder, T. Matz, T. Caine, M. Downs, R. Buxton, J. W. Ryder, and L. Ploutz-snyder, “Panoramic ultrasound : a novel and valid tool for monitoring change in muscle mass,” *J. Cachexia. Sarcopenia Muscle*, vol. 8, pp. 475–481, 2017.
 - [48] K. D. Seymore, Z. J. Domire, P. Devita, P. M. Rider, and A. S. Kulas, “The effect of Nordic hamstring strength training on muscle architecture , stiffness , and strength,” *Eur. J. Appl. Physiol.*, vol. 117, pp. 943–953, 2017.
 - [49] K. Tayashiki, K. Hirata, K. Ishida, and H. Kanehisa, “Associations of maximal voluntary isometric hip extension torque with muscle size of hamstring and gluteus maximus and intra - abdominal pressure,” *Eur. J. Appl. Physiol.*, vol. 117, pp. 1267–1272, 2017.
 - [50] R. R. Estes, A. M. Y. Malinowski, M. Piacentini, D. Thrush, E. Salley, C. Losey, and E. Hayes, “The Effect of High Intensity Interval Run Training on Cross- sectional Area of the Vastus Lateralis in Untrained College Students,” *Int. J. Excercise Sci.*, vol. 10, pp. 137–145, 2017.
 - [51] M. N. M. Blue, A. E. Smith-Ryan, E. T. Trexler, and K. R. Hirsch, “The effects of high intensity interval training on muscle size and quality in overweight and obese adults,” *J. Sci. Med. Sport*, pp. 1–6, 2017.
 - [52] S. Sipilä and H. Suominen, “Ultrasound imaging of the quadriceps muscle in elderly athletes and untrained men,” *Muscle and Nerve*, vol. 14, pp. 527–533, 1991.
 - [53] T. K. K. Koo, C. Wong, and Y. Zheng, “Reliability of Sonomyography for Pectoralis Major Thickness Measurement,” *J. Manipulative Physiol. Ther.*, vol. 33, pp. 386–394, 2010.
 - [54] A. Wong, K. M. Gallagher, and J. P. Callaghan, “Computerised system for measurement of muscle thickness based on ultrasonography,” *Comput. Methods Biomech. Biomed. Engin.*, vol. 16, pp. 1–7, 2012.
 - [55] P. Han, Y. Chen, L. Ao, G. Xie, H. Li, L. Wang, and Y. Zhou, “Automatic thickness estimation for skeletal muscle in ultrasonography: evaluation of two enhancement methods,” *Biomed. Eng. Online*, vol. 12, p. 6, 2013.
 - [56] S. Ling, Y. Zhou, Y. Chen, Y. Q. Zhao, L. Wang, and Y. P. Zheng, “Automatic tracking of aponeuroses and estimation of muscle thickness in ultrasonography: A feasibility study,” *IEEE J. Biomed. Heal. Informatics*, vol. 17, pp. 1031–1038, 2013.
 - [57] M. Rana, G. Hamarneh, and J. M. Wakeling, “Automated tracking of muscle fascicle orientation in B-mode ultrasound images,” *J. Biomech.*, vol. 42, pp. 2068–2073, 2009.
 - [58] N. J. Cronin, C. P. Carty, R. S. Barrett, and G. Lichtwark, “Automatic tracking of medial

- gastrocnemius fascicle length during human locomotion standing balance Automatic tracking of medial gastrocnemius fascicle length during human locomotion,” *JJ App Physiol*, vol. 111, pp. 1491–1496, 2015.
- [59] J. Darby, E. F. Hodson-tole, N. Costen, and I. D. Loram, “Automated regional analysis of B-mode ultrasound images of skeletal muscle movement Automated regional analysis of B-mode ultrasound images of skeletal muscle movement,” *J Appl Physiol*, vol. 112, pp. 313–327, 2015.
 - [60] Y. Zhou, J. Li, G. Zhou, and Y. Zheng, “Dynamic measurement of pennation angle of gastrocnemius muscles during contractions based on ultrasound imaging,” *Biomed. Eng. Online*, vol. 11, pp. 9–11, 2012.
 - [61] G. Zhou, P. Chan, and Y. Zheng, “Automatic measurement of pennation angle and fascicle length of gastrocnemius muscles using real-time ultrasound imaging,” *Ultrasonics*, vol. 57, pp. 72–83, 2015.
 - [62] L. M. J. Florack, B. M. ter Haar Romeny, J. J. Koenderink, and M. A. Viergever, “Scale and the differential structure of images,” *Image Vis. Comput.*, vol. 10, pp. 376–388, 1992.
 - [63] N. Otsu, “A threshold selection method from gray-level histograms,” *IEEE Trans. Syst. Man. Cybern.*, vol. 9, pp. 62–66, 1979.
 - [64] R. O. Duda and P. E. Hart, “Use of the Hough transformation to detect lines and curves in pictures,” *Comm. ACM*, vol. 15, pp. 11–15, 1971.
 - [65] C. N. Maganaris and V. Baltzopoulos, “Predictability of in vivo changes in pennation angle of human tibialis anterior muscle from rest to maximum isometric dorsiflexion,” *Eur. J. Appl. Physiol. Occup. Physiol.*, vol. 79, pp. 294–297, Feb. 1999.
 - [66] A. F. Frangi, W. J. Niessen, K. L. Vincken, and M. a Viergever, “Multiscale vessel enhancement filtering,” *Medial Image Comput. Comput. Invervention - MICCAI'98. Lect. Notes Comput. Sci. vol 1496*, vol. 1496, pp. 130–137, 1998.
 - [67] F. H. Sheehan, E. L. Bolson, H. T. Dodge, D. G. Mathey, J. Schofer, and H. W. Woo, “Advantages and applications of the centerline method for characterizing regional ventricular function,” *Circulation*, vol. 74, pp. 293–305, 1986.
 - [68] L. Saba, F. Molinari, K. M. Meiburger, M. Piga, G. Zeng, U. Rajendra Acharya, A. Nicolaides, and J. S. Suri, “What is the correct distance measurement metric when measuring carotid ultrasound intima-media thickness automatically?,” *Int. Angiol.*, vol. 31, pp. 483–489, 2012.
 - [69] L. R. Dice, “Measures of the Amount of Ecologic Association Between Species,” *Ecology*, vol. 26, pp. 297–302, 1945.
 - [70] P. Jaccard, “The distribution of the flora in the alpine zone,” *New Phytol.*, vol. 11, pp. 37–50, 1912.
 - [71] T. Abe, R. S. Thiebaud, J. P. Loenneke, M. Loftin, and T. Fukunaga, “Prevalence of site-specific thigh sarcopenia in Japanese men and women,” *Age (Omaha)*, vol. 36, pp. 417–426, 2014.

Chapter 3

Quantitative skeletal muscle ultrasound imaging

Part of this chapter has been published as:

C. Caresio, F. Molinari, G. Emanuel and M.A. Minetto, **Muscle echo intensity: reliability and conditioning factors.**, *Clin Physiol Funct Imaging*, 2015;35: 393–403.

and

F. Molinari, C. Caresio, U.R. Acharya, M.R.K. Mookiah and M.A. Minetto, **Advances in Quantitative Muscle Ultrasonography Using Texture Analysis of Ultrasound Images.**, *Ultrasound Med Biol*, 2015, 41: 2520–2532.

3.1 Introduction

As previously mentioned in Chapter 2, B-Mode ultrasonography is an enabling diagnostic technique for the architectural characterization of skeletal muscles. Muscle ultrasound is a convenient, for its cost and safety, in the study of both normal healthy and pathological muscles tissue [1].

Along the transversal projection, where the cross-sectional area is visible, normal healthy muscles appear darker, i.e. have low echo intensity, compared to the aponeuroses and the subcutaneous tissue layer. Skeletal muscles exhibit an internal characteristic pattern of fibrous endomysial tissue, which appear white at the ultrasound examination. The interaction between the ultrasound beam and the endomysium generates hyperechoic reflections, caused by the difference of acoustical impedance. Healthy muscle usually contains only little fibrous tissue and few reflections, which can be qualitatively evaluated in the clinical practice.

The normal muscle structure can be disrupted in myopathic and neuropathic diseases and muscle disorders [2]–[7] by the presence of fat and fibrous infiltrations, resulting in the increase of muscle reflections. Infiltrations can present a specific distribution within the muscle [1], [4]. According to recent studies, the muscle overall echogenicity appears homogenous in myopathies and inhomogeneous in neuropathies [2], [5], but this evaluation can only be performed visually.

Fat infiltrations within the muscle is better known, in clinical practice, with the name of myosteatorsis [8], [9]: body fat accumulation during weight gain (obesity) or for metabolic disorders (diabetes, hormone deficit or excess), sedentary and aging [10] are related to the increase of ectopic storage of adipose tissue within skeletal muscle, with a consequent functional impairment.

Muscle quality can be assessed quantitatively through the gray-scale analysis of a given region of interest (ROI) with the extraction of the Mean Echo Intensity (MEI). Upper and lower limbs muscles are usually investigated in the study of skeletal muscle disorders. The ROI is usually manually placed by an expert

operator, selected to include as much of the muscle as possible avoiding the surrounding epymisium and bones, and it often corresponds to the visible cross-sectional area (VCSA) displayed by the ultrasound transducer in conventional B-mode ultrasonography and already discussed in Chapter 2 [3], [6], [11].

However, the use of muscle echo intensity in the characterization of muscle quality presents a considerable number of limitations. First of all, there is no specific state of art in the computation of MEI in terms of ROI size, shape and location. In fact, MEI obtained by the VCSA can be biased by the presence of internal fasciae (as in the case of the tibialis anterior or the rectus femoris); besides, the choice of the ROI plays a fundamental role in the muscle inhomogeneity investigation. Moreover, MEI computation is critically influenced by the ultrasound system settings in terms of gain [12]–[14], making difficult data comparisons in multicenter trials. This aspect impedes the creation of a standard MEI values database for healthy controls and limits the comparison with myopathic and neuropathic patients only to stand-alone US device-dependent studies.

Finally, the characteristic generated by the presence of intramuscular fat and fibrous tissue in endocrine, myopathic or neuropathic diseases cannot be fully described using a mean luminance gray level value, since this parameter is unable to detect the fine “coarseness” also called texture, of the US muscle images.

Compared to first order descriptors, as MEI, which are extracted from the luminance histogram of the image, higher-order texture features offer better characterization performance [15], [16], since they are intensity invariant [17]–[19] and proven to be informative in the investigation of animal intramuscular fat content [20], in human studies of arterial surface roughness [21], [22], breast [23] and ovarian tumors [15], [24], thyroid lesions [17], [25] and liver images [26], [27].

Few previous works have attempted to develop quantification methods to overcome the limitation of MEI in measuring the image texture. Maurits et al. proposed quantitative variables, obtained by density analysis able to characterize

the presence of patches of high echogenicity, to differentiate between myopathies and neuropathies [2] and to distinguish between healthy muscles and neuromuscular diseases [28]. Gdynia et al. used the muscle echo intensity, the first order entropy, and the fractal dimension to analyze the ultrasound images of tibialis anterior and medial gastrocnemius muscles of healthy patients and patients affected by myopathies and motor neuron disorders to distinguish between healthy and pathological muscles [29].

To the best of our knowledge, in previous studies, only linear and first-order descriptors are used to characterize the texture of different skeletal muscles. Moreover, no previous study has been proposed in the characterization of muscle texture between healthy subjects and pathological patients.

In this chapter, an initial study on skeletal muscle quantification with MEI in healthy subjects with the use of different size and location of manual ROIs selection is reported [30]. In a second study, we characterized the image texture of five skeletal muscles of healthy men and women using different texture features.

In the last part of the chapter, a preliminary study on automatic muscle VCSA characterization by texture analysis is proposed in the differentiation of healthy and pathological muscles.

3.1 Muscle echo intensity reliability assessment on healthy controls

3.1.1 Materials and Methods

Twenty volunteers (10 females, 26.0 ± 2.3 years, body mass index: 20.7 ± 2.2 kg/m² and 10 males, age 30.2 ± 5.6 years; body mass index 23.3 ± 2.6 kg/m²) whose status was assessed by clinical examination, were examined to assess the reliability of MEI on healthy controls. Both sides of the following five muscles were investigated: biceps brachii, rectus femoris, vastus lateralis, tibialis anterior and

medial gastrocnemius. For each muscle, three consecutive scans were acquired. Detailed description of the ultrasound setting device and protocol are reported in APPENDIX A and B.

A VCSA ROI, called hereinafter “maximum ROI”, was chosen in each scan to include as much as the muscle as possible, without bone and perimysial layer.

In Fig. 3.1 maxima ROIs examples are shown in the medial gastrocnemius (panel A) and tibialis anterior (panel C) for a representative subject. Furthermore,

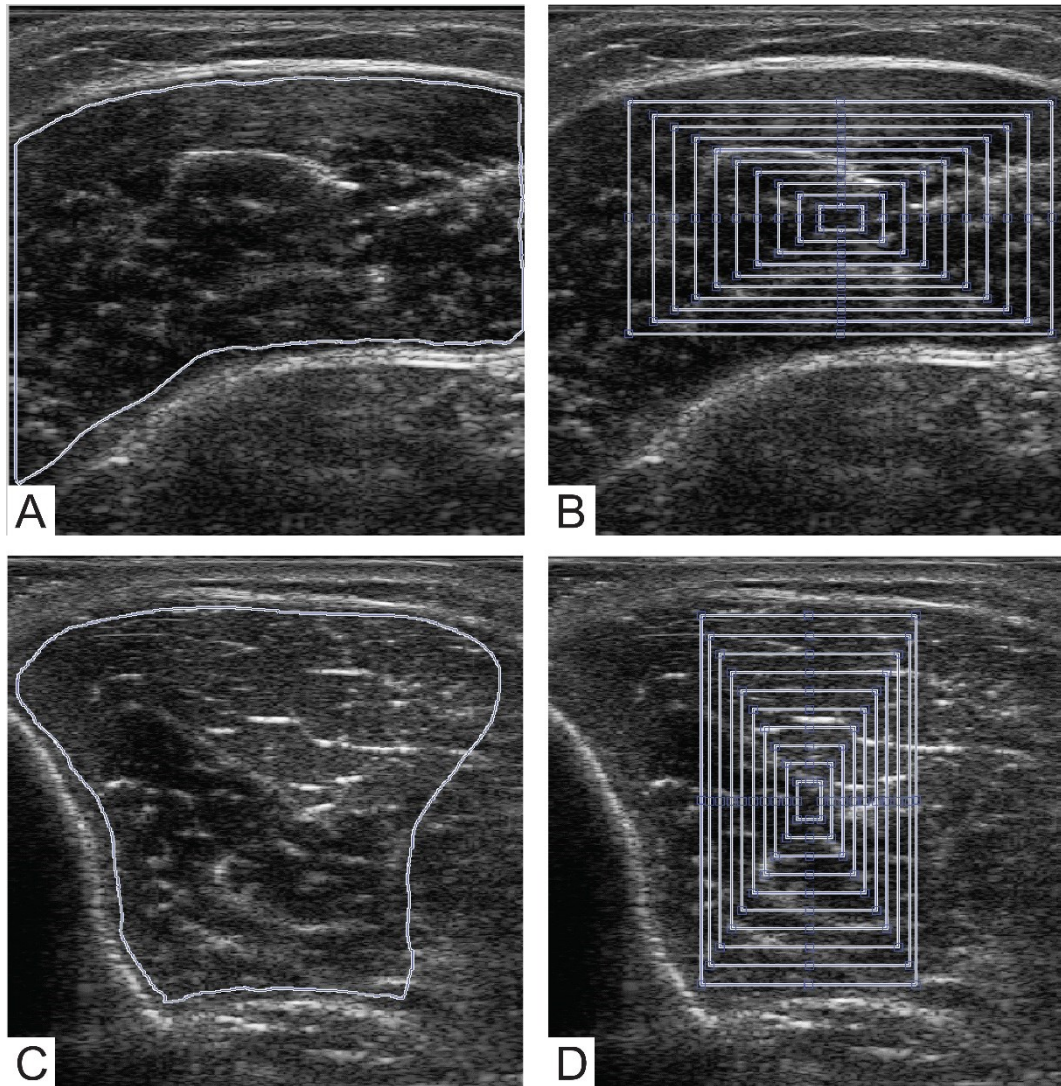


Figure 3. 1: Examples of maxima ROIs extracted from medial gastrocnemius (panel A) and tibialis anterior (panel C) compared with maxima ROIs and the 9 concentric ROIs automatically obtained (panel B and D).

a rectangular ROI was chosen in each scan to include as much of the muscle as possible without any bone or surrounding fascia. We named this ROI as “maximum rectangular ROI”. A series of nine rectangular concentric ROIs to the maximum were obtained by progressively decreasing the side by 10%. Figure 1 reports examples of all rectangular ROIs ($n=10$) considered in the medial gastrocnemius and tibialis anterior muscles (panels B and D). Additionally, two other ROIs were chosen in the tibialis anterior to compare the MEI among the following four ROIs presenting different shape, size, and position, as reported in Fig. 3.2: square-shaped ROI positioned in the lower muscle portion vs rectangular-shaped ROI positioned in the upper muscle portion vs maximum rectangular ROI vs maximum ROI.

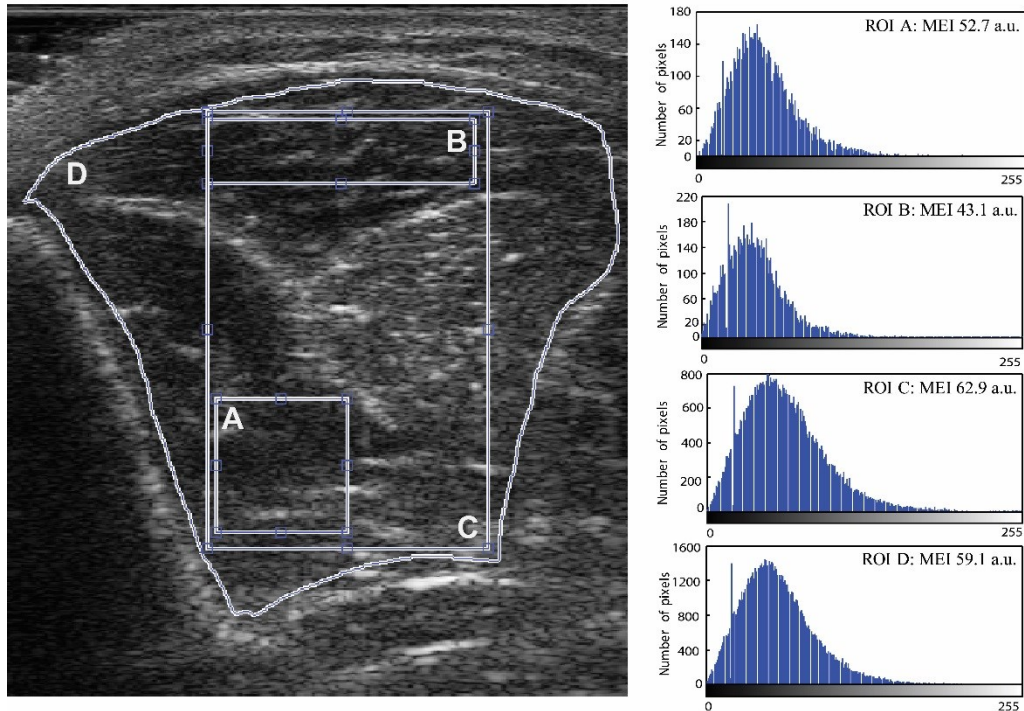


Figure 3. 2: Example of extraction and MEIs computation on 4 ROIs of tibialis anterior muscle. Panel A: square-shaped ROI positioned in the lower muscle portion; panel B: rectangular-shaped ROI positioned in the upper muscle portion; panel C maximum-squared ROI; panel D maximum ROI.

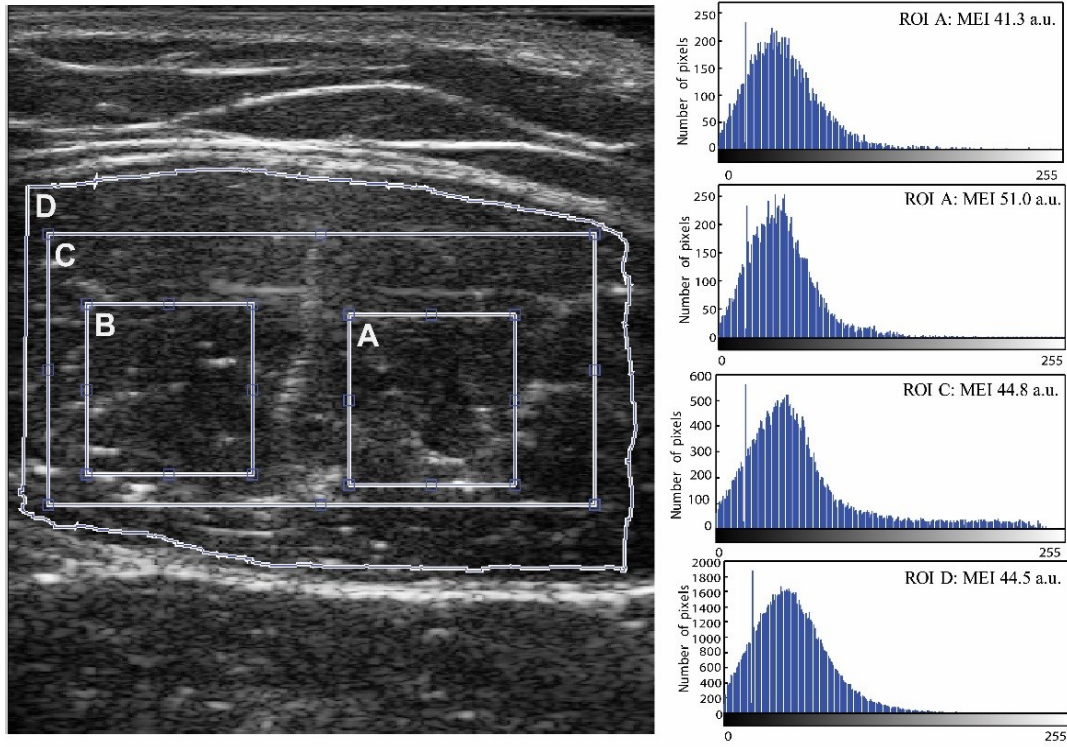


Figure 3. 3: Example of extraction and MEIs computation on 4 ROIs of rectus femoris muscle. Panel A: lateral ROI; panel B: medial ROI; panel C maximum-squared ROI; panel D maximum ROI.

Using the same approach, MEI of two different portions of the rectus femoris was also assessed: lateral portion of the muscle vs median portion of the muscle, compared with the bigger ROIs previously described in Fig. 3.3. The dimension of 70 mm^2 and 165 mm^2 and the position of the former two ROIs for tibialis anterior and rectus femoris respectively were chosen to be the same in all subjects. Echo intensity reliability across the different sized ROIs ($n=11$: 10 rectangular ROIs + 1 maximum ROI) considered in each scan was assessed using ICC(2,1) since it estimates the intra-image reliability (agreement). The coefficient of variation (CV %) was also calculated. Echo intensity reliability across the three scans acquired from each muscle was assessed using ICC(3,1) since it estimates the inter-image reliability (consistency). Further details in the choice of the sampling size can be found in [30].

All the statistical analysis was conducted applying non-parametric tests: the Mann-Whitney U test was used for comparisons between the two genders and

between maxima ROIs (maxima ROIs vs maxima rectangular ROIs), while the Kruskal-Wallis ANOVA (followed by Dunn's post-hoc test) was adopted for comparing muscle echo intensity among the five muscles and among the four ROIs considered in the tibialis anterior and rectus femoris muscles.

3.1.2 Results

ICC(2,1) agreement among different sized ROIs ranged from 0.542 to 0.860 and CV values ranged from 6-7% to 11-5 % (Table 3.1). ICC(3,1) consistency among equal sized ROIs of the three scans was function of the ROI size. As shown in Fig. 3.4, MEI consistency across different scans and ROI size present a non-linear relationship for all muscles. In general, a ROI dimension of 9-6 % of the maximum ROI (or 16% of the maximum rectangular ROI) is sufficient to obtain ICC(3,1) higher than 0.7 (considered good). MEI reliability between rectangular ROIs and maxima ROIs was confirmed by the CV ($< 10\%$ in all muscle).

Since no significant differences in MEI were observed between the dominant and non-dominant sides ($P > 0.05$, data not reported), pooled data for the two sides were used in the comparison between ROIs and genders.

Comparisons between maxima rectangular ROIs and maxima ROIs for pooled data from males and females (data reported in [30]) shows that MEIs of only biceps brachii and tibialis anterior were significantly higher for the maxima rectangular ROIs (no significant comparison were found for rectus femoris, vastus lateralis and medial gastrocnemius ROIs)

In Table 3.2, MEI appears to be comparable between maxima ROIs and maxima rectangular ROIs for all the muscles. Moreover, females' MEI was higher than males for rectus femoris, tibialis anterior and medial gastrocnemius, while comparable for biceps brachii and vastus lateralis.

Scan	Biceps brachii		Medial gastrocnemius		Rectus femoris		Tibialis anterior		Vastus lateralis	
	R	L	R	L	R	L	R	L	R	L
1	0.73 (7.7)	0.79 (6.7)	0.67 (8.7)	0.54 (7.1)	0.82 (8.6)	0.86 (10.7)	0.74 (9.6)	0.76 (11.5)	0.76 (9.5)	0.68 (7.8)
2	0.72 (7.9)	0.72 (7.1)	0.68 (9.6)	0.70 (7.4)	0.84 (9.5)	0.78 (7.9)	0.62 (10.4)	0.68 (10.3)	0.71 (9.2)	0.72 (8.0)
3	0.76 (6.7)	0.72 (7.4)	0.76 (9.5)	0.72 (7.7)	0.86 (9.2)	0.82 (8.0)	0.70 (8.9)	0.68 (10.7)	0.69 (8.3)	0.70 (7.7)

Table 3. 1: ICC(2,1) values calculated for each scan acquired from the two sides of the five muscles and respective CV (%).

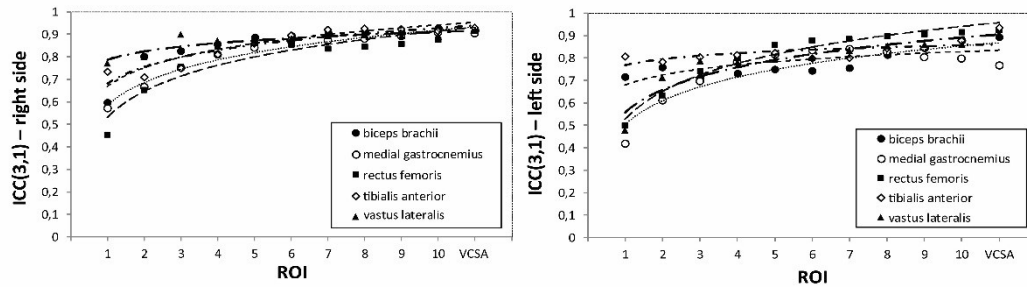


Figure 3. 4: ICC(3,1) values among equal sized ROIs of the three scans as a function of the ROI size for the two sides and for all the muscles.

In the comparison of muscle compartments, the analysis of the whole group of twenty subjects showed that the MEI was comparable ($P > 0.05$) among three portions of the tibialis anterior (inferomedial portion, maximum rectangular ROI, maximum ROI), while it was significantly lower ($P < 0.05$) for the ROI positioned in the upper portion compared to the maximum rectangular ROI. In the same way, the analysis extended to the whole group of subjects proved that the rectus femoris MEI was comparable ($P > 0.05$) among three portions of the rectus femoris (lateral

portion.; maximum rectangular; maximum ROI), while it was significantly higher ($P < 0.05$) for the ROI positioned in the median portion compared to both the maximum rectangular ROI and the maximum ROI.

Muscle	Males		Females		Max ROI vs. Max rect ROI (P value)	Males vs Females (P values)	
	Max ROI	Max rect ROI	Max ROI	Max rect ROI		Max ROI	Max rect ROI
Biceps brachii	63.6 (5.7)	65.7 (6.7)	65.5 (7.9)	69.0 (9.2)	0.10	0.25	0.14
Rectus femoris	48.9 (6.9)	48.7 (7.2)	53.3 (5.5)	53.6 (5.1)	1.00	0.05	0.01
Vastus lateralis	48.2 (5.5)	48.8 (6.6)	53.3 (9.9)	54.9 (10.1)	0.58	0.12	0.08
Tibialis anterior	58.7 (7.9)	61.0 (8.3)	64.5 (8.8)	65.8 (9.0)	0.31	0.03	0.07
Medial gastrocnemius	50.8 (6.5)	51.6 (6.6)	53.8 (6.5)	54.8 (6.6)	0.48	0.05	0.05

Table 3. 2: MEI (a.u.) for maxima ROIs: comparisons between ROIs and genders.

3.1.3 Discussion

In this first sonographic study, the relationship between muscle MEI and ROI size, shape and location was quantitatively investigated in five muscles (biceps brachii, rectus femoris, vastus lateralis, tibialis anterior and medial gastrocnemius) in twenty healthy subjects.

This is the first study showing that muscle echo intensity reliability was function of the ROI size and that MEI was comparable between maxima ROIs and

maxima rectangular ROIs chosen to include as much of the muscle as possible while avoiding bones or surrounding fasciae.

We found that the agreement between different sized ROIs ranged from moderate (ICC: 0.54) to high (ICC: 0.86) and that MEI consistency across the three scans acquired from each muscle ranged from high (ICC: 0.77) to very high (0.91) for maxima rectangular ROIs and maxima ROIs. These results were in line with previous findings and large groups of patients [11], [31]–[35].

The main implication of our findings is that a minimum dimension of the ROI (~10% of the maximum ROI or ~15% of the maximum rectangular ROI) is required for a reliable analysis of the muscle echo intensity. Nevertheless, we also observed a nonlinear relationship between MEI consistency and ROI size as well as a lack of differences in MEI between maxima ROIs and maxima rectangular ROIs. These findings imply that the selection of a ROI including the entire VCSA of a muscle through a manual or an automatic segmentation of the ultrasound image is not required for a reliable and valid estimation of the muscle MEI.

Comparisons between the five muscles and between the two genders showed that:

- the echo intensity was different between different portions of the rectus femoris and tibialis anterior muscles, probably due to the different proportion of fibrous tissue;
- MEI of the biceps brachii and tibialis anterior muscles was higher than that of rectus femoris, vastus lateralis and medial gastrocnemius muscles, probably resulted from different architectural features within the muscles;
- females had higher echo intensity than males, in line with previous observations [36]. The increase of MEI for females could be due to the higher degree of fibrous and adipose tissues content.

In the same article [30] a positive correlation between MEI and subcutaneous tissue layer thickness was found in three (rectus femoris, vastus lateralis and medial

gastrocnemius) out of five investigated muscles, as it was proved in previous works [8], [37], suggesting that muscle adaptations of cellular mechanisms regulating lipid storage play a role in determining the accumulation of fat in the intramuscular depots. On the other hand, it can be hypostatized that MEI does not accurately represent the ROI coarseness (since the distribution shape is lost and the lower/higher values are not very well represented) and/or it is not a valid marker of fibrous and adipose tissue content. Therefore, other descriptors may be required to unravel (in biceps brachii and rectus femoris) and improve (in the other muscles) the correlation between amount of subcutaneous fat and intramuscular fat deposit. In the following section, an advanced quantitative method based on texture analysis is proposed to find fine differences in muscles ultrasound architecture, ROI shape location and gender.

3.2 Quantitative muscle ultrasonography using texture analysis in healthy subjects

3.2.1 Materials and Methods

In the current section built upon Molinari et al. [38], the same dataset of healthy patients, ultrasound procedure and investigated skeletal muscles already described in the previous section were taken into account. In this study, first order texture features based on the histogram of gray levels, Second Order (Haralick features, [39]) and High-Order statistical features (Galloway's features, [40]) and Local Binary Patterns [41], [42] descriptors have been used in the analysis of ultrasound texture of the five previously mentioned skeletal muscles, in female and male subjects.

To conduct the texture analysis, the following ROIs were manually placed in each image as shown in Fig. 3.5. ROIs dimensions were chosen to be the same for each subject. One ROI was chosen in the median portion of the biceps brachii (286 mm²), vastus lateralis (338 mm²) and medial gastrocnemius (338 mm²), whereas two equal sized ROIs were chosen in the rectus femoris (named medialis RF_{med} and lateralis RF_{lat}, 144 mm²) and tibialis anterior (named superior TA_{sup} and inferior TA_{inf}, 68 mm²) to include the largest part of the muscle without the central aponeurosis and the internal fascia. The mean of six measurements (one measurement per ROI for both sides) was used for comparison among muscles and

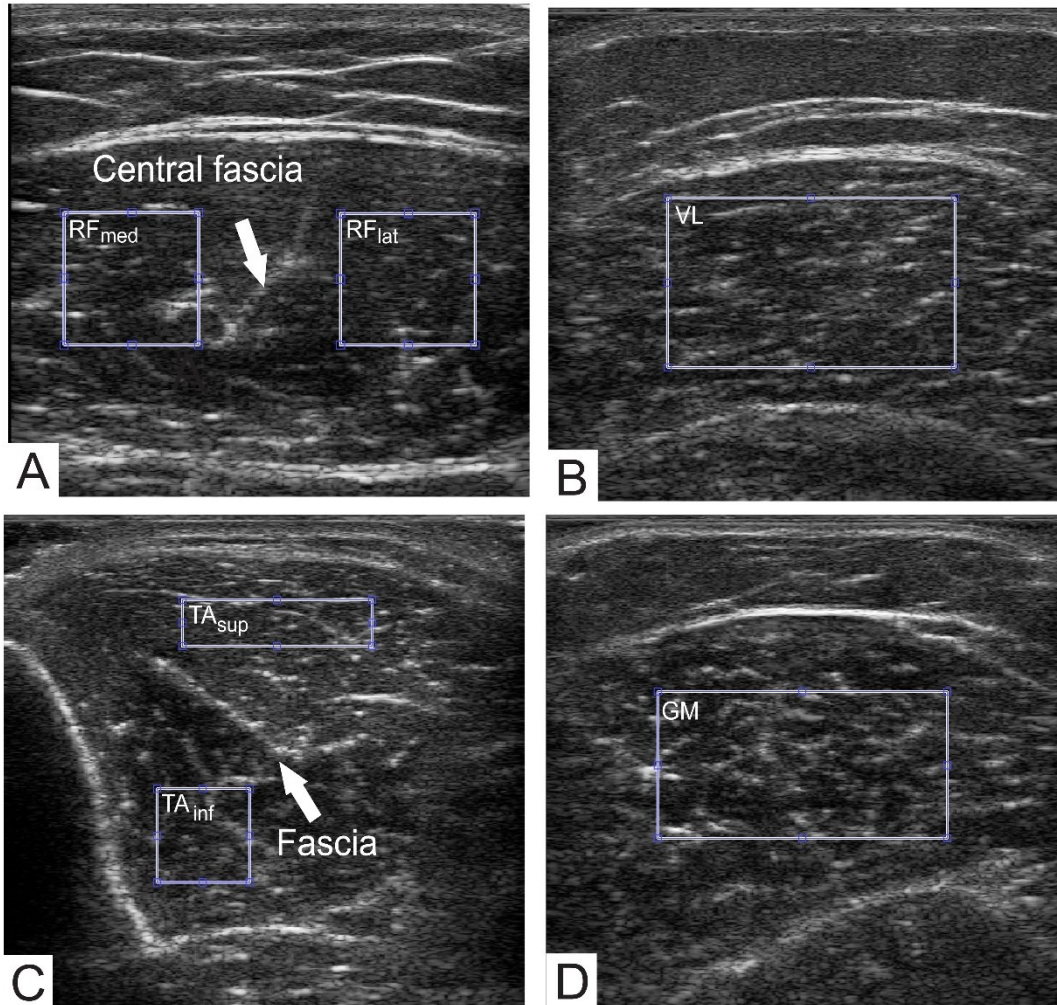


Figure 3. 5: Examples of ROIs positioning for the 4 investigated muscles. Panel A: Rectus femoris, medial ROI (RF_{med}) – lateral ROI (RF_{lat}); panel B: vastus lateralis; panel C: tibialis anterior, superior ROI (TA_{sup}) – inferior ROI (TA_{inf}); panel D: medial gastrocnemius.

between genders. From each ROI, a total of 53 features were extracted: seven First Order Features (IOD, MEI, Standard Deviation, Variance, Skewness, Kurtosis and Energy₁) six Haralick features repeated along the four principal directions (Symmetry, Contrast, Homogeneity, Entropy, Energy₂ and Correlation), five Galloway's features repeated along the four principal directions (Short Run Emphasis, Long Run Emphasis, Gray-level Non-Uniformity, Run-length Non Uniformity and Run Percentage) and two Local Binary Pattern parameters (LBP_{Energy} and LBP_{Entropy}). Further details about the implementation of these texture parameters can be found in the APPENDIX C. Considering four muscles and two sides, a total of 742 features were extracted for each subject.

Since the Shapiro-Wilk test for normal distributed variables failed, Mann-Whitney U test and Kruskal-Wallis ANOVA (followed by the Dunn's post hoc test) were used to compare features' values among the different muscles. The equality of the means among groups was tested conducting a Multivariate Analysis of the Variance (MANOVA). We tested the texture feature values against gender and against the muscle type. Collinear variables were removed by computing the Wilks' lambda to avoid singularities in the observation matrix (further details of the statistical analysis can be retrieve in [38]).

The optimal lambda value for our data set was found to be 0.35, since higher values lead to insufficient removal of collinear variables, whereas lower values discarded an excessive number of variables [43]. The number of groups the data belong can be obtain from the MANOVA's dimension increased of 1. Linear regression in the classification of subjects according to gender or muscle type was performed on the most significant features.

3.2.2 Results

The MANOVA analysis was not significant when the side dominance was the dependent variable, since dominant side texture features were correlated to the non-

dominant side ($p < 0.001$). Hence, variables of the two side were averaged and a total number of 371 features for each subject were considered.

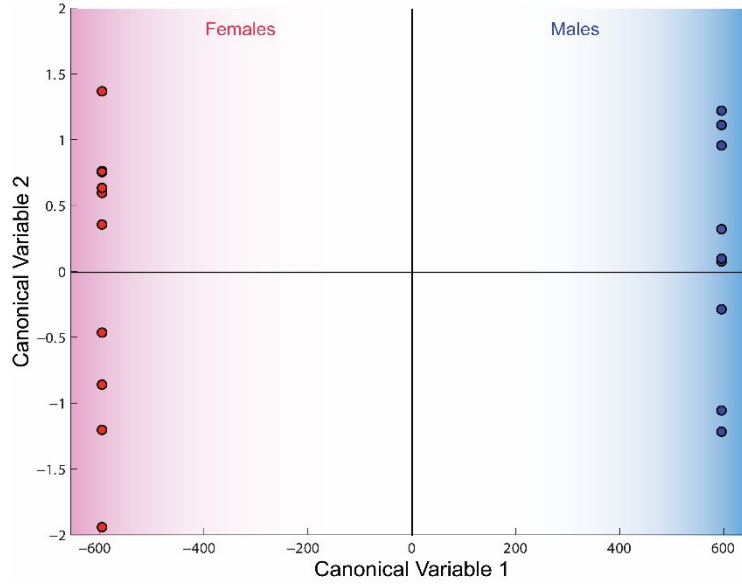


Figure 3. 6: Representation of the patients in the plane of the first two canonical variables obtained by MANOVA. Texture features showed a clear separation of the patients based on the gender.

When the gender was considered as a dependent variable, 38 features were left after the collinear variable removal. The MANOVA dimension was equal to 1 ($p < 0.001$), implying that, in the canonical variables hyperplane, the first canonical variable (CV1) is sufficient to separate the dataset in 2 groups according to gender, as shown in Fig. 3.6 (blue circles are males, red circle are females). The left column of Table 3.3 reports the 10 most discriminant image features between the two genders. First order and Galloway features were not significant ($p > 0.2$). Haralick features (Energy₂, Entropy and Correlation), LBP Energy and Entropy were significantly higher (Haralick Energy₂, $p < 0.01$) and lower (all other features, $p < 0.001$) in men compared with women (data reported on [38]). By using those 10 most discriminant features, we performed a classification of the patients based on the linear regression. All the patients were correctly classified, with sensitivity and specificity of 100% and an Area Under the Receiver Operating Curve (AUROC) equal to 1.

The MANOVA statistics was repeated, keeping 43 features after removing the collinear variables, considering the muscle as a dependent variable. The MANOVA dimension was equal to 6 ($p < 0.02$), hence samples can be separated in 7 distinct groups and are represented in Fig. 3.7 in a plot showing CV1 vs. CV2 (panel A) and CV1 vs. CV3 planes (panel B). The second column of Table 3.3 shows the first

Most discriminant features for gender	Most discriminant features for muscle type
Haralick energy ($\theta = 0^\circ, 45^\circ, 90^\circ, 135^\circ$)	GLNU ($\theta = 0^\circ, 45^\circ, 90^\circ$)
Haralick entropy ($\theta = 90^\circ, 135^\circ$)	Haralick entropy ($\theta = 135^\circ$)
LBP _{energy}	LBP _{entropy}
Haralick correlation ($\theta = 45^\circ, 90^\circ$)	RLNU ($\theta = 135^\circ$)
LBP _{entropy}	Haralick symmetry ($\theta = 90^\circ$)
	RP ($\theta = 90^\circ$)
	SRE ($\theta = 0^\circ, 90^\circ$)

Table 3. 3 Texture features most discriminant between the two genders and among the five muscles in the MANOVA analysis; features listed in descending weight of the first canonical variable.

10 most significant discriminant features. Galloway's features (Gray-level Non-Uniformity, Run Length Non-Uniformity, Run Percentage, Short Run Emphasis), the Haralick's parameters (Entropy and Symmetry) and the LBP_{entropy} are the most important. No significant difference in the texture features was observed between the different ROIs of rectus femoris and tibialis anterior for all comparison ($p > 0.05$). Galloway features (Gray-level Non-Uniformity and Run Length Non-Uniformity) and the Haralick Entropy resulted higher ($p < 0.05$ for all comparisons) in biceps brachii, medial gastrocnemius and vastus lateralis muscles compared with rectus femoris and tibialis anterior muscles. The performance in classifying different muscles using the linear regression showed that the average sensitivity was equal to $76.4 \pm 21.9\%$, the specificity to $97.7 \pm 1.9\%$, and the AUROC to 0.976 ± 0.026 . The two ROIs of the tibialis anterior were perfectly classified (AUROC = 1), and the worst performance was obtained in classifying the rectus femoris (AUROC = 0.936).

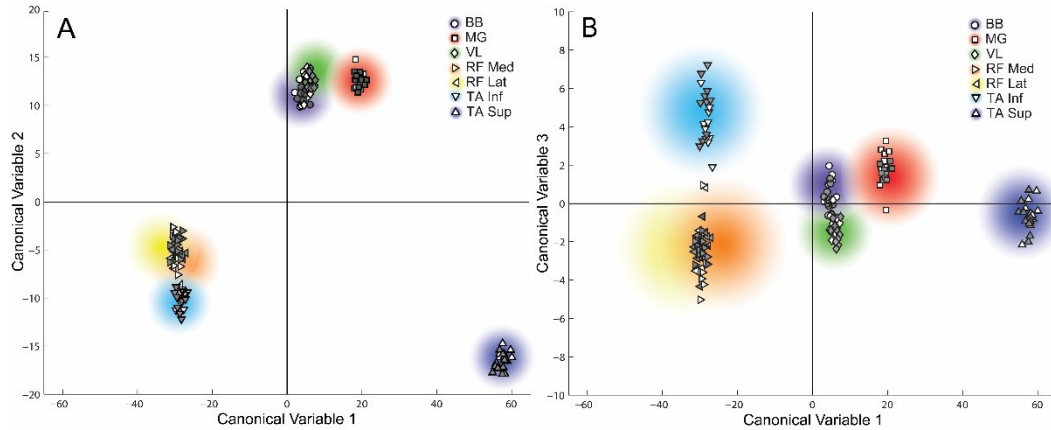


Figure 3. 7: Representation of the patients (A) in the plane of CV1 and CV2, and (B) in the plane of the CV1 and CV3 obtained by MANOVA. Different symbols and colors are used for the different muscles. The full symbols represent the males, the empty symbols the females. BB = biceps brachii; MG = medial gastrocnemius; VL = vastus lateralis; RF = rectus femoris; TA = tibialis anterior.

A further comparison between higher order features (Galloway's and Haralick's features) and first order descriptors was made conducting MANOVA analysis and the classification 7 first-order parameters. From our analysis, when gender is considered the independent variable, the males and females are still separated in the hyperplane of canonical variables but not that evidently as using also high order descriptors. The classification performance was excellent (100% sensitivity and specificity and AUROC of 1), suggesting that Haralick and LBP features did not improve the description of patients on the basis of gender. In the same way, Conducting the MANOVA when the muscle type is the independent variable and using the seven first-order descriptors led to an unclear separation among muscles; even if the dimension of the MANOVA was equal to 6 ($p < 0.05$) the classification performance was significantly lower compared to the complete high-order set of features (average sensitivity of $46.4 \pm 32.3\%$, the specificity of $97.3 \pm 1.92\%$ and AUROC of 0.907 ± 0.081).

3.2.2 Discussion

In this section, quantitative ultrasonography was performed in five muscles (biceps brachii, rectus femoris, vastus lateralis, tibialis anterior, medial gastrocnemius) of 20 healthy patients to assess the characterization performance of higher-order texture descriptors in the differentiation between genders and among muscles.

This work shows that first-order descriptors, Haralick features (Energy₂, Entropy and correlation measured along different angles), LBP_{energy} and LBP_{entropy} were highly linked to the gender, whereas Haralick Entropy and Symmetry, Galloway texture descriptors and LBP_{Entropy} were useful in the differentiation of muscles. It can be noticed that the texture descriptors considered alone do not have a very high discriminatory power.

The main findings of the present study are listed in the following:

- First-order and texture descriptors are comparable to the dominant and non-dominant side of each muscle (confirming the reliability of MEI, reported in [30]).
- First-order features help to distinguish genders.
- Galloway features quantify the coarseness of an image along a given direction and enable to distinguish different types of muscles.
- Haralick and LBP features (in particular, Haralick Entropy and LBP_{Entropy}) quantify the overall (Haralick Entropy) and local (LBP entropy) image homogeneity and distinguish both gender and muscle types.

The first and second findings are confirmed by previous publications [6], [30], in particular, women MEI resulted to be higher than in men. Therefore, the original contribution of this work is the observation that image homogeneity is lower in women compared with men (quantified by Haralick and LBP features) and

directional coarseness (quantified by Galloway features) enables the differentiation of skeletal muscles. Difference in texture parameters are probably related to different portion of fibrous tissue and/or from different architectural features of the fascicles.

The relationship between textural features and adipose and fibrous tissue content and distribution still need to be investigated in the detection of differences between healthy and pathological muscles; combination of different texture features could in the future in the prediction, diagnosis, monitoring and prognosis of myopathic disorders. A preliminary study regarding the possible detection of muscles texture disruption is proposed in the following section.

3.3 Quantitative muscle ultrasonography using texture analysis in healthy subjects and pathological patients

In the present section, a further study on ultrasound muscle texture analysis is proposed. The conclusive aim of this work is to provide a set of preliminary results in the comparison between healthy subjects and patients with endocrine disorders and myopathy (Acromegaly, GHD, Cushing's syndrome, Obesity, Diabetes, Gender Dysphoria patients under hormones therapy), to assess the texture analysis capability in the distinction of healthy and pathological muscles, coupled with the automatic VCSA extraction provided by the TRAMA algorithm and described in Chapter 2. Compared to the previous study, in the current work the VCSA texture of the four previously considered muscles has been extracted, without separating the compartments of rectus femoris and tibialis anterior muscles. With this study, we want to find out if the VCSA texture can, without any further processing on areas, differentiate between healthy and pathological bicompartamental muscles.

3.3.1 Materials and Methods

In this study, the same control subjects and pathological patients already presented in Chapter 2 were considered; four skeletal-muscles were investigated on the dominant side during the ultrasound session: rectus femoris (29 controls, 21 patients, 21 females, 29 males), vastus lateralis (36 controls, 14 patients, 21 females, 29 males), tibialis anterior (20 controls, 30 patients, 28 females, 22 males), and medial gastrocnemius (29 controls, 21 patients, 24 females, 26 males). One scan of each muscle was taken in the transversal plan, and a total of 200 images

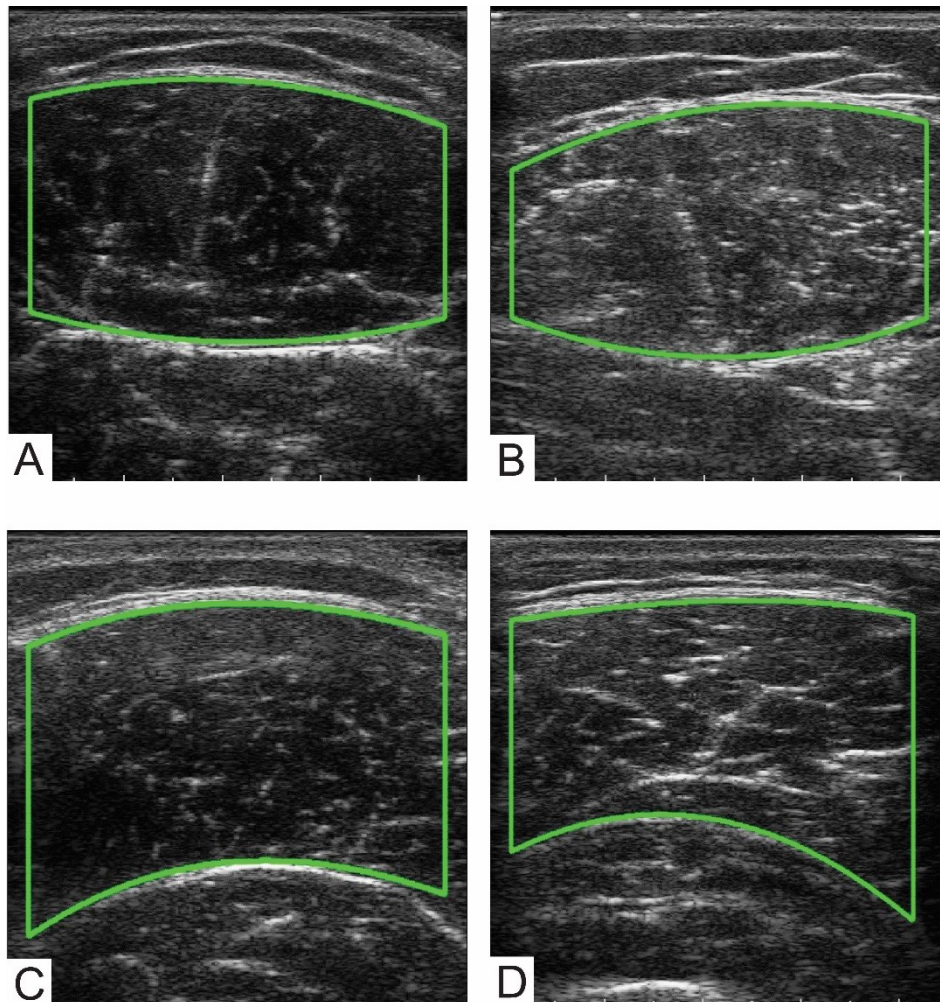


Figure 3. 8: Examples of automatic VCSA performed by TRAMA algorithm in rectus femoris (panels A-B), vastus lateralis (panels C-D), for healthy (panels A-C) and endocrine pathological patients (panels B-D).

were acquired and the automatic VCSA provided by the TRAMA algorithm was extracted as shown in Fig. 3.8 for both healthy and pathological subjects. Following the same procedure reported in the previous section, a total of 53 texture parameters were extracted from each VCSA: seven First Order Features (IOD, MEI, Standard Deviation, Variance, Skewness, Kurtosis and Energy₁) six Haralick features repeated along the four principal directions (Symmetry, Contrast, Homogeneity, Entropy, Energy₂ and Correlation), five Galloway's features repeated along the four principal directions (Short Run Emphasis, Long Run Emphasis, Gray-level non uniformity, Run-length Non-Uniformity and Run Percentage) and two Local Binary Pattern parameters (Energy and Entropy). Compared to the previous study [38], VCSA were not divided in the corresponding superior and inferior tibialis anterior ROIs and medial and lateral rectus femoris ROIs, respectively.

Since the previous work [38] demonstrated the ability of texture analysis in the differentiation of muscles according to the gender and type, two studies were conducted on the texture features capability in the distinction of pathological muscles from healthy ones: considering, as an dependent variable, the presence of the myopathy, we firstly tested the difference between healthy vs pathological females and healthy vs pathological males; subsequently, we tested the difference between healthy vs pathological subjects for each muscle.

Non-parametric Mann-Whitney U tests were used to compare paired features' values. As before, the equality of the means among groups was tested conducting a Multivariate Analysis of the Variance (MANOVA) and collinear variables were removed by computing the Wilks' lambda to avoid singularities in the observation matrices.

The optimal lambda value for our data set was found to be 0.56 for the comparisons between healthy and pathological patients according the gender and 0.14 according to the muscle type, since higher values lead to insufficient removal of collinear variables, whereas lower values discarded an excessive number of variables. The number of groups the data belong can be obtain from the

MANOVA's dimension increased of 1. Linear regression in the classification of subjects according to gender or muscle type was performed on the most significant features.

3.3.2 Results

When the presence of myopathy was considered as a dependent variable and pooled data for the four muscles were considered, 25 features were left after the collinear variable removal for both the females and males groups. The MANOVA

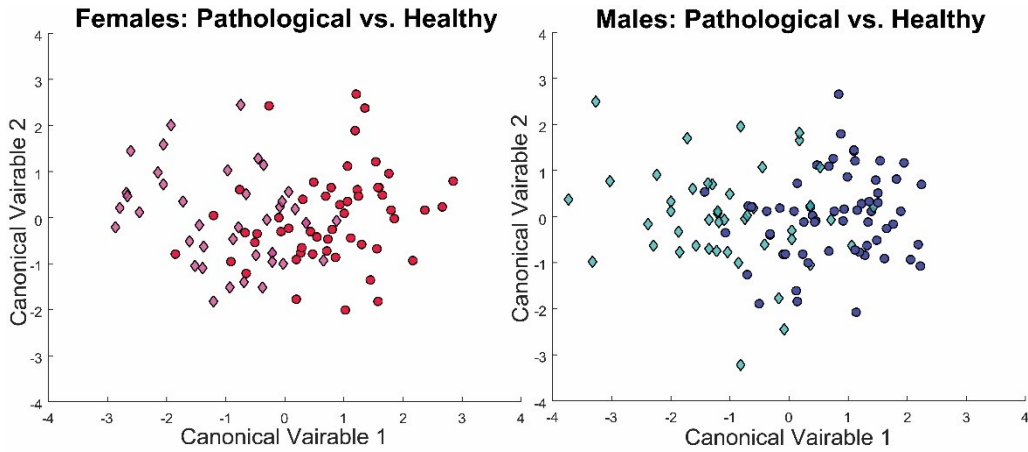


Figure 3. 9: Representation of the controls and pathological patients, for female and male subjects, in the plane of the first two canonical variables (CV1 and CV2) obtained by MANOVA. The features do not allow for a clean-cut separation between the two groups.

dimension was equal to 1 ($p < 0.05$ for the females group, $p < 0.01$ for the males group), implying that, in the canonical variables hyperplane, the first canonical variable (CV1) is sufficient to group the two datasets in healthy and pathological subjects, as shown in Figure 3.9 (diamonds markers are pathological, circles are healthy). Table 3.4 reports the 10 most discriminant image features for the two genders in the distinction between healthy and pathological patients.

No First order variables were reported as significant for the comparisons, Haralick descriptors and Galloways features were the most discriminant. Common features for both genders are 0°Energy and Short Run Emphasis 0° (for both gender

significantly higher in patients group) and 0° Homogeneity (for both genders significantly higher in control group). Galloway's Run Percentage in all directions are also significant higher in both patients' groups, suggesting that texture changes in myopathies may occur along preferential directions for both female and male subjects. Haralick Correlation, along different directions, is significative different for both genders (90° higher and 45° lower for females, 0° higher and 135° lower for males). Nevertheless, the MANOVA classification performance was poor for the females group (sensitivity 44,3%, the specificity of 53.2% and AUROC = 0.40) and males group (sensitivity 43,2%, the specificity of 39.5% and AUROC = 0.41).

Taking as dependent variable the presence of myopathy, a further set of tests was conducted with males and females pooled data, for each muscle separately.

Most discriminant features for females group	Most discriminant features for males group
Haralick Energy ($\theta = 0^\circ$)	
RP ($\theta = 0^\circ, 45^\circ, 90^\circ, 135^\circ$)	
SRE ($\theta = 0^\circ$)	Haralick Homogeneity ($\theta = 0^\circ, 45^\circ$)
LBP _{entropy}	SRE ($\theta = 0^\circ$)
Haralick Correlation ($\theta = 45^\circ, 90^\circ$)	Haralick Symmetry ($\theta = 90^\circ$)
Haralick Homogeneity ($\theta = 0^\circ$)	Haralick Correlation ($\theta = 0^\circ, 135^\circ$)

Table 3. 4: Image features that are the most discriminant between healthy and pathological subjects for the two genders in the MANOVA analysis.

To perform the MANOVA, after the collinear variables removal, 43, 36, 20 and 29 features were left for rectus femoris, vastus lateralis, tibialis anterior and medial gastrocnemius respectively. The dimension of the MANOVA was equal to 1 for all muscle types ($p < 0.05$). Fig. 3.10 shows in four panels the results of the MANOVAs plotted in the canonical variables plane (CV1 vs CV2) for the considered muscles. For all the four investigated muscles, MANOVA performance classification was excellent (AUROC = 1). In table 3.5 the first 10 most discriminant features for the four muscles in the separation between controls and patients are presented (p-value threshold fixed at 0.05). The first 4 variables

(Energy 0° , 45° , 90° , 135°) are common for all muscles, indicating that these variables are generally highly discriminant between healthy and pathological muscles. $LBP_{entropy}$ is significantly higher in healthy controls for vastus lateralis, tibialis anterior and medial gastrocnemius; in the same way, LBP_{energy} is significantly higher in healthy control for rectus femoris, vastus lateralis and medial gastrocnemius; these findings suggest that the architectural aspect of healthy muscles can be detected and described by morphological operators. Correlation 0° for vastus lateralis, tibialis anterior and medial gastrocnemius and Correlation 45° for rectus femoris are higher for normal subjects, reflecting the property of healthy muscles of being better organized and with a less chaotic texture, also confirmed by higher values of Homogeneity in different directions (90° , 135° for

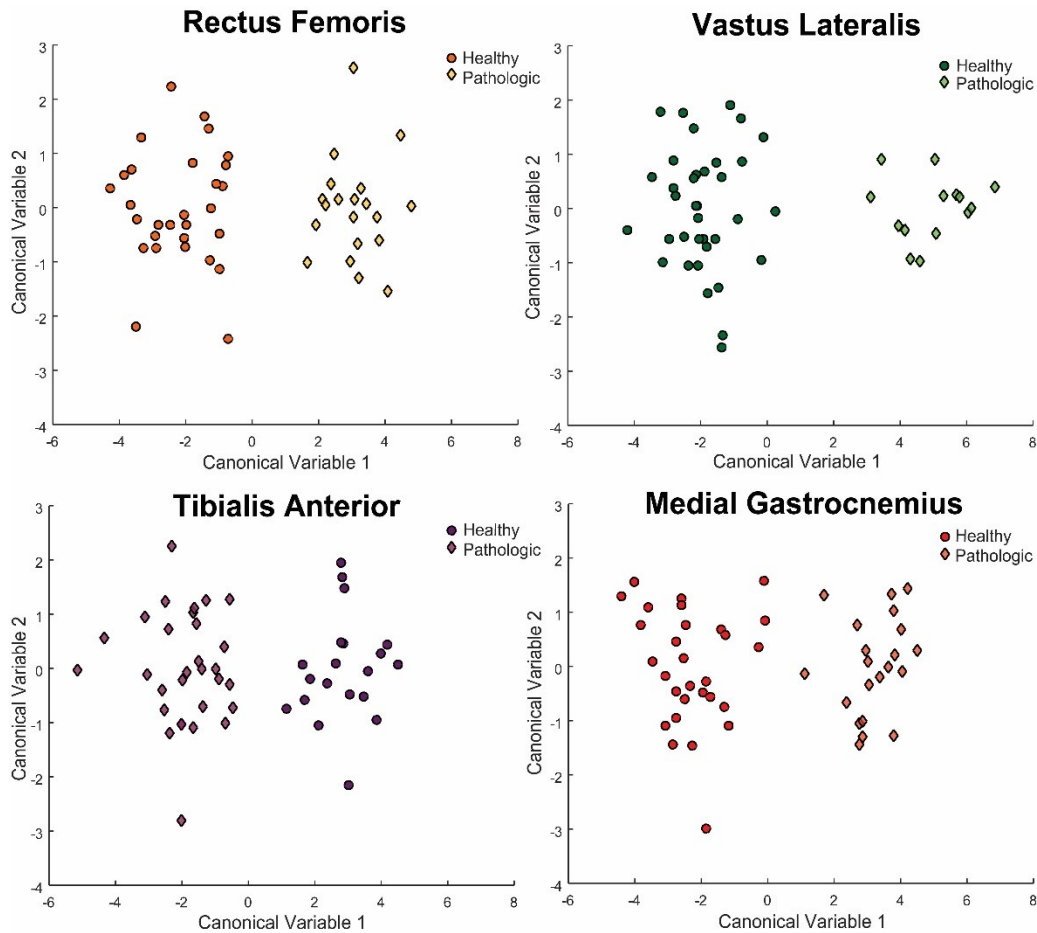


Figure 3.10: Representation of pooled healthy and pathological patients in the hyperplane of the canonical variables obtained by MANOVA. The texture features allowed the clear separation of the two groups for all the four muscles.

rectus femoris, 0° , 90° , 135° for the vastus lateralis and 0° , 45° , 90° for the medial gastrocnemius). Galloway Short Run Emphasis 0° also presents higher values in healthy controls for rectus femoris, vastus lateralis and tibialis anterior, strengthening the hypothesis of higher pattern uniformity. On the other hand, both rectus femoris and tibialis anterior, whose two compartments have not been separated in the analysis, present a discriminant characteristic feature: Long Run Emphasis (45°) for rectus femoris and for tibialis anterior Haralick Entropy (45° , 90°) present higher values in the pathological population.

Most discriminant features for rectus femoris	Most discriminant features for vastus lateralis	Most discriminant features for tibialis anterior	Most discriminant features for medial gastrocnemius
Haralick Energy ($\theta = 0^\circ$, 45° , 90° , 135°)			
LRE ($\theta = 45^\circ$)	LBP _{entropy}		
SRE ($\theta = 0^\circ$)	Haralick Homogeneity ($\theta = 0^\circ$, 90° , 135°)		Haralick Homogeneity ($\theta = 0^\circ$, 45° , 90°)
LBP _{energy}		SRE ($\theta = 0^\circ$)	LBP _{energy}
Haralick Correlation ($\theta = 45^\circ$)	Haralick Correlation ($\theta = 0^\circ$)		
Haralick Homogeneity ($\theta = 90^\circ$, 135°)	Haralick Entropy ($\theta = 45^\circ$, 90°)		

Table 3. 5: Most discriminant features between healthy and pathological patients for all the four muscle in the MANOVA analysis.

From the reported results, a common texture features set for the discrimination between healthy and pathological muscles can be identified: the Haralick Energy parameter, computed along the 0° direction, shows significantly higher values in the control subjects both for genders and muscle type.

3.3.3 Discussion

In the conclusive study on ultrasound skeletal muscle investigation, quantitative texture analysis was performed in five muscles (rectus femoris, vastus lateralis, tibialis anterior, medial gastrocnemius) of 116 subjects and to assess the characterization performance of higher-order texture descriptors in the differentiation between healthy and pathological for genders and among muscles.

This work shows that a subset of texture descriptors can be used in the differentiation between healthy and pathological muscles.

The main findings of the present work are listed in the following:

- First-order descriptors are not significant in the differentiation between healthy and pathological subjects;
- The clouds of healthy and pathological patients cannot be clearly separated in the hyperplane of canonical variables for both females and males;
- Higher-order texture descriptors have higher weight in the classification: in particular, Haralick Energy, Correlation and Homogeneity, Short Run Emphasis, and LBP entropy are common for both gender and muscle type studies;
- Haralick Energy is the most discriminant feature in all the performed classifications;
- Classification of healthy and pathological subjects for bicompartimental muscles, such as rectus femoris and tibialis anterior, is made possible considering a further characteristic parameter (Long Run Emphasis of rectus femoris and Haralick Entropy for tibialis anterior).

Compared to the previous findings [38], this analysis confirms that texture analysis performed on muscle VCSA extraction can be used in the differentiation of healthy and pathological muscles. In particular, this study shows how texture

descriptors can have different weight in the classification procedure; nevertheless, texture descriptors have a small power, if taken as single entities. Some muscles, such as bicompartmental ones, need the extraction of at least one more descriptor compared to mono-compartmental muscles.

In a recent medline of 2017, only three published works have applied texture analysis in skeletal muscle ultrasound diagnostic procedures. Sogawa et al. [44] have demonstrated the ability of MEI in the differentiation between healthy and pathological medial gastrocnemius muscles; moreover, they have demonstrated that high texture descriptors (Haralick and Galloway features) are effective in the distinction between neurogenic and myogenic groups. The present study partly confirms these findings, showing that a clear separation between healthy and pathological medial gastrocnemius is achieved extracting Haralick and LBP features.

In another work, Martinez-Payà et al. [45], first order descriptors and Haralick features combined with muscle architectural parameters were used and considered as biomarkers in the classification of amyotrophic lateral sclerosis in biceps brachialis, forearm flexor, quadriceps femoris, and tibialis anterior muscle groups.

Lastly, Matta et al. [46] used Haralick descriptors in the assessment of biceps brachii muscle damage induced by eccentric-exercise, finding that Haralick Correlation significantly increased few hours after training. Even if muscle damage is related to an inflammatory process and has been proven to increase the muscle ultrasound MEI, in the present study healthy patients have higher values of Haralick correlation compared to pathological subjects. These findings may suggest that correlation itself can highlight differences between inflammation and muscle disorders and should be considered together with a larger number of descriptors to provide a better classification performance.

3.4 Conclusions

In this Chapter, a complete quantitative characterization in skeletal muscles ultrasonography is proposed, starting from the MEI state-of-the-art muscle quality to the application of a fully automated strategy in the assessment of healthy and pathological muscles by high-dimensional agnostic texture descriptors.

The presented study shows how automated segmentation coupled with texture analysis can provide information “beyond the surface” of an image, and how image data can improve the muscle disorders diagnosis; this approach could be find application in automatic diagnosis on ultrasound scanners.

In the future, semantic and agnostic attributes on ultrasound skeletal muscles could be stored in databases and mined with dedicated bioinformatic algorithms to provide prognostic and predictive results for personalized medicine.

3.5 References

- [1] S. Pillen, I. M. P. Arts, and M. J. Zwarts, “Muscle ultrasound in neuromuscular disorders,” *Muscle and Nerve*, pp. 679–693, 2008.
- [2] N. Maurits, A. Bollen, A. Windhausen, A. De Jager, and J. Van der Hoeven, “Muscle Ultrasound Analysis: normal value and differentiation between myopathies and neuropathies,” *Ultrasound Med. Biol.*, vol. 29, pp. 215–225, 2003.
- [3] R. R. Scholten, S. Pillen, and A. Verrips, “Quantitative ultrasonography of skeletal muscles in children: normale value,” vol. 27, pp. 693–698, 2003.
- [4] F. O. Walker, M. S. Cartwright, E. R. Wiesler, and J. Caress, “Ultrasound of nerve and muscle,” vol. 115, pp. 495–507, 2004.
- [5] S. Pillen, I. Arts, and M. Zwarts, “Muscle Ultrasound in neuromuscular disorders,” *Muscle and Nerve*, vol. 37, pp. 679–693, 2008.
- [6] I. Arts, S. Pillen, H. Schelhaas, S. Overeem, and M. Zwarts, “Normal values for quantitative muscle ultrasonography in adults,” *Muscle and Nerve*, vol. 41, pp. 32–41, 2010.
- [7] I. Arts, H. Schelhaas, K. Verrijp, M. Zwarts, S. Overeem, J. Van der Laak, M. Lammens, and S. Pillen, “Intramuscular fibrous tissue determines muscle echo intensity in amyotrophic lateral sclerosis,” *Muscle and Nerve*, vol. 45, pp. 449–450, 2012.
- [8] I. Miljkovic and J. Zmuda, “Epidemiology of myosteatorsis,” *Curr Opin Clin Nutr Metab Care*, vol. 13, pp. 260–264, 2010.
- [9] M. Hamrick, M. McGee-Lawrance, and D. Frchette, “Fatty infiltration of Skeletal Muscle: Mechanisms and Comparisons with Bone Marrow Adiposity,” *Front. Endocrinol. (Lausanne)*, vol. 7, pp. 1–7, 2016.

- [10] I. Miljkovic, A. Kuipers, R. Cvejkus, C. Bunker, A. Patrick, C. Gordon, and J. Zmuda, "Myosteatosis increases with aging and is associated with incident diabetes in African ancestry men," *Obes. (Silver Spring)*, vol. 24, pp. 476–482, 2016.
- [11] S. Pillen, M. Van Keimpema, R. Nievelstein, A. Verrips, W. van Kruijsbergen-Raijmann, and M. Zwarts, "Skeletal muscle ultrasonography: visual versus quantitative evaluation.," *Ultrasound Med. Biol.*, vol. 32, pp. 1315–1321, 2006.
- [12] S. Pillen, J. Van Dijk, G. Weijers, W. Raijmann, C. De Korte, and M. Zwarts, "Quantitative gray-scale analysis in skeletal muscle ultrasound: a comparison study of two ultrasound devices," *Muscle and Nerve*, vol. 39, pp. 781–786, 2009.
- [13] S. Pillen, R. Tak, M. Zwarts, M. Lammens, K. Verrijp, I. Arts, J. van der Laak, P. Hoogerbrugge, B. van Engelen, and A. Verrips, "Skeletal muscle ultrasound: correlation between fibrous tissue and echo intensity.," *Ultrasound Med. Biol.*, vol. 35, pp. 443–446, 2009.
- [14] C. Zaidman, M. Holland, C. Anderson, and A. Pestronk, "Calibrated quantitative ultrasound imaging of skeletal muscle using backscatter analysis," *Muscle and Nerve*, vol. 38, pp. 893–898, 2008.
- [15] U. Acharya, M. Mookiah, V. Sree, R. Yanti, R. Martis, L. Saba, F. Molinari, S. Guerriero, and J. Suri, "Evolutionary algorithm-based classifier parameter tuning for automatic ovarian cancer tissue characterization and classification.," *Ultraschall der Medizin*, vol. 35, pp. 237–245, 2014.
- [16] U. R. Acharya, G. Swapna, S. V Sree, F. Molinari, S. Gupta, R. H. Bardales, A. Witkowska, and J. S. Suri, "A review on ultrasound-based thyroid cancer tissue characterization and automated classification.," *Technol. Cancer Res. Treat.*, vol. 13, pp. 289–301, 2014.
- [17] U. Acharya, O. Faust, S. Sree, F. Molinari, and J. Suri, "ThyroScreen system: high resolution ultrasound thyroid image characterization into benign and malignant classes using novel combination of texture and discrete wavelet transform.," *Comput. Methods Programs Biomed.*, vol. 107, pp. 233–241, 2012.
- [18] U. R. Acharya, S. V. Sree, M. M. R. Krishnan, L. Saba, F. Molinari, S. Guerriero, and J. S. Suri, "Ovarian Tumor Characterization using 3D Ultrasound," *Technol. Cancer Res. Treat.*, vol. 11, pp. 543–552, 2012.
- [19] R. Acharya, S. Sree, M. Mookiah, F. Molinari, R. Garberoglio, and J. S. Suri, "Non-invasive automated 3D thyroid lesion classification in ultrasound: A class of ThyroScan systems," *Ultrasonics*, vol. 52, pp. 508–520, 2012.
- [20] N. Kim, V. Amin, D. Wilson, G. Rouse, and S. Udpa, "Ultrasound image texture analysis for characterizing intramuscular fat content of live beef cattle.," *Ultrason. Imaging*, vol. 20, pp. 191–205, 1998.
- [21] R. U. Acharya, O. Faust, A. P. C. Alvin, S. V. Sree, F. Molinari, L. Saba, A. Nicolaides, and J. S. Suri, "Symptomatic vs. Asymptomatic Plaque Classification in Carotid Ultrasound," *J. Med. Syst.*, vol. 36, pp. 1861–1871, 2012.
- [22] L. Niu, M. Qian, W. Yang, L. Meng, Y. Xiao, K. K. L. Wong, D. Abbott, X. Liu, and H. Zheng, "Surface roughness detection of arteries via texture analysis of ultrasound images for early diagnosis of atherosclerosis.," *PLoS One*, vol. 8, p. e76880, 2013.
- [23] A. P. Singh and B. Singh, *Texture Features Extraction in Mammograms Using Non-Shannon Entropies. Machine learning and systems engineering*. Springer, Dordrecht, 2010.
- [24] U. R. Acharya, S. V. Sree, L. Saba, F. Molinari, S. Guerriero, and J. S. Suri, "Ovarian tumor characterization and classification using ultrasound-a new online paradigm.," *J. Digit. Imaging*, vol. 26, pp. 544–553, 2013.
- [25] U. Acharya, S. Sree, M. Krishnan, F. Molinari, W. Zieleznik, R. Bardales, A. Witkowska, and J. Suri, "Computer-aided diagnostic system for detection of Hashimoto thyroiditis on ultrasound images from a Polish population.," *J. Ultrasound Med.*, vol. 33, pp. 245–253, 2014.
- [26] U. Acharya, O. Faust, F. Molinari, S. Sree, S. Junnarkar, and V. Sudarshan, "Ultrasound-based tissue characterization and classification of fatty liver disease: A screening and diagnostic paradigm.,"

- Knowledge-Based Syst., vol. 75, pp. 66–77, 2015.
- [27] S. Gao, Y. Peng, H. Guo, W. Liu, T. Gao, Y. Xu, and X. Tang, “Texture analysis and classification of ultrasound liver images,” *Biomed. Mater. Eng.*, vol. 24, pp. 1209–1216, 2014.
 - [28] N. Maurits, E. Beenakker, D. Van Schalk, J. Fock, and J. Van der Hoeven, “Muscle ultrasound in children: normal values and application to neuromuscular disorders,” *Ultrasound Med. Biol.*, vol. 30, pp. 1017–1027, 2004.
 - [29] H.-J. Gdynia, H.-P. Müller, A. C. Ludolph, H. Köninger, and R. Huber, “Quantitative muscle ultrasound in neuromuscular disorders using the parameters ‘intensity’, ‘entropy’, and ‘fractal dimension’,,” *Eur. J. Neurol.*, vol. 16, pp. 1151–1158, 2009.
 - [30] C. Caresio, F. Molinari, G. Emanuel, and M. A. Minetto, “Muscle echo intensity: reliability and conditioning factors,” *Clin. Physiol. Funct. Imaging*, vol. 35, pp. 393–403, 2015.
 - [31] R. Radaelli, M. Bottaro, E. N. Wilhelm, D. R. Wagner, and R. S. Pinto, “Time course of strength and echo intensity recovery after resistance exercise in women,” *J. strength Cond. Res.*, vol. 26, pp. 2577–2584, 2012.
 - [32] Y. Fukumoto, T. Ikezoe, H. Tateuchi, R. Tsukagoshi, H. Akiyama, K. So, Y. Kuroda, T. Yoneyama, and N. Ichihashi, “Muscle mass and composition of the hip, thigh and abdominal muscles in women with and without hip osteoarthritis,” *Ultrasound Med. Biol.*, vol. 38, pp. 1540–1545, 2012.
 - [33] Y. Fukumoto, T. Ikezoe, Y. Yamada, R. Tsukagoshi, M. Nakamura, N. Mori, M. Kimura, and N. Ichihashi, “Skeletal muscle quality assessed from echo intensity is associated with muscle strength of middle-aged and elderly persons,” *Eur. J. Appl. Physiol.*, vol. 112, pp. 1519–1525, 2012.
 - [34] J. G. Rosenberg, E. D. Ryan, E. J. Sobolewski, M. J. Scharville, B. J. Thompson, and G. E. King, “Reliability of panoramic ultrasound imaging to simultaneously examine muscle size and quality of the medial gastrocnemius,” *Muscle and Nerve*, vol. 49, pp. 736–740, 2014.
 - [35] M. Chen, W.-P. Wang, W.-R. Jia, L. Tang, Y. Wang, W.-W. Zhan, and X.-C. Fei, “Three-dimensional contrast-enhanced sonography in the assessment of breast tumor angiogenesis correlation with microvessel density and vascular endothelial growth factor expression,” *J. Ultrasound Med.*, vol. 33, pp. 835–846, 2014.
 - [36] I. M. P. Arts, S. Pillen, H. J. Schelhaas, S. Overeem, and M. J. Zwarts, “Normal values for quantitative muscle ultrasonography in adults,” *Muscle and Nerve*, vol. 41, pp. 32–41, 2010.
 - [37] J. Nijboer-Oosterveld, N. Van Alfen, and S. Pillen, “New normal values for quantitative muscle ultrasound: obesity increases muscle echo intensity,” *Muscle and Nerve*, vol. 43, pp. 142–143, 2011.
 - [38] F. Molinari, C. Caresio, R. U. Acharya, M. R. K. Mookiah, and M. A. Minetto, “Advances in quantitative muscle ultrasonography using texture analysis of ultrasounding images,” *Ultrasound Med. Biol.*, vol. 41, pp. 2520–2532, 2015.
 - [39] R. M. Haralick, K. Shanmugam, and I. Dinstein, “Textural Features for Image Classification,” *IEEE Trans. Syst. Man. Cybern.*, vol. SMC-3, pp. 610–621, 1973.
 - [40] M. M. Galloway, “Texture analysis using gray level run lengths,” *Comput. Graph. Image Process.*, vol. 4, pp. 172–179, 1975.
 - [41] T. Ojala, M. Pietikainen, and T. Maenpaa, “Multiresolution gray-scale and rotation invariant texture classification with local binary patterns,” *IEEE Trans. Pattern Anal. Mach. Intell.*, vol. 24, pp. 971–987, 2002.
 - [42] T. Ojala, M. Pietikäinen, and D. Harwood, “A comparative study of texture measures with classification based on featured distributions,” *Pattern Recognit.*, vol. 29, pp. 51–59, 1996.
 - [43] M. C. Costanza and A. A. Afifi, “Comparison of Stopping Rules in Forward ‘Stepwise’ Regression,” *J. Am. Stat. Assoc.*, vol. 74, no. 368, pp. 777–785, 1979.
 - [44] K. Sogawa, H. Nodera, N. Takamatsu, A. Mori, H. Yamazaki, Y. Shimatani, Y. Izumi, and R. Kaji, “Neurogenic and Myogenic Diseases: Quantitative Texture Analysis of Muscle US Data for Differentiation,” *Radiology*, vol. 283, pp. 492–498, 2017.

- [45] J. J. Martínez-Payá, J. Ríos-Díaz, M. E. del Baño-Aledo, J. I. Tembl-Ferrairó, J. F. Vazquez-Costa, and F. Medina-Mirapeix, "Quantitative Muscle Ultrasonography Using Textural Analysis in Amyotrophic Lateral Sclerosis," *Ultrason. Imaging*, 2017.
- [46] T. T. da Matta, W. C. de A. Pereira, R. Radaelli, R. S. Pinto, and L. F. de Oliveira, "Texture analysis of ultrasound images is a sensitive method to follow-up muscle damage induced by eccentric exercise," *Clin. Physiol. Funct. Imaging*, 2017.

Chapter 4

Multimodal 3-D ultrasound quantitative characterization of thyroid tumors vasculature

This chapter has been built upon:

C. Caresio, , M. Caballo, M. Deandrea, R. Garberoglio, R. Mormile, R. Rossetto, P. Limone, F. Molinari, **Optimized quantification of thyroid nodular vascularization from 3-D contrast enhanced ultrasound images.**, *The 22^o European Symposium on Ultrasound Contrast Imaging*, January 19-20th, 2017, Rotterdam, The Netherlands.

4.1 Introduction

Tumor vasculature plays a fundamental role in cancer growth and evolution [1]–[2]. At any evolution stage, cancers are highly oxygen and nutrients demanding [3]; consequently, they produce a considerable quantity of angiogenic growth factors (i.e. Ang-1 and VEGF) that stimulate neo-vessels formation, which rapidly branch out from the existing vasculature through a process called angiogenesis [4]. Compared to healthy tissues, tumor angiogenesis usually incurs excessively dilated, malformed, and chaotic blood vessels [5]. In particular, malignant tumors present a dense, tortuous and usually incomplete vascular network [6], which needs to be better understood in the clinical practice for the assessment and characterization of tumor malignancy and for monitoring vascular abnormalities.

Several imaging techniques are currently used within the clinical practice in the assessment of tumor vascularity, such as contrast-enhancement computed tomography (CT) [7] and magnetic resonance imaging (MRI) [8]. Both techniques present excellent spatial and contrast resolution and are specifically optimized in the detection of blood vessels morphology, but they present a few downsides, such as the CT ionizing radiations and the MRI high cost and highly toxic contrast agents [9], [10].

In recent times, Power Doppler UltraSound (PDUS) and Contrast-Enhancement UltraSound (CEUS) have been used in the investigation of cancer vasculature development, taking advantage of the ultrasound imaging safety and convenience [11], [12].

CEUS imaging implies the use of Ultrasound Contrast Agents (UCAs), able to increase contrast within the vessels compared to the parenchymal surrounding tissue. Given the size of the bubbles (smaller than red blood cells), this technique can depict details with an excellent spatial resolution (10 μm). On the other hand, the Doppler imaging, even though with lower resolution (200-300 μm), encodes the strength of the Doppler signal which directly subjects to the amount of blood flowing in the tumor vascular network.

In the past years, previous works have already been proposed in the quantification of tumor vasculature. Hoyt et al. developed a volumetric strategy for real-time monitoring and characterization of tumor blood flow using CEUS imaging [13]. They found that CEUS imaging is a promising modality for monitoring changes in tissue perfusion and may prove clinical feasibility for detecting and monitoring the early antitumor effects in response to cancer drug therapy. Gerst et al. performed a study to determine whether preoperative CEUS imaging can be used to differentiate benign renal tumors from carcinoma [14]. They found that ultrasound features of gray-scale heterogeneity and perfusion curve parameters can be used in the differentiation carcinoma and non-clear cell renal tumors. Wu et al. [15] quantified the Power Doppler signal on cervical lymphadenopathy and calculated the vascular voxels' density to assess the tumor vascularity. In this study several types of vascular patterns both benign and malignant were recognized, and the main conclusion was that higher values of vascular density may be related to higher malignancy grade. Finally, Huang et al. extracted several quantitative features from 3-D PDUS imaging of breast cancer, demonstrating a correlation between the morphology of blood vessels and tumor malignancy [16]. Moreover, CEUS and PDUS techniques have been both applied in the vascular features extraction and computation of vascularity indices of malignancy [17][18]. However, quantification is often limited to the count of the visible vessels number (VN) or the computation of the Micro Vascular Density (MVD). Since both benign and malignant tumors may present the same values of VN and MVD, these parameters may be insufficient for the accurate differentiation of benign and malignant thyroid tumors. Vascular features quantification can objectively and completely characterize the chaotic pattern the cancerous vasculature, and enables the differentiation between benign and malignant tumors.

Among the tumor formations investigated in clinical practice, thyroid nodules are particularly suitable for ultrasound imaging [19], [20], since thyroid is a superficial organ with no superimposed dense (i.e. highly-attenuating) structures.

Thyroid nodules are abnormal growths of thyroid cells that form a lump within the thyroid gland and are commonly diagnosed in clinical practice (up to 50% of the worldwide population). Even if the number of new thyroid cancers has considerably risen in the last decade, only 5% of thyroid nodules are malignant (incidence: 2.1%, mortality 0.5%, [21]).

Although the great majority of thyroid nodules are benign (noncancerous), a small proportion of thyroid nodules contain thyroid cancer [22]. Differential diagnosis is, therefore, of extreme importance for a correct treatment of the nodule. Conventional ultrasound imaging has a moderate diagnostic accuracy (sensitivity: 68-100%, specificity: 67-94%, [23]) in the differentiation of thyroid nodules, and it must be coupled to fine needle aspiration (FNA) biopsy. However, FNA biopsy is an invasive procedure subjected to inconclusive diagnosis in about 25% of the cases, possibly leading to overtreatment and unneeded surgery.

PDUS imaging and CEUS imaging techniques have a consolidate clinical background in thyroid cancer diagnosis and in functional imaging studies for their spatial and temporal resolution [24]. Both techniques evaluate the specific characteristics of the vascularity associated with thyroid nodules.

In previous works, quantitative 2-D CEUS imaging has been proven to be effective in the assessment of thyroid nodules [17],[25]–[27] ; all the cited methods are based on perfusion curves, enhancement patterns, signal intensity and nodules area measurements. Quantitative 2-D PDUS imaging found application in the detection of malignant lesions by means of the computation of a Doppler Vascular Index [28]. To the best of our knowledge, 3-D CEUS quantitative geometrical analysis of thyroid nodules has only proposed by Molinari et al. [29] and this study represents a further step in the characterization of thyroid lesions, extending the analysis to the 3-D PDUS imaging.

In this work, a volume processing and geometrical features extraction algorithm are described to study the correlation between thyroid tumors vascularity and malignancy; moreover, a performance comparison between 3-D PDUS and 3-D

CEUS techniques in malignancy characterization is proposed. Since both imaging modalities provide images in which the functionality of the tumor is more outstanding rather than the morphological aspect, we adopted a pipeline-steps strategy to transform the original volumes into a set of interconnected single-voxel skeletons. The tumor vasculature is assessed by the automatic extraction of 7 vascular features, partly reported in previous works [16], [29]. Extracted features are the number of vascular trees (NT), number of branching (NB), vascular volume density (VVD), and three tortuosity measures, namely Distance Metric (DM), Inflections Count Metric (ICM) and Sum Of Angles Metric (SOAM). One further parameter, called Spatial Vascular Pattern (SVP) and related to the geometrical location of tumor vessels, has been automatically detected from the vasculature [30]. For each feature, we compared the value extracted from CEUS and PDUS volumes to prove its statistical significance. Finally, the diagnosis using these seven features in classification of benign and malignant tumors was performed using MANOVA. The implemented strategy enables the objective assessment of tumor vasculature, and suggest that the proposed morphological features can have clinical impact in thyroid nodules classification, for both the PDUS and the CEUS techniques.

4.2 Materials and Methods

Subjects and acquisition settings

Twenty patients (3 Males, age 43.0 ± 10.4 , range 31 – 49 years, 17 Females, age 46.0 ± 13.2 , range 31 – 75 years) with a previous diagnosis of solitary solid thyroid nodule were enrolled to participate to the study; 10 patients were recruited from the Division of Endocrinology, Diabetology and Metabolism of the “Città della Salute e della Scienza” Hospital of Torino, Italy, and 10 patients were recruited from the Endocrinology Section of the “Umberto I” Hospital of Torino, Italy. Inclusion criteria were: age ≥ 18 years and maximum diameter of the thyroid

nodules ≤ 4 cm. Exclusion criteria were: multi-nodule goiter, thyroiditis, and other generic inflammatory process. The experimental protocol for this multi-center study was approved by the ethical committee of both hospitals. The patients signed an informed consent before participating in the experiment.

All subjects underwent clinical examination, hormonal profiling, and Fine Needle Aspiration (FNA) biopsy. Longitudinal diameter (LD), anteroposterior diameter (AD) and transversal diameter (TD) were measured by ultrasound B-Mode examination. From the FNA result, ten patients presented benign nodules, and ten had malignant lesions.

The 10 benign nodules (LD: 16.75 ± 4.32 mm, AD: 20.33 ± 4.11 mm, TD: 15.00 ± 5.35 mm) were classified as THY2 (9 single goiter nodules) and THY3a (1 nodules with architectural atypia) according to the cytological criteria [20], [21]. The malignant nodules (LD: 19.50 ± 7.89 mm; AD: 25.67 ± 9.66 mm; TD: 19.50 ± 7.25 mm) were classified as THY3f (4 suspected follicular neoplasms), THY4 (2 suspicious malignant nodules), and THY5 (4 positive malignant nodules). All the subjects with diagnosis of malignancy from FNA underwent surgical treatment. The histopathological report after thyroidectomy confirmed the malignancy for all the ten subjects (7 papillary carcinomas, 2 follicular carcinomas, 1 Hurtle cells carcinoma).

Ultrasound Equipment and Image Acquisition

3-D PDUS and 3-D CEUS scans were performed for all patients during the same experimental session. The 3-D volumes were acquired using a MyLab™ Twice (at the “Città della Salute e della Scienza” Hospital) and a MyLab70 (at the “Umberto I” Hospital) ultrasound devices (Esaote, Genova, Italy), both equipped with the same linear-volumetric array transducer (code BL433) with 4-13 MHz variable frequency. The main feature of this transducer is that the piezoelectric elements are mounted on a moving array which enables 3-D scan of tissues without moving the probe [33], [34]. We used a fixed scanning angle of 50 degrees and a

scanning step variable between 0.24 – 0.30 degrees, which was automatically selected according to the scanning depth. The average frame-rate was equal to 15 frames/s. For all the 3-D acquisitions, the B-Mode gain was set at the 50% and the Time Gain Compensation was kept in a neutral position. The Pulse Repetition Frequency (PRF) at 1 kHz and the wall filter at 4 Hz. To acquire CEUS volumes, 2.4 ml of ultrasound contrast agent (Sonovue, Bracco, Italy) were administrated intravenously and a 3-D volume containing the lesion was acquired after 40 seconds from the injection, to avoid the blooming artefact. The 3-D volumes were transferred offline to an external workstation for subsequent processing.

Vascular segmentation algorithm

Fig. 4.1 sketches the overall processing pipeline of our analysis technique. The entire processing framework was developed in the Matlab (The MathWorks, Natick, MA, USA), by custom-made software. The detailed description of the single steps is reported in the following.

Volume preprocessing

PDUS and CEUS volumes were converted in grayscale format (gray levels ranged between 0 – black to 1 – white). For PDUS, we extracted the color map containing the vascular information. Two different thresholds of 50% and 70% of the maximum gray level of each image were applied to PDUS and CEUS volumes, respectively, to highlight signal from vessels. Fig. 4.2.A and fig. 4.2.B show two representative slices of the original PDUS and CEUS volumes of the same nodule are reported. The thresholding step results are depicted in fig. 4.2.C and fig.4.2.D respectively.

Vessel enhancement filtering

In PDUS and CEUS images, due to resolution and signal-to-noise ratio limitations, the representation of the vascular network is suboptimal. Hence, we proposed a vessel-enhancement filter to improve the representation of the vascular structure of the nodules. The filter was designed partly following the formalism of the multiscale enhancing filter proposed by Frangi et al. [23].

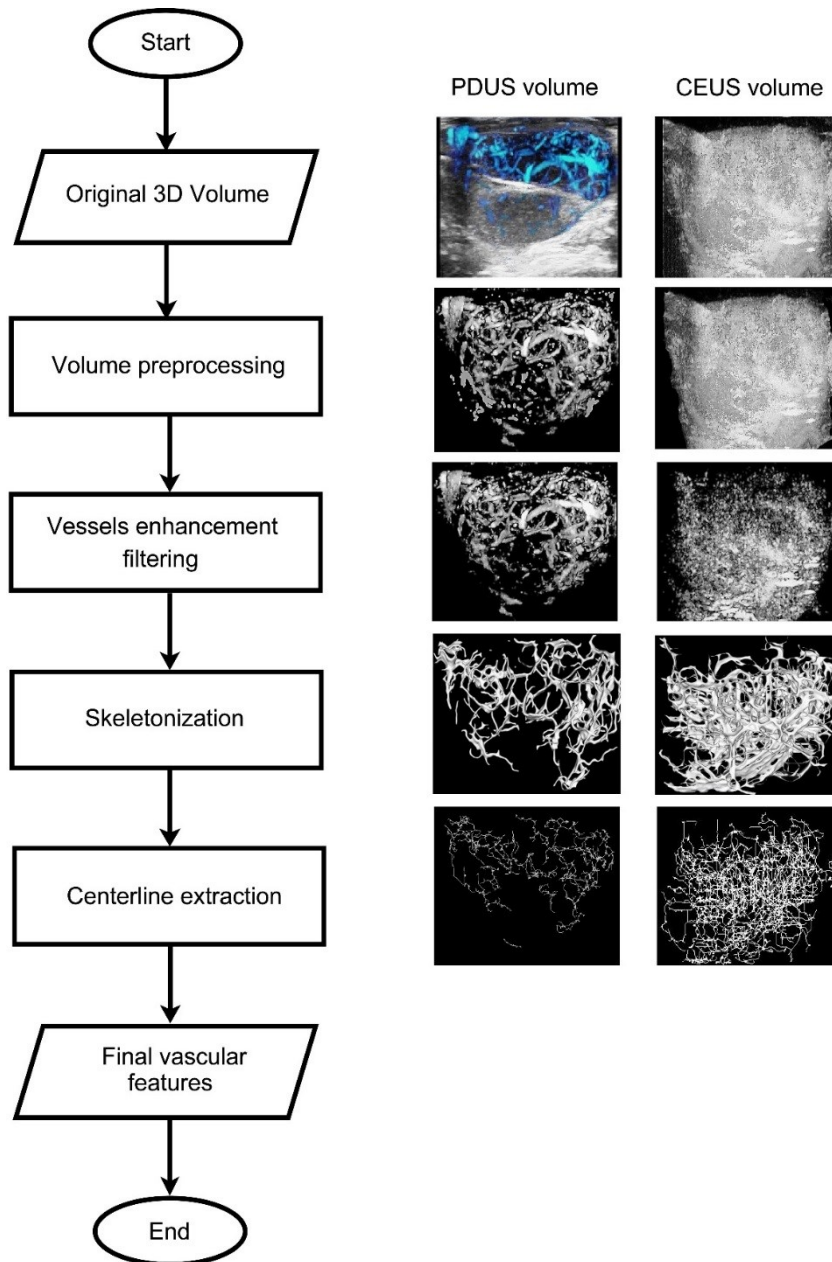


Figure 4. 1: Schematic representation of the processing steps for PDUS and CEUS volumes.

In our study, four different scale dimensions equal to $\sigma = 1, 2, 3, 4$ were chosen in the computation of four respective 3-D Gaussian kernels. This choice was made to tune the filter dimension on the width and length of tumor vessels (between 1-4 voxel, where 1 voxel approximately corresponded to $0.05 \times 0.05 \times 0.05$ mm). Each Gaussian kernel was applied to the Volume V (size $L \times M \times N$) to obtain four 3-D Hessian matrices. For each single voxel of i, j and k coordinates, the three eigenvalues λ were computed and sorted in a way that

$$|\lambda_{1(i,j,k)}| \geq |\lambda_{2(i,j,k)}| \geq |\lambda_{3(i,j,k)}|$$

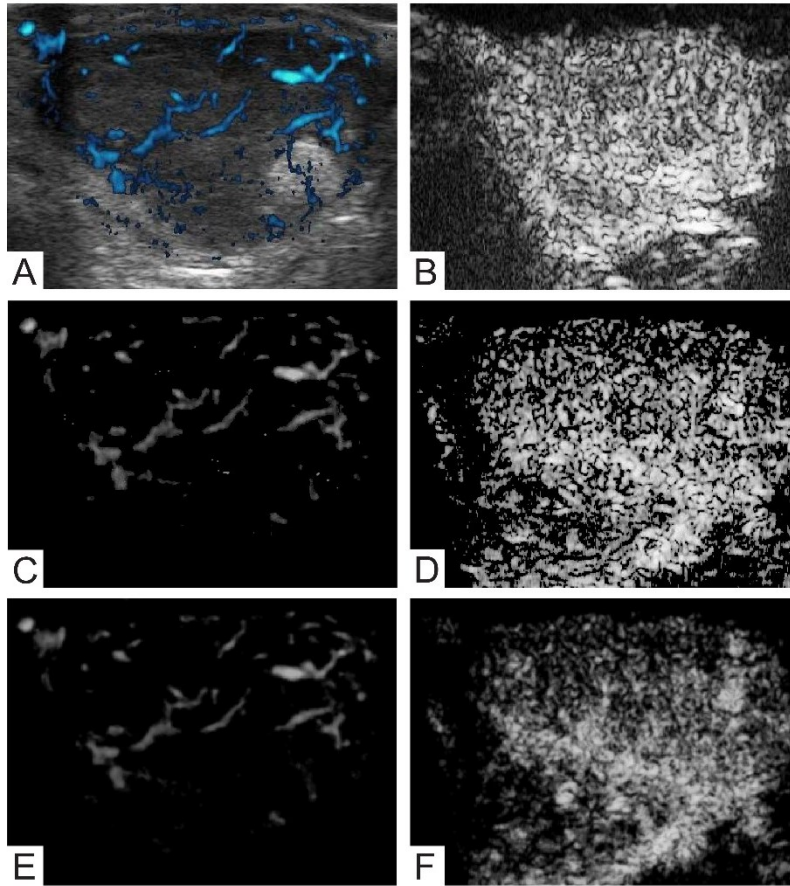


Figure 4. 2: Preprocessing steps and vessel enhancement filtering for the 3-D PDUS and CEUS volumes in a malignant tumor. Panels A, B - Original PDUS in and CEUS slices. Panels D, E - Preprocessing step for the PDUS and CEUS slices. Panel F, G -Vessel enhancement filtering for the PDUS and CEUS slices.

The volumetric response of the voxel VR at a specific σ is computed as

$$S(i, j, k) = \sqrt{\lambda_{1(i,j,k)}^2 + \lambda_{2(i,j,k)}^2 + \lambda_{3(i,j,k)}^2}$$

$$VR_{\sigma}(i, j, k) = \begin{cases} 0 & \text{if } S(i, j, k) = 0 \text{ and } \lambda_{1(i,j,k)} = 0 \\ A_{(i,j,k)} = \frac{\lambda_{1(i,j,k)}}{S(i, j, k)} & \text{in all other case.} \end{cases}$$

The value of $A_{(i,j,k)}$ is the local measurement of the Signal-to-Noise Ratio (SNR) of the volumetric image, namely the vessels flux power compared to the background. For each of the four VR_{σ} matrices created, the candidate Winning Factor WF_{σ} is computed as

$$WF_{\sigma} = \sum_{1=i,j,k}^{L,M,N} VR_{\sigma}.$$

The four WF_{σ} are sorted in ascending values of σ and the maximum value among these elements is the final Winning Factor for each voxel, corresponding to the chosen value of σ . Examples of the vessels enhancement filtering are reported in fig. 4.2.E and fig 4.2.F for PDUS and CEUS slices.

Vascular network extraction: skeleton and centerline

Two cascaded algorithms were applied to optimize the tumor vascular representation. Since tumor vascular patterns are featured by both vessels shape (vascular trees and branches) and the blood flow intensity, morphological and functional information can be extracted from the PDUS and CEUS volumes. This extraction was made possible combining two techniques, namely a skeletonization of the 3-D vessels followed by the centerline extraction.

An initial non-minimal skeletonization processing step was applied to obtain a morphological thinner representation of vessels, highlighting the vascular pathways, without loss of connectivity.

In the beginning of the skeletoning process, the 3-D volumes were globally thresholded to create a 3-D binary mask with the vascular component set to 1 (white) and background at 0 (black). From this step on, a morphological thinning algorithm was applied frame by frame and along each axis in order to find the minimal skeleton of the vascular network.

The skeleton algorithm considers each pixel P belonging to a single frame of the binary mask and the respective 8-connected neighborhood according to the following scheme:

X_4	X_3	X_2
X_5	P	X_1
X_6	X_7	X_8

The pixel P was eroded if and only if the following two conditions were simultaneously met:

- $P = 1$, hence it belongs to a vessel structure;
- $2 \leq N(P) \leq 3$, where

$$N(P) = \sum_{i=1}^4 X_{2i-1} \vee X_{2i} = \sum_{i=1}^4 \{X_1, X_3, X_5, X_7\} \vee \{X_2, X_4, X_6, X_8\}.$$

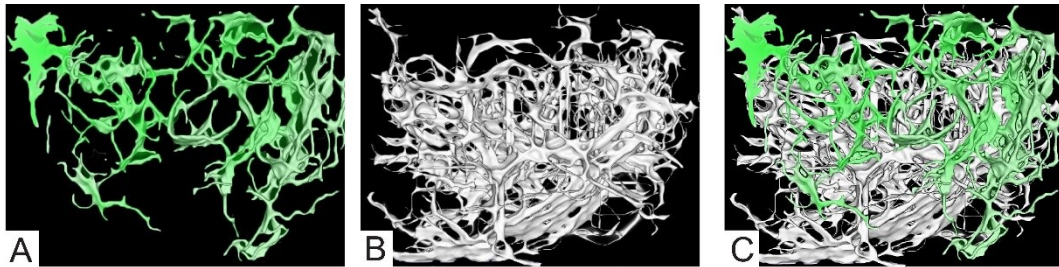


Figure 4.3: 3-D rendering of the vascular architecture obtained from the skeleton algorithm. The same thyroid nodule is shown, acquired with PDUS in Panel A and with CEUS in Panel B. Panel C - Overlap of the two renderings.

The algorithm preserved branches connectivity and deleted non-physiological spurious branches shorter than the threshold of 70 voxels. Example of 3-D vascular skeletons obtained from this processing are reported in fig. 4.3.A for PDUS volume and fig 4.3.B for CEUS volume. The overlaid skeletons are represented in fig. 4.3.C.

The second methodology applied in this work is the centerlines algorithm; compared with the skeleton algorithm, the centerline computation is performed on the blood flow intensity information. This algorithm is partly inspired by a common explicit approach based on the intensity of Height Ridge Transversal and multiscale extraction [24] and depicted in fig. 4.4.

Starting from the non-minimal skeleton mask overlaid on the original volume, a specific number of candidate points, named seeds, are selected according to the

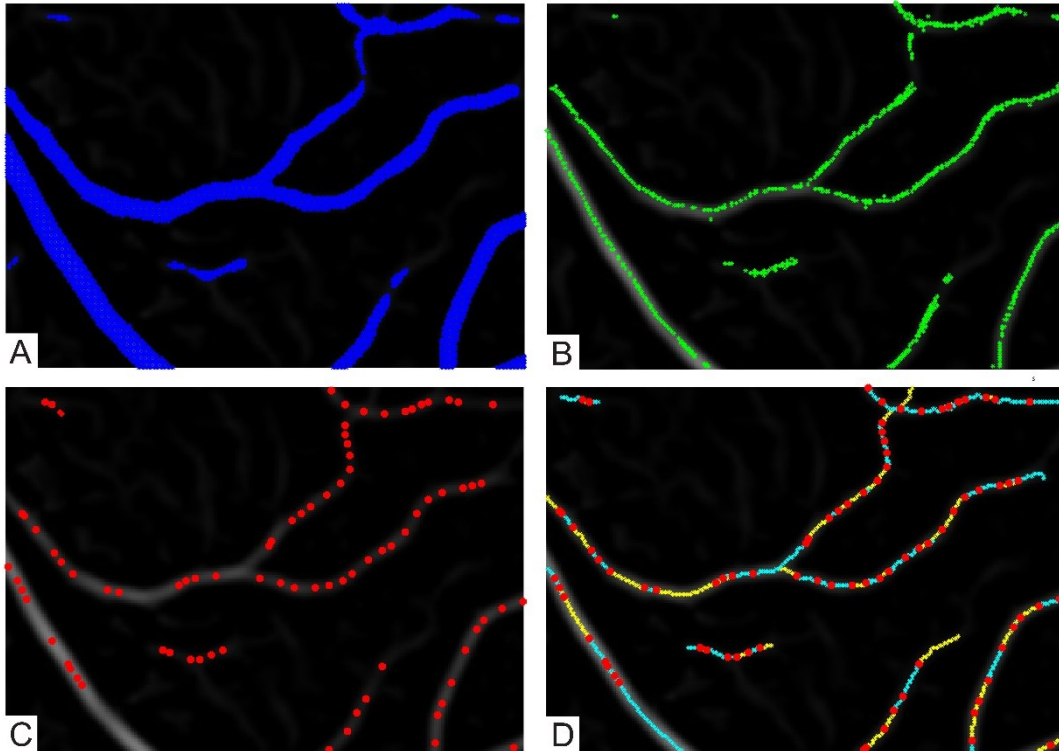


Figure 4. 4: Main steps of the centerline algorithm. Panel A - representation of initial seed points. Panel B - identification of the 1-D maximum candidates. Panel C - selection of the ridge points. Panel D - forward (in yellow) and backward (in cyan) path of search.

intensity threshold, equal to the 20% of the maximum gray-level of the image (fig 4.4.A).

The 26-connected neighborhood of each seed point is considered, and the search of the ridge is performed along the line that joins the seed point and the maximum intensity voxel in the neighborhood. If the intensity difference between the seed point and the maximum intensity voxel of the neighborhood is higher than 0, the direction is saved for the following iteration, otherwise the seed point is defined 1-D maximum candidate and the search ends. This operation allows to get closer to the central part of the vessel, where the blood flow is maximum (fig 4.4.B).

All the candidate 1-D maximum voxels are required to meet all the criteria that are presented and cited in [24] in order to be considered as ridge points; the results of this search is presented in fig 4.4.C.

After all the ridge points are detected, an intensity-based search of the centerline is performed. Starting from the first ridge point, the maximum intensity voxel in its 26-connected neighborhood is labelled as the first voxel of the centerline and defines the forward path of search (fig. 4.4.D). From this new voxel, another maximum intensity voxel is identified in its neighborhood and the process is iteratively repeated along the forward path. 26-connected neighborhood already visited in the previous iterations are forbidden. This process is needed because, in bifurcation or stenosis regions, where the hypothesis of laminar flow becomes less substantial and the blood flow could be higher in peripheral regions of the vessel, the centerline could deviate from its real location. Forbidding these kernel positions does not allow the centerline to deviate from its central path. The specific 3-D masks of the forbidden positions are shown in the APPENDIX D.

The search of the forward path ends when one of the following conditions is matched:

- the search reaches another ridge point;
- the current path crosses itself or another previously traced path;

- the search reaches a single point onto the volume boundary or in the background.

When the forward path of search ends, the search is repeated, starting from the first voxel opposite of the first point found near to the considered ridge point. The search continues in the opposite direction, along the backward path of search, following the same criteria of the forward path of search.

When all the forward and backward paths of search are found, a post-processing algorithm links the split centerlines whose distance between their closest endpoints is lower than 5 voxels. In fig. 4.4.D ridges, forward and backward path of search are highlighted. The final result after the application of the centerline algorithm is shown in fig. 4.5 (panels A – C PDUS volume, panels B - D CEUS volume).

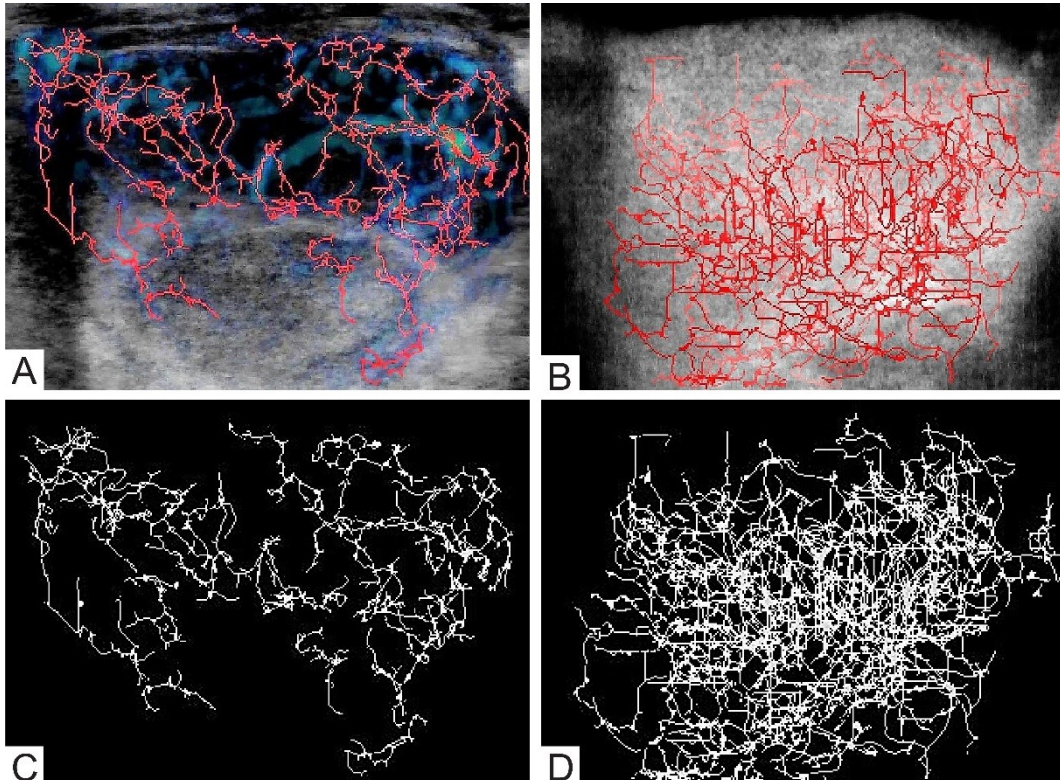


Figure 4. 5: 3-D centerline extraction. Panel A, B - Centerline pattern (in red) overlapped to the original 3-D PDUS and CEUS volumes. Panel C, D - 3-D rendering of the centerline for PDUS and CEUS volumes.

Automatic features extraction for vascular quantitative analysis

Once the centerlines were obtained, a quantitative vascular features extraction was performed in order to characterize the tumor malignancy.

In our study, 7 blood vessels-related features were calculated: three of them were tortuosity metrics, and the remaining four were related to the tumors vascular architecture. In the computation of vascular features, the centerline was mapped using an iterative procedure which isolated vascular trees T according to the position of the nodes:

$$CTree = \{T_1, T_2, \dots, T_N\}$$

where N is the number of vascular trees. Each vascular tree T_i can be thought as the sequence of m nodes $T_i = \{p_1, p_2, \dots, p_m\}$.

The three tortuosity metrics, already introduced by [25] and reported in APPENDIX E are:

1. Distance Metric (DM), which computes the ratio of the length of the vessel and the linear Euclidean distance between its endpoints;
2. Inflections Count Metric (ICM), which is obtained by the product of the number of inflection points N_{InfP} and the DM , plus 1. The N_{InfP} value is obtained using the geometrical representation of the Frenet frame already described [26], [27]. This parameter is an estimation of the average number of time the vascular tree changes its shape from convex to concave and vice-versa in a 3-D framework;
3. Sum Of Angles Metric (SOAM), which calculates the total angles of the curve as a sum for each point and normalizes the result by dividing by the total curve length.
4. Vascular Volume Density (VVD, %), which is obtained by the ratio of the total space occupied by the blood vessels and the total tumor size, expressed in voxels;

5. Number of vascular Trees (NT), which is the number of the vascular networks;
6. Number of vascular Branches (NB), which is the branches of the tumor vascular pattern identified by branchpoints.
7. Spatial Vascularity Pattern (SVP), which evaluates whether the vascular patterns are more concentrated peripherally (perilesional vascularization) or inside the tumor (intranodular vascularization).

This last feature is calculated as follows:

- three intensity profiles of the entire volume were calculated, summed and normalized along the three principal axes X, Y and Z. The resulting normalized vascular intensity profile was an indicator of how vascularity was distributed into the entire volume of the tumor;
- from this vascular intensity profile, the second order polynomial was interpolated;
- the first order derivative of such a polynomial was calculated;
- the tumor presented a perilesional vascularization if this first derivative was either always positive, or always negative, or simply monotonically increasing;
- in case the previous requirements were not met, the tumor was classified as intranodular.

Since benign nodules are frequently associated with a perilesional architecture, while a malignant lesions commonly present a intranodular vascularization, the final SVP score was reported as a fraction of positive perilesional benign on the total benign nodules or positive intranodular malignant on the total malignant tumors [38].

All the features, except for the VVD and the SVP, which were calculated on the entire volume, were computed in 3 Volumes of Interest (VOIs) automatically generated around the highest gray-level intensity voxels, i.e. in those points where the density of blood vessels is higher. The size of the three VOIs was 5 times

smaller than the original 3D image along the x and y axes, while along the z axes it was kept as the half of the image size (this is due to limited number of slices along the z direction). The final value for each feature was obtained as the average of the three values calculated in each VOI.

Statistical Analysis and Classification

In this work, 20 thyroid tumors (10 benign and 10 malignant) were analyzed and the features extraction was applied on both PDUS and CEUS volumes. For the two group of tumors, mean values and standard deviation for the first six continuous features (DM, ICM, SOAM, VVD, NT and NB) and the discrete fraction of SVP parameter were reported. Since the Shapiro-Wilk test failed for both the techniques, the comparison between benign and malignant nodules was performed using a non-parametric Mann-Whitney U-test.

Multivariate Analysis of Variance (MANOVA) was used to test the equality of the means between benign and malignant nodules. Before conducting the MANOVA analysis, collinear variables were removed to avoid singularities in the observation matrix. The collinearity of variables was checked by computing the Wilks' lambda. The dimension of the MANOVA was used to assess the number of groups the data belong to. Classification of the tumor as benign or malignant was obtained by linear regression analysis performed on the most significant features, as revealed by the MANOVA. The statistical significance is set to $p \geq 0.05$. Statistical analyses were performed in Matlab.

CEUS	Benign Tumors	Malignant Tumors	p-value
DM (a.u.)	13.91 \pm 8.31	82.93 \pm 49.38	<< 0.05
ICM (a.u.)	35.78 \pm 18.63	227.62 \pm 93.97	<< 0.05
SOAM (a.u.)	4.28 \pm 3.19	26.51 \pm 21.19	<< 0.05
VVD (%)	30.30 \pm 11.40	60.30 \pm 7.11	<< 0.05
NT (a.u.)	5.30 \pm 1.34	8.40 \pm 2.79	<< 0.05
NB (a.u.)	18.30 \pm 5.83	53.70 \pm 17.72	<< 0.05
SVP (a.u.)	6/10	10/10	<< 0.05

Table 4. 1: Mean values \pm standard deviation and p-value of the 6 vascular features analyzed for CEUS volumes. The SVP is reported as a fraction of perilesional benign tumor and intranodular malignant tumors on the total number of tumor of the respective group.

PDUS	Benign Tumors	Malignant Tumors	p-value
DM (a.u.)	6.37 \pm 4.98	31.12 \pm 24.14	<< 0.05
ICM (a.u.)	23.95 \pm 16.93	153.80 \pm 132.49	<< 0.05
SOAM (a.u.)	1.93 \pm 1.19	11.31 \pm 10.15	<< 0.05
VVD (%)	25.7 \pm 11.83	43.00 \pm 14.57	<< 0.05
NT (a.u.)	4.70 \pm 2.00	8.50 \pm 2.27	<< 0.05
NB (a.u.)	9.80 \pm 7.06	28.20 \pm 12.95	<< 0.05
SVP (a.u.)	9/10	10/10	<< 0.05

Table 4. 2: Mean values \pm standard deviation and p-value of the 6 vascular features analyzed for PDUS volumes. The SVP is reported as a fraction of perilesional benign tumor and intranodular malignant tumors on the total number of tumor of the respective group.

4.3 Results

In table 4.1 and table 4.2 mean values \pm standard deviations of the six continuous features and the discrete parameter SVP previously described are reported for PDUS and CEUS volumes respectively. The two tables show that

vascular continuous parameters are all higher for malignant tumors than benign ones for both techniques.

The result of the Mann-Whitney U-test shows a significant difference between the benign and malignant nodules for both PDUS and CEUS techniques for all the continuous features (DM, ICM, SOAM, VVD, NT, NB).

For the SVP feature, 9 out of 10 and 6 out of 10 benign nodules were labelled as perilesional for the PDUS and CEUS volumes respectively, while malignant nodules were all classified as intranodular (10/10) for both the techniques.

Fig. 4.6 shows an example of 3-D vascular rendering of two benign and malignant thyroid tumors for both PDUS (fig. 4.6.A and fig 4.6.C) and CEUS (fig 4.6.B and fig 4.6.D) techniques. It is evident that the benign nodule (fig. 4.6.A and fig 4.6.B) displays a lower peripheral vascular density than the malignant one (fig. 4.6.C and fig 4.6.D). The respective normalized vascular intensity profiles (fig. 4.6.E and fig. 4.6.F), indicates that the SVP parameter classifies the benign nodule as perilesional and the malignant tumor as intranodular for both PDUS and CEUS techniques.

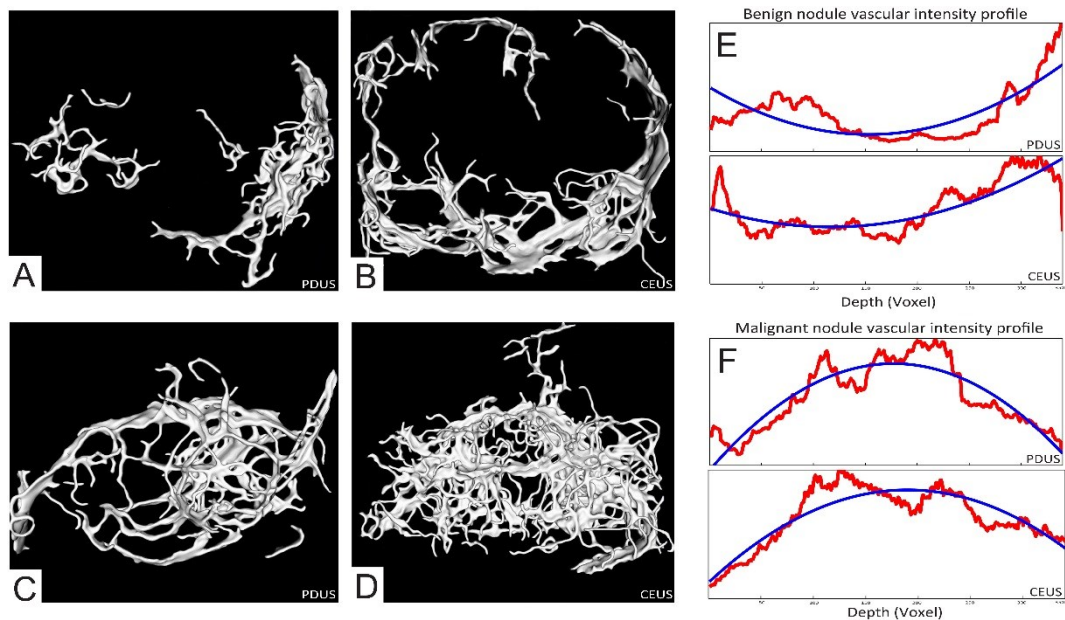


Figure 4. 6: 3-D vascular rendering of a representative benign tumor (top panels) and malignant tumor (bottom panels). Panels A, C - 3-D PDUS reconstructions. Panel B, D - display 3-D CEUS volumes. Panels (E - benign) and (F - malignant) show the normalized vascular intensity profile obtained by summing the three x, y, and z intensity profiles for PDUS and CEUS volumes.

After this first step of statistical processing, the MANOVA is applied on data considering all the significant 9 features of this study: patient age, patient gender, ICM, DM, SOAM, VVD, NB, NT, SVP. For each subject, the parameter SVP was reported as a binary value of 0 if the tumor was perilesional or 1 if it was intranodular.

When the tumor type (benign or malignant) was considered as a dependent variable, after removing the collinear variables in common for both the PDUS and CEUS volumes, 5 features were left (ICM, VVD, NT, SVP and patient age). The optimal Wilks' lambda values for our data set were found to be 0.03 for the PDUS and 0.13 for the CEUS techniques. The MANOVA dimension of the group means was equal to 1 ($p \ll 0.001$ for both PDUS and CEUS). The dimensionality of the MANOVA was important to understand how samples were distributed on the hyperplane of the canonical variables. We plotted the first and second canonical variable for each subject for PDUS (fig. 4.7.A) and CEUS techniques (fig. 4.7.B), and we indicated the benign tumors by an empty symbol (circle) and malignant tumors by a full one. The graph indicates that the first canonical variable was discriminant for the tumor type. The most discriminant feature was ICM, followed, in the order, by VVD, NT, SVP and patient age. By using these features, a classification of tumors based on the linear regression was performed. All the thyroid nodules were correctly classified, with sensitivity and specificity of 100% and an area under the receiver operating curve (AUROC) equal to 1.

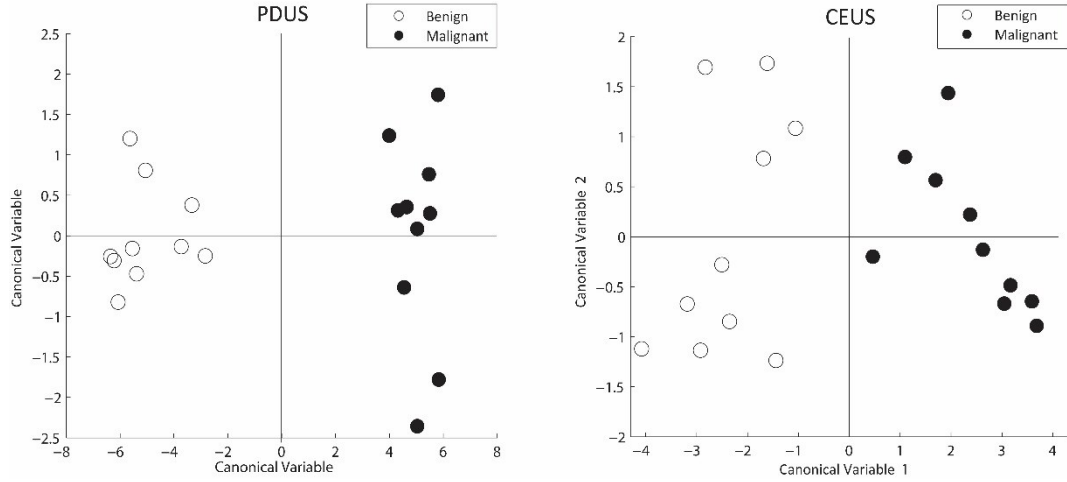


Figure 4. 7: Representation of patients in the plane of the first two canonical variables obtained by MANOVA. The vascular features ICM, VVD, NT, SVP and patient age allow for a clear separation of the patients according to the tumor type (benign or malignant). The empty circles represent the benign nodules and the full symbols the malignant lesions.

4.4 Discussion

Tumor vasculature plays fundamental role in tumor invasion and has gained critical importance in the assessment of benign or malignant lesions. However, challenges remain on how to outline blood vessels features that can serve as clinically useful markers to help clinicians in the diagnosis and to guide the treatment. Vascular ultrasound imaging like 3-D PDUS and CEUS techniques are valuable tool in the differential diagnosis, although they are mainly used as functional imaging techniques in perfusion and blood flow studies rather than showing the morphological tumor vascular network. In this work, we developed and presented a systematic and versatile method for reconstructing the thyroid tumor vascular network for the subsequent automatic computation of seven morphological vessel-related features. Our algorithm can extract morphological details to vascular ultrasound volumes, making them suitable for a vasculature quantitative analysis.

To address this task, we first used a vessel-enhancement filter to overcome signal-to-noise ratio limitations and therefore to improve the representation of the

vascular network, automatically tuning the scale parameter σ of the filter on the local vessels' dimension. The main advantage obtained by using this filter is a denoising effect, which allows to keep only the vascular information on the images and to correct intensity inhomogeneities. Subsequently, a skeleton and a centerline extraction algorithm are applied. The former is useful to add morphological information to the images, while the latter relies on blood flow information, which is outstanding in vascular ultrasound images. Since tumor vascular patterns are featured by both vessels shape (vascular trees and branches) and blood flow intensity, the combination of the two algorithms can provide an accurate representation of angiogenic blood vessels and quantitative analysis based on vascular features extraction.

Vascular features were quantified by the measurements involving three tortuosity metrics (DM, ICM and SOAM), number of trees and branches (NT, NB), vascular volume density (VVD) and spatial vascularity pattern (SVP).

These features (except for the last two) are computed within three VOIs automatically created around the maximum intensity voxels of tumor vascularity. This choice has been made to capture highly concentrated blood vessels areas and to avoid vessels-free areas.

Finally, the latter two features, VVD and SVP evaluate the global information of the tumor. The vascular volume density assesses the grade of vascularization of the nodule, while the spatial vascularity pattern, a parameter inspired by the clinical practice which has not been previously proposed in literature, gives an estimation on where, within the tumor volume, blood vessels are more concentrated.

The numerical values of these features were reported in terms of mean and standard deviation for the two techniques (PDUS and CEUS) adopted in this study. Exploiting all the morphological features, high accuracy in the description of tumor vascularity can be achieved. Furthermore, the statistical analysis resulted in very low p-values ($p \ll 0.05$), indicating that all these features can be used to significantly discriminate benign from malignant tumors.

The MANOVA analysis shows that a minimum set of common vascular parameters can be used to distinguish benign from malignant tumors for both PDUS and CEUS techniques. Following the discriminant features' weight order, only one out of three tortuosity metrics, the ICM, is needed to discriminate nodules. This finding suggests that malignant thyroid nodules present vessels with evident higher degree of inflection and this characteristic is dominant compared to the simple computation of curvature of DM and the presence of coil shapes detected by SOAM. Furthermore, the features related to the tumor volume, the NT and the VVD, demonstrate to be more discerning in the classification, in line with the previous findings [27]. In the canonical variables hyperplane, the newly introduced parameter SVP proves to be effective in the separation of groups, even though some benign tumors could present the intranodular pattern typical to the malignant ones in both ultrasound techniques; this result highlights the reliability of the multiparametric approach, able to combine different aspects of geometry and morphology, such as radiomics can combine semantic attribute to agnostic features to improve diagnostic and prognostic results.

Few comparisons arise from our results regarding the performance and the diagnostic accuracy of the two ultrasound modalities adopted in this study. As expected, the tumor vascular network reconstructed from the CEUS volumes shows much more vessels than the 3-D rendering obtained from the PDUS volumes. This is true for all the patient images in our dataset. These different results are due to the intrinsic limitations given by the spatial resolution of the two techniques. In fact, CEUS employs microbubbles as contrast agent. This allows to improve the resolution and therefore to detect also angiogenetic neo-formed blood vessels. These latter are not detectable by the PDUS, whose resolution constraints make this technique suitable to detect only major tumor vascularity [19].

Despite this difference, the quantitative analysis of tumor images from the two imaging techniques shows comparable results. This suggests that it could be sufficient to compute the vessel-related features only on tumor major vessels

(detected both with PDUS and CEUS) and not on angiogenetic vessels (detected only with CEUS). Moreover, PDUS could be sufficient for a proper analysis of thyroid tumors vascular networks as a diagnostic indicator, with the advantage of being fully non-invasive, as no contrast medium is required, and less expensive. Avoiding the use of a contrast agent could also allow to include a higher number of patients in future clinical trials, since the examination would be totally cost-effective.

Our study reveals a correlation between the morphology of vascularity in thyroid lesions and malignancy. Furthermore, it reveals a strong correlation between the PDUS and the CEUS in terms of accuracy in diagnosis. However, the system still has limitations. In fact, some malignant thyroid nodules in advanced stage could present a high rate of necrotic tissue, thus completely non-vascularized. Such nodules, due to the absence of blood vessels, could be misclassified as benign nodules with perilesional vascularization. This is not an overwhelming limitation, since usually these malignant nodules show other non-vessels-related biomarkers of malignancy which are apparent to the clinicians (nodule size, growth rate, singularity, hypothyroidism). The proposed method is instead accurate in classifying highly-vascularized thyroid tumors, and therefore can provide a valuable tool for helping physicians in clinical decisions with suspicious lesions.

The images were processed using a 2.4 GHz CPU, 12 GB RAM workstation. The total time for a complete evaluation of a thyroid nodule (including all steps of the algorithm) is about 45 minutes, although the computational time much depends on the image size and on the amount of blood vessels evaluated. The algorithm can still be optimized in order to reduce the computational time. Furthermore, it can be speeded up by using lower level languages like C++ and/or parallel processing, especially using Graphic Processing Units (GPU).

4.5 Conclusion

Power Doppler UltraSound (PDUS) and Contrast-Enhancement UltraSound (CEUS) imaging techniques can be used in the assessment and differential diagnosis of thyroid nodules vasculature. The proposed strategy provides the tumor vascular network visualization in full anatomy and enables the extraction of many numerical morphological features. With the presented algorithm, it is possible to estimate the thyroid nodule's malignancy, providing a fast and non-expensive diagnostic tool able to reduce the number of biopsies and overtreatments, helping physicians in clinical decisions and improving the diagnostic process with a higher level of accuracy.

The quantitative shows comparable results between CEUS and PDUS, suggesting also that PDUS can be potentially effective in the diagnosis of thyroid tumors malignancy.

Future work includes the evaluation of the performance of the algorithm using a bigger and more heterogeneous patients' dataset. A CAD system could also be built upon the proposed methods, including other non-vessels-related features to provide a more comprehensive analysis of thyroid tumors. This method could be used for a quantitative evaluation of other emerging ultrasound modalities, like high-resolution photoacoustic imaging and acoustic angiography.

4.6 References

- [1] J. Folkman, "What is the evidence that tumors are angiogenesis dependent?," *J. Natl. Cancer Inst.*, vol. 82, pp. 4–6, 1990.
- [2] P. Carmeliet and R. K. Jain, "Angiogenesis in cancer and other diseases.," *Nature*, vol. 407, pp. 249–257, 2000.
- [3] A. Kurjak, S. Kupesic, B. Breyer, V. Sparac, and S. Jukic, "The assessment of ovarian tumor angiogenesis: what does three-dimensional power Doppler add?," *Ultrasound Obstet. Gynecol.*, vol. 12, pp. 136–146, Aug. 1998.
- [4] N. Nishida, H. Yano, T. Nishida, T. Kamura, and M. Kojiro, "Angiogenesis in cancer.," *Vasc. Health Risk Manag.*, vol. 2, pp. 213–219, 2006.
- [5] S. F. Huang, R. F. Chang, W. K. Moon, Y. H. Lee, D. R. Chen, and J. S. Suri, "Analysis of Tumor Vascularity Using Ultrasound Images," *IEEE Trans. Med. Imaging*, vol. 27, pp. 320–330, 2008.

- [6] N. Tanigawa, M. Matsumura, H. Amaya, A. Kitaoka, T. Shimomatsuya, C. Lu, R. Muraoka, and T. Tanaka, "Tumor vascularity correlates with the prognosis of patients with esophageal squamous cell carcinoma," *Am. Cancer Soc.*, vol. 79, pp. 220–225, Jan. 1997.
- [7] V. Goh, S. Halligan, F. Daley, D. M. Wellsted, T. Guenther, and C. I. Bartram, "Colorectal tumor vascularity: quantitative assessment with multidetector CT-do tumor perfusion measurements reflect angiogenesis?," *Radiology*, vol. 249, pp. 510–517, Nov. 2008.
- [8] C. Balu-Maestro, C. Chapellier, A. Bleuse, I. Chanalet, C. Chauvel, and R. Largillier, "Imaging in evaluation of response to neoadjuvant breast cancer treatment benefits of MRI," *Breast Cancer Res. Treat.*, vol. 72, pp. 145–152, 2002.
- [9] P. Marckmann, L. Skov, K. Rossen, A. Dupont, M. B. Damholt, J. G. Heaf, and H. S. Thomsen, "Nephrogenic systemic fibrosis: suspected causative role of gadodiamide used for contrast-enhanced magnetic resonance imaging," *J. Am. Soc. Nephrol.*, vol. 17, pp. 2359–2362, 2006.
- [10] S. G. Moore, P. J. Shenoy, L. Fanucchi, J. W. Tumeh, and C. R. Flowers, "Cost-effectiveness of MRI compared to mammography for breast cancer screening in a high risk population," *BMC Health Serv. Res.*, vol. 9, p. 9, 2009.
- [11] T. Hata, K. Hata, D. Senoh, K. Makihara, S. Aoki, O. Takamiya, and M. Kitao, "Doppler ultrasound assessment of tumor vascularity in gynecologic disorders," *J. ultrasound Med.*, vol. 8, pp. 309–314, 1989.
- [12] C. Nicolau, R. Vilana, V. Catalá, L. Bianchi, R. Gilabert, A. García, and C. Brú, "Importance of evaluating all vascular phases on contrast-enhanced sonography in the differentiation of benign from malignant focal liver lesions," *Am. J. Roentgenol.*, vol. 186, pp. 158–167, 2006.
- [13] K. Hoyt, A. Sorace, and R. Saini, "Quantitative mapping of tumor vascularity using volumetric contrast-enhanced ultrasound," *Invest. Radiol.*, vol. 47, pp. 167–174, 2011.
- [14] S. Gerst, L. E. Hann, D. Li, M. Gonen, S. Tickoo, M. J. Sohn, and P. Russo, "Evaluation of renal masses with contrast-enhanced ultrasound: initial experience," *Am. J. Roentgenol.*, vol. 197, pp. 897–906, 2011.
- [15] C. H. Wu, M. M. Hsu, Y. L. Chang, and F. J. Hsieh, "Vascular pathology of malignant cervical lymphadenopathy: qualitative and quantitative assessment with power Doppler ultrasound," *Cancer*, vol. 83, pp. 1189–96, Sep. 1998.
- [16] S.-F. Huang, R.-F. Chang, W. K. Moon, Y.-H. Lee, D.-R. Chen, and J. S. Suri, "Analysis of tumor vascularity using three-dimensional power Doppler ultrasound image," *IEEE Trans. Med. Imaging*, vol. 27, pp. 320–330, 2008.
- [17] B. Sun, L. Lang, X. Zhu, F. Jiang, Y. Hong, and L. He, "Accuracy of contrast-enhanced ultrasound in the identification of thyroid nodules: A meta-analysis," *Int. J. Clin. Exp. Med.*, vol. 8, pp. 12882–12889, 2015.
- [18] R.-J. Schroeder, M. Bostanjoglo, J. Rademaker, J. Maeurer, and R. Felix, "Role of power Doppler techniques and ultrasound contrast enhancement in the differential diagnosis of focal breast lesions," *Eur. Radiol.*, vol. 13, pp. 68–79, 2003.
- [19] C. Caresio, M. Caballo, M. Deandrea, R. Garberoglio, A. Mormile, R. Rossetto, P. Limone, and F. Molinari, "Optimized quantification of thyroid nodular vascularization from 3-D contrast-enhanced ultrasound images," in *European symposium on Ultrasound Contrast Imaging*, 2017.
- [20] M. H. Wu, C. N. Chen, K. Y. Chen, M. C. Ho, H. C. Tai, Y. H. Wang, A. Chen, and K. J. Chang, "Quantitative analysis of echogenicity for patients with thyroid nodules," *Sci. Rep.*, vol. 6, pp. 1–8, 2016.
- [21] C. La Vecchia, M. Malvezzi, C. Bosetti, W. Garavello, P. Bertuccio, F. Levi, and E. Negri, "Thyroid cancer mortality and incidence: a global overview," *Int. J. Cancer*, vol. 136, pp. 2187–2195, 2015.
- [22] L. Davies and H. G. Welch, "Increasing Incidence of Thyroid Cancer in the United States, 1973-2002," *JAMA*, vol. 295, pp. 2164–2167, 2006.
- [23] D. Yu, Y. Han, and T. Chen, "Contrast-Enhanced Ultrasound for Differentiation of Benign and Malignant Thyroid Lesions: Meta-analysis," *Otolaryngol. -- Head Neck Surg.*, vol. 151, pp. 909–915,

- 2014.
- [24] M. Chammas, R. Gerhard, I. de Oliveira, A. Widman, N. de Barros, M. Durazzo, A. Ferraz, and G. Cerri, "Thyroid nodules: evaluation with power Doppler and duplex Doppler ultrasound," *Otolaryngol. Head Neck Surg.*, vol. 132, pp. 874–882, 2005.
 - [25] Y. Liu, H. Liu, C.-L. Qian, M.-S. Lin, and F.-H. Li, "Utility of quantitative contrast-enhanced ultrasound for the prediction of extracapsular extension in papillary thyroid carcinoma," *Sci. Rep.*, vol. 7, p. 1472, 2017.
 - [26] Y. Zhang, Y. Luo, M. Zhang, J. Li, J. Li, and J. Tang, "Diagnostic Accuracy of Contrast-Enhanced Ultrasound Enhancement Patterns for Thyroid Nodules," *Med. Sci. Monit.*, vol. 22, pp. 4755–4764, 2016.
 - [27] T. V. Bartolotta, M. Midiri, M. Galia, G. Runza, M. Attard, G. Savoia, R. Lagalla, and A. E. Cardinale, "Qualitative and quantitative evaluation of solitary thyroid nodules with contrast-enhanced ultrasound: Initial results," *Eur. Radiol.*, vol. 16, pp. 2234–2241, 2006.
 - [28] M. H. Wu, C. N. Chen, K. Y. Chen, M. C. Ho, H. C. Tai, Y. C. Chung, C. P. Lo, A. Chen, and K. J. Chang, "Quantitative Analysis of Dynamic Power Doppler Sonograms for Patients with Thyroid Nodules," *Ultrasound Med. Biol.*, vol. 39, pp. 1543–1551, 2013.
 - [29] F. Molinari, A. Mantovani, M. Deandrea, P. Limone, R. Garberoglio, and J. S. Suri, "Characterization of Single Thyroid Nodules by Contrast-Enhanced 3-D Ultrasound," *Ultrasound Med. Biol.*, vol. 36, pp. 1616–1625, 2010.
 - [30] J. Kong, J. Li, H. Wang, Y. Wang, R. Zhao, Y. Zhang, and J. Jin, "Role of Superb Micro-Vascular Imaging in the Preoperative Evaluation of Thyroid Nodules: Comparison With Power Doppler Flow Imaging," *J. Ultrasound Med.*, vol. 36, pp. 1329–1337, 2017.
 - [31] P. Cowling, A. Chandra, and T. Giles, "Guidance on the reporting of thyroid cytology specimens," *R. Coll. Pathol.*, no. 261035, 2016.
 - [32] D. N. Poller, Z. W. Baloch, G. Fadda, S. J. Johnson, M. Bongiovanni, A. Pontecorvi, and B. Cochand-Priollet, "Thyroid FNA: New classifications and new interpretations," *Cancer Cytopathol.*, pp. 1–10, 2016.
 - [33] R. Acharya, S. Sree, M. Mookiah, F. Molinari, R. Garberoglio, and J. S. Suri, "Non-invasive automated 3D thyroid lesion classification in ultrasound: A class of ThyroScan systems," *Ultrasonics*, vol. 52, pp. 508–520, 2012.
 - [34] R. Garberoglio, F. Molinari, L. Manzoli, S. De Beni, L. Lodigiani, and L. Forzoni, "Virtual Biopsy and Three Dimensional Ultrasound for Radio Frequency Ablation of Thyroid Nodules," in *European Society of Radiology*, 2015, pp. 1–15.
 - [35] A. F. Frangi, W. J. Niessen, K. L. Vincken, and M. a Viergever, "Multiscale vessel enhancement filtering," *Medial Image Comput. Comput. Intervention - MICCAI'98. Lect. Notes Comput. Sci. vol 1496*, vol. 1496, pp. 130–137, 1998.
 - [36] S. R. Aylward and E. Bullitt, "Initialization, noise, singularities, and scale in height ridge traversal for tubular object centerline extraction," *IEEE Trans. Med. Imaging*, vol. 21, pp. 61–75, 2002.
 - [37] E. Bullitt, G. Gerig, S. M. Pizer, W. Lin, and S. R. Aylward, "Measuring Tortuosity of the Intracerebral Vasculature from MRA Images," *IEEE Trans Med Imaging*, vol. 22, pp. 1163–1171, 2003.
 - [38] A. Lyshchik, R. Moses, S. L. Barnes, T. Higashi, R. Asato, M. I. Miga, J. C. Gore, and A. C. Fleischer, "Quantitative analysis of tumor vascularity in benign and malignant solid thyroid nodules," *J. ultrasound Med.*, vol. 26, pp. 837–846, 2007.

Chapter 5

Quantitative assessment of cancer growth in 3-D preclinical acoustic angiography

This chapter has been built upon:

A. Panfilova, S. Shelton, R.J.G. van Sloun, C. Caresio, H. Wijkstra, P. Dayton and M. Mischi, **Which properties of the vascular architecture are reflected by dynamic contrast-enhanced ultrasound imaging of dispersion and wash-in rate? A comparison with acoustic angiography.**, *IEEE Proceedings IUS 2017*, September 6 - 9th, 2017 Washington, D.C., USA.

5.1 Introduction

Ultrasound is a popular modality for imaging animal models of human diseases because of its portable, relatively low cost, and present a real-time modality [1].

In the past decade, Contrast-Enhanced UltraSound imaging (CEUS) has demonstrated to be reliable in the quantification of blood vessels architecture in thyroid and breast tumor [2]–[5]. Conventional CEUS imaging relies on receiving the acoustic signal scattered from microbubbles of the ultrasound contrast agents (UCAs) at the fundamental frequency [6], however, frequencies ranges (1-12 MHz) and image reconstruction techniques (such as harmonic imaging, subharmonic imaging, phase inversion, contrast pulse sequence, and contrast harmonic imaging) limit the spatial resolution and the background signal scatter suppression.

High-resolution ultrasound imaging has been demonstrated to be effective in non-invasive preclinical studies, in which rodents are extensively used in the assessment of tumor development or to therapy's response studies [7]–[10].

The recent design of ultra-broadband, multi-frequency ultrasound transducers has enabled high sensitivity, high-resolution contrast imaging, with very efficient suppression of tissue background using a technique called Acoustic Angiography (AA) [11].

AA is a significant development in CEUS imaging, based on the application of dual-frequency ultrasound transducer, but still only available as prototype devices in preclinical protocols [12]. In AA imaging, the UCA lipid-encapsulated bubbles with a diameter in the range of $0.8 - 4 \mu\text{m}$, are excited at the resonance by a low frequency ultrasound transducer element in a range between 2-4 MHz, while the echoes are received with a second transducer at a much higher frequency (25-30 MHz).

The high frequency receiver can detect the broadband super-harmonic signal emitted by the excited UCA, filtering the negligible energy background tissue scatters at this frequency [13].

The dual frequency approach improves substantially the resolution, though it limits the penetration depth due to attenuation of high frequency signals from the microbubbles [14]. Therefore, AA is an extremely efficient in the visualization of superficial micro-vessels structure and is an ideal tool in the representation of abnormal vascular morphology in cancer angiogenesis. Specifically, AA has demonstrated to be considerable advanced in ultrasound imaging technology and enables the meaningful quantification of vascular architecture in angiogenic networks [6], [11], [12]. Moreover, the analysis of abnormal vascular network's morphology within a diseased tissue volume provides a methodology in the assessment of the therapy's effects, which is essential in the design of personalized medical treatments [15].

Tumor vasculature results in an abnormal network with disorganized, twisted and tortuous blood vessels, with uneven diameters and irregular branching patterns, density, and permeability [16]. The accurate quantification of tumor vessels tortuosity is particularly challenging in large volumes and in case of complex and chaotic structures. In several past works, automatic algorithms for the primary vascular path extraction based on the Breadth First Search [17] were proposed and applied in CEUS and photoacoustic imaging [2], [18]. Though the BFS approach is computationally convenient for the analysis of a selected Volume of Interest (VOI), the investigation is reductive, in case of large intricate structures, since it relies on values extracted from a unique vascular path, without ramifications, which might not represent the overall tumor tortuosity; in addition, the main disadvantage consists in the absence of local information within the considered VOI.

Recent AA studies have characterized the tortuosity of tumor vasculature and found it significantly higher than that of control tissue [19], in spatial comparisons [20], and according to the tumor dimension [11]; in all these works implemented in AA, a manually-defined individual vessel segmentation and analysis method, based on the Aylward-Bullitt multiscale centerline extraction algorithm, were applied [21]. Moreover, the tortuosity characterization of vessels was made possible by

means of the tortuosity metrics described in Bullitt et al. [22]. Although this methodology has been proven to be effective in the assessment of control and abnormal vasculature, it still requires the manual selection of centerline seed points, which is time consuming and user-dependent. Moreover, in recent studies, only few visible vessels were selected by an experienced operator [11], reducing the analysis to a small set of samples.

In this chapter, a novel, fully automated strategy for vessel segmentation and vascular features extraction for high-spatial-resolution high-contrast imaging is proposed. This methodological approach is applied on 3-D AA acquisitions of 8 rats implanted with fibrosarcoma tumor, imaged at 4 time points (TPs) with a 3-days interval. The analysis is conducted on the manually traced cubic VOIs which include all the tumor lesion and on the surrounding control region of each 3-D scan.

Global vascular parameters, such as the global number of trees (GNT), global number of branches (GNB) and the vascular volume density (VVD) are extracted from a specific VOI, whereas vascular parametric maps of local architectural parameters, such as local number of branching nodes (LNB), number of trees (LNT), local diameter (LD) and tortuosity metrics (DM, ICM, SOAM) are calculated to completely characterize and quantify the angiogenetic tumor architecture of tumor and control areas VOIs, overcoming the major limitations of the manual selection or the use of sub-optimal automatic approach.

A preliminary study on pooled data of tumors vs surrounding control areas is carried out in order to confirm the previous findings on quantitative AA [19]; a further longitudinal study on vascular tumor VOIs and control areas VOIs evolution along 4 time points of AA acquisitions are carried out in order to verify if there are significant differences, for each parameter, in time for both tumor and control area VOIs; finally, a comparison between an ideal control VOI and the 4 TPs tumor VOIs is investigated in order to discover which are the parameters more sensitive in the differentiation of the tumor stage.

5.2 Materials and Methods

5.2.1 Rats preparation and AA acquisition

Fibrosarcoma tumor models were implanted from propagated tumor tissue provided by the Dewhirst Lab at Duke University. Rats (Fischer 344) were anesthetized with isoflurane and a 2 mm incision was made above the quadriceps muscle and a piece of tumor tissue (approximately 1 mm³) was implanted subcutaneously. This procedure was performed on 8 rats, which were operated on the same day. When the tumors were palpable, AA acquisitions of the tumor-bearing flank were performed while the animals were anesthetized with vaporized isoflurane in oxygen. For all animals, imaging started on day 8 from the operation, with subsequent acquisitions every 3 days, amounting to 4 time points (TPs). All experiments were approved by the Institutional Animal Care and Use Committee at the University of North Carolina at Chapel Hill [23].

AA images were acquired with a prototype dual-frequency transducer, transmitting at 4 MHz and receiving at 30 MHz [11], [20]. A continuous infusion of UCA was administered using a syringe pump (PHD 2000, Harvard Apparatus) at a rate of 1.5×10^8 microbubbles per minute. The 3-D images were acquired with a linear motion stage using an inter-frame step of 100 μm [14], then linearly interpolated to obtain an isotropic form of 50 μm voxels using Matlab (The MathWorks Inc., Natick, MA).

5.2.2 Tumor microvasculature 3-D mapping and analysis

Volume processing

In this section the algorithm of the tumor angiogenetic vessel segmentation and vascular skeleton extraction in AA volume is presented. The complete pipeline of processing is sketched in fig. 5.1.

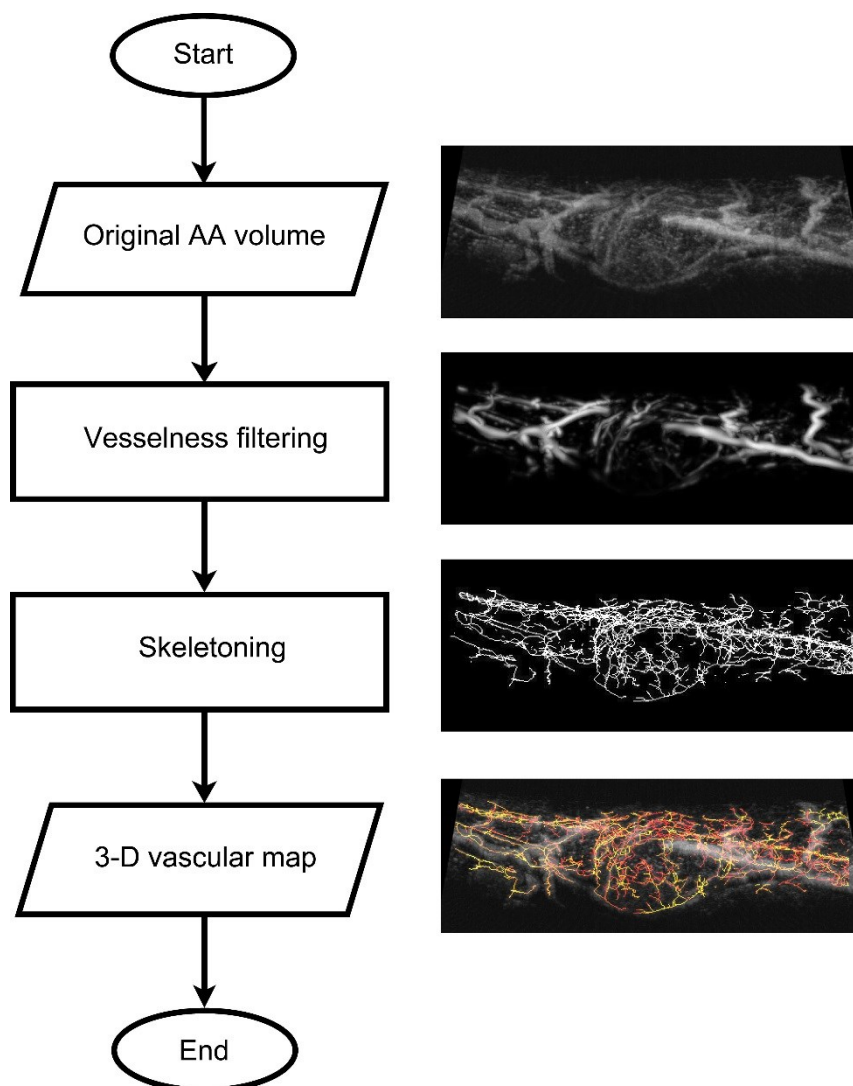


Figure 5. 1: Schematic representation of the AA volume processing steps.

Although the signal-to-noise ratio in AA imaging is considerably higher compared to CEUS conventional imaging, the AA volumes need to be preprocessed in order to reduce the background scatter and uniform the gray level intensity within vessels. Starting from the original volume (fig 5.2.A) regularization along the elevation plane and volume equalization for contrast improvement are initially applied (fig 5.2.B).

The AA volume is subsequently filtered with a multiscale vessel enhancement filter [24], already named Vesselness filter, which is particularly suitable for “angiographic” image [25]. Vesselness filter parameters are adjusted to highlight specific vessels’ shape and dimension. Since the voxel dimension is equal to 50 μm and AA volumes show tumor’s vessel diameters ranging between 50 – 250 μm , the Vesselness filter σ value is set in the range of 1-5 voxels, in a way that 25 equally spaced diameter sizes, with an in-between-step of 10 μm , are calculated.

The implementation of the 3-D filter has been taken from Frangi et al. [24] and defined as:

$$V_{\sigma} = \begin{cases} 0 & \text{if } \lambda_2 > 0 \text{ or } \lambda_3 > 0 \\ \left(1 - e^{\left(-\frac{R_a^2}{2\alpha^2}\right)}\right) e^{\left(-\frac{R_b^2}{2\beta^2}\right)} \left(1 - e^{\left(-\frac{S^2}{2c^2}\right)}\right) & \text{in all other case.} \end{cases}$$

where $\lambda_1, \lambda_2, \lambda_3$ are the eigenvalues extracted from the Hessian matrix parameters, α, β and c are thresholds which control the sensitivity of the filter to the measure of $R_a = \frac{|\lambda_2|}{|\lambda_3|}$ (line-like structure), $R_b = \frac{|\lambda_1|}{\sqrt{\lambda_2}}$ (blob-like structure) and $S = \sqrt{\lambda_1 + \lambda_2}$ (second order structureness). α is set to 0.1 and β to 9 in order maximize the detection of vessel-like structures and minimize the blob-like structures [25]. c value is set adaptively to the half the value of the maximum Hessian norm. The final result is reported in Fig 5.2.C.

After the application of the Vesselness filter, the AA volume is converted in the binary format and a heuristic cleaning of residual 3-D structures smaller than

10 voxels and with eccentricity lower than 0.5 is applied, generating the Vesselness Binary Mask (Fig 5.2.D). This step of cleaning is fundamental for the subsequent detection of big vascular trees and the computational time and cost reduction.

The Vesselness binary mask is processed to obtain the vascular skeleton according to the parallel medial axis homotopic thinning method proposed by Lee [26]. The maximum intensity projection of the final result is depicted in fig. 5.2.E.

The vascular skeleton is computed to enable the extraction the vascular features already discussed in Chapter 4. Due to the complexity of the vascular exanimated structures, two different approaches in the extraction of vascular parameters are

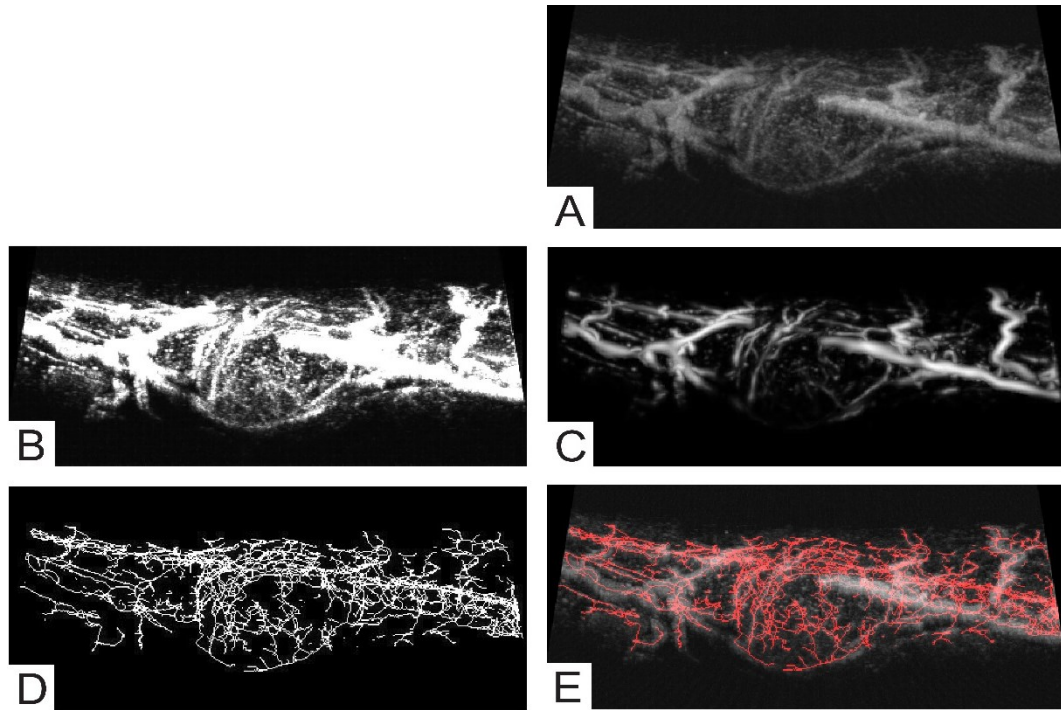


Figure 5. 2: Panel A – Original volume. Panel B - Volume with adjusted contrast. Panel C – Vesselness binary mask. Panel D – Skeletonization. Panel E - Original volume and overlaid skeleton (in red).

proposed in the following: global architectural parameters referable to a specific volume are directly computed from the skeleton, while tortuosity measurements are locally computed within a moving 3-D window. In addition, local vascular architectural parameters are also mapped as in the case of tortuosity measurements.

Volumetric architectural features extraction

From each 3-D vascular skeleton, a Volume of Interest (VOI) enclosing the tumor is manually selected and measured. In absence of a contralateral AA angiography acquisition as previously reported in [6], [11], [12], we assumed as a control area the surrounding visible tissue section of each tumor VOI.

Four vascular architectural global parameters are extracted from both the Tumor VOI and the Control VOI; they are the global number of vascular trees (GNT), the global number of branches (GNB) the vascular volume density (VVD, %), which is the percentage of space occupied by vessels within a specific volume.

Vascular features mapping

In order to locally map the tumor vasculature captured by the AA acquisition, the vascular network represented by the 3-D skeleton are quantitatively analyzed applying, iteratively, a moving 31 pixels width 3-D window centered on each voxel of the skeleton; for each 3-D window considered, the Breadth First Search (BFS) algorithm [17],[18] is applied and five vascular parameters, both architectural and tortuosity measurements, are automatically computed as follows in order to locally map the vascular network on each point of the skeleton (APPENDIX E):

1. Local Number of Trees (LNT), which defines the number of connected s decomposes the skeleton volume;
2. Local Number of Branching nodes (LNB), ramification of each tree;
3. Distance Metric (DM): defined as the ratio between the actual path length of the curve and the linear distance between the first and last point of the curve, where each curve represents a vessel;
4. Inflections Count Metric (ICM): defined as the DM multiplied by the number of inflection points found along the vessel path;
5. Sum of Angles Metric (SOAM): defined as the sum of all the angles that a curve has in space. This tortuosity measurement is used to handle tight coils.

All the computed parameters were already mathematically described and discussed in previously published works [22] and in APPENDIX E. A further map, the Local Diameter (LD) map is obtained according to the values locally extracted from the Vesselness binary mask using the vascular skeleton voxels points as a guide. LNT and LNB maps were specifically computed for qualitative evaluation,

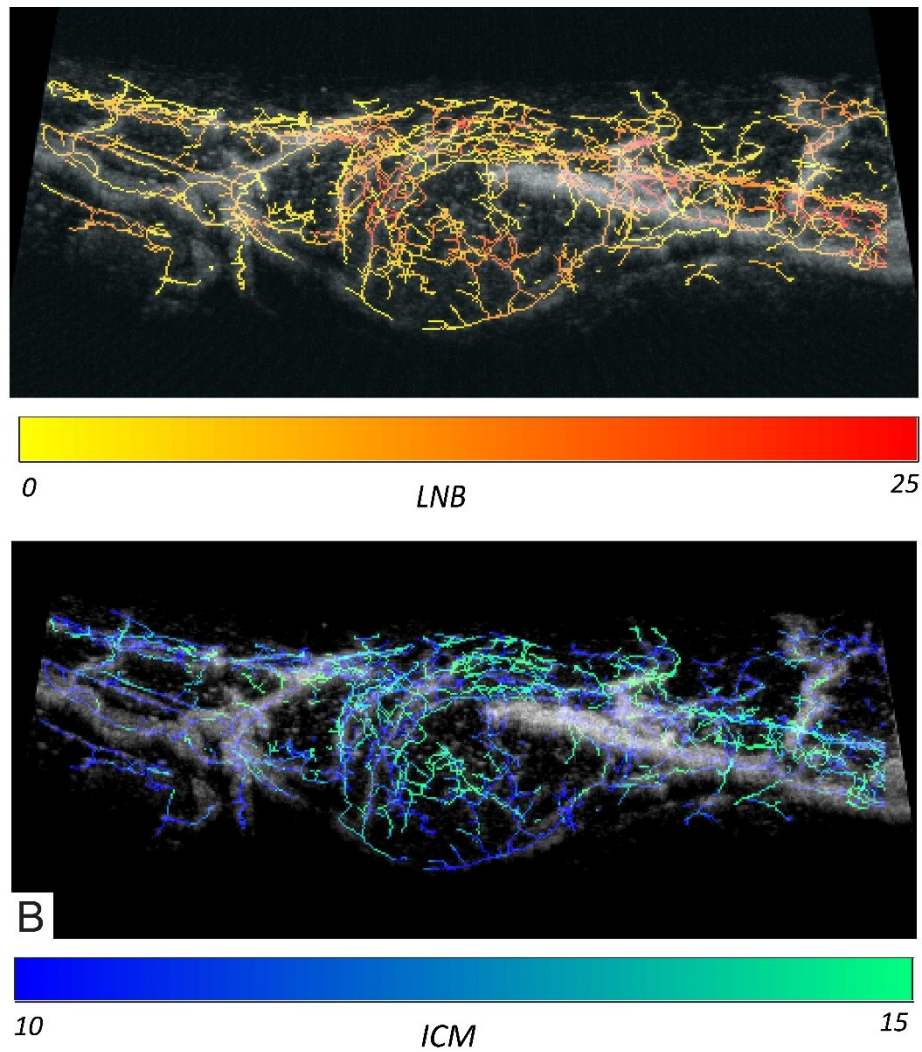


Figure 5.3 Vascular parameters maps. Panel A – Local number of Branches (LNB) map, for qualitative evaluation. Panel B – Inflections Count Metric (ICM) map.

while tortuosity maps were calculated for further statistical analysis. Two significant examples of vascular maps are presented in Fig. 5.3.A for the LNB and Fig. 5.3.B the ICM tortuosity.

5.2.3 Statistical Analysis

From each AA volume, a tumor VOI and the complementary control area VOI are extracted and global architectural vascular parameters (GNT, GNB and VVD), local averaged tortuosity measurements (DM, ICM, SOAM) and local vessels diameter (LD) are calculated within the two VOIs for each rat and each TP.

Regarding each vascular parameter, three studies are made on the 8 rats AA data and on each TP.

First, a tumor vs control area comparison with pooled data, with all the TPs, is conducted to prove the statistical differences between the two regions, applying a non-parametric Mann-Whitney U-test.

Then, a longitudinal study to prove the statistical differences between the four TPs both for tumor VOIs and control area VOIs are performed with a repeated measurements Friedman's test followed by a Fisher's post hoc test for paired data.

Finally, a Kruskal-Wallis test followed by a Dunn's post hoc test established the differences between the TP2 point control area, taken arbitrary as the global control, and the four tumor VOI TPs. This comparison was made to establish which parameter(s) is/are more sensitive in the recognition of tumor vasculature at different stages. All the data are expressed as average \pm standard deviation and all the statistical analysis was performed in Matlab.

5.3 Results

The first column of Table 5.1 resumes the results of the Mann-Whitney U-test between tumor regions and control areas for all the vascular parameters. Pooled data from tumor dimension VOIs (expressed in mm^3) are statistically higher than the control VOIs.

From the comparison between tumor VOIs and control area VOIs, it is evident that all the vascular parameters are significantly different between the two regions. In particular, GNB, GNT, VVD, DM, ICM and SOAM appear to be significantly higher whereas LD is significantly lower in tumor VOIs compared to control VOIs. These results are in line with all the previous findings [23]. Representative examples of tumor evolution are shown in fig 5.4. where the 4 TPs of the same tumor are depicted and the two maps of LD and SOAM are reported.

Considering only the significant comparisons, the Fisher's post hoc test after Friedman's test conducted on multiple repeated measurements (4 TPs) reveals, among the main findings, that tumor Volume raises considerably along the 4 TPs, while it is kept almost constant for all the control areas VOIs; in addition, GNT and GNB tumor TP1 is statistically lower compared to TP3 and TP4 respectively,

GNT tumor TP4 is significantly higher than TP1, TP2 and TP3; moreover, VVD of tumor TP1 is statistically higher, in descending order, compared to TP2, TP3, and TP4. VVD is slightly reduced along the control area TPs, while it drastically decreases along the 4 tumor TPs. On the other hand, GNT of control area TP1 is statistically higher than TP4, while GNB does not change in time. In the case of LD, control area TP1 appears significantly lower, in ascending order, to TP2, TP3 and TP4. LD appears almost constant for all the tumor VOIs TPs, while it raises on the control area VOIs. All the tortuosity measurements do not change significantly along the four TPs for both tumor VOIs and control area VOIs.

		p-value	TP1	TP2	TP3	TP4
Volume (mm ³)	T	< 0.05	738.1 ± 449.4	1262.1 ± 627.8	1749.1 ± 584.0	2581. ± 730.7
	C		1246.4 ± 436.1	1061.8 ± 252.1	1034.2 ± 313.6	984.8 ± 371.3
GNB	T	< 0.01	1044 ± 611	1445 ± 970	1779 ± 1225	2737 ± 1898
	C		894 ± 486	774 ± 290	653 ± 385	414 ± 232
GNT	T	< 0.01	54 ± 34	77 ± 39	104 ± 44	160 ± 62
	C		81 ± 25	49 ± 19	44 ± 16	37 ± 26
VVD (%)	T	< 0.01	20.8 ± 6.1	13.7 ± 2.1	10.2 ± 3.7	10.0 ± 2.8
	C		7.4 ± 1.3	6.9 ± 1.6	6.6 ± 2.5	4.3 ± 1.7
LD (μm)	T	< 0.01	109 ± 9	110 ± 3	108 ± 6	108 ± 3
	C		111 ± 7	121 ± 8	120 ± 6	118 ± 8
DM	T	< 0.01	3,0 ± 0.6	2,6 ± 0.5	2,7 ± 0.4	2,9 ± 0.5
	C		2,2 ± 0.4	2.0 ± 0.3	2,2 ± 0.3	2,3 ± 0.5
ICM	T	< 0.01	15,3 ± 1.9	14,4 ± 1.5	14,4 ± 1.5	14,8 ± 1.8
	C		12,5 ± 1.2	11,9 ± 1.1	13,2 ± 1.1	13,4 ± 2.0
SOAM	T	< 0.01	1,5 ± 0.2	1,4 ± 0.2	1,4 ± 0.1	1,4 ± 0.2
	C		1,2 ± 0.1	1,1 ± 0.1	1,2 ± 0.2	1,2 ± 0.3

Table 5. 1: Results of the vascular parameters extraction and mapping. The first column represents the results of the statistical comparison between tumor (T) and control (C) VOIs, along the 4 TPs. GNT = Global Number of Trees. GNB = Global Number of Branches. VVD = Vascular Volume Density. LD = Local Diameter; D = Distance Metric. ICM = Inflections Count Metric. SOAM = Sum of Angles Metric.

From the Dunn's post hoc test after the Kruskal-Wallis test for comparison between a reference control (TP2) and the four tumor TPs, a statistical difference is found for GNB and GNT on TP4, VVD (higher) in TP1 and TP2 while the LD is significantly smaller in tumor TP1, TP3 and TP4. Considering the three tortuosity metrics, the highest number of significant comparisons is obtained with SOAM

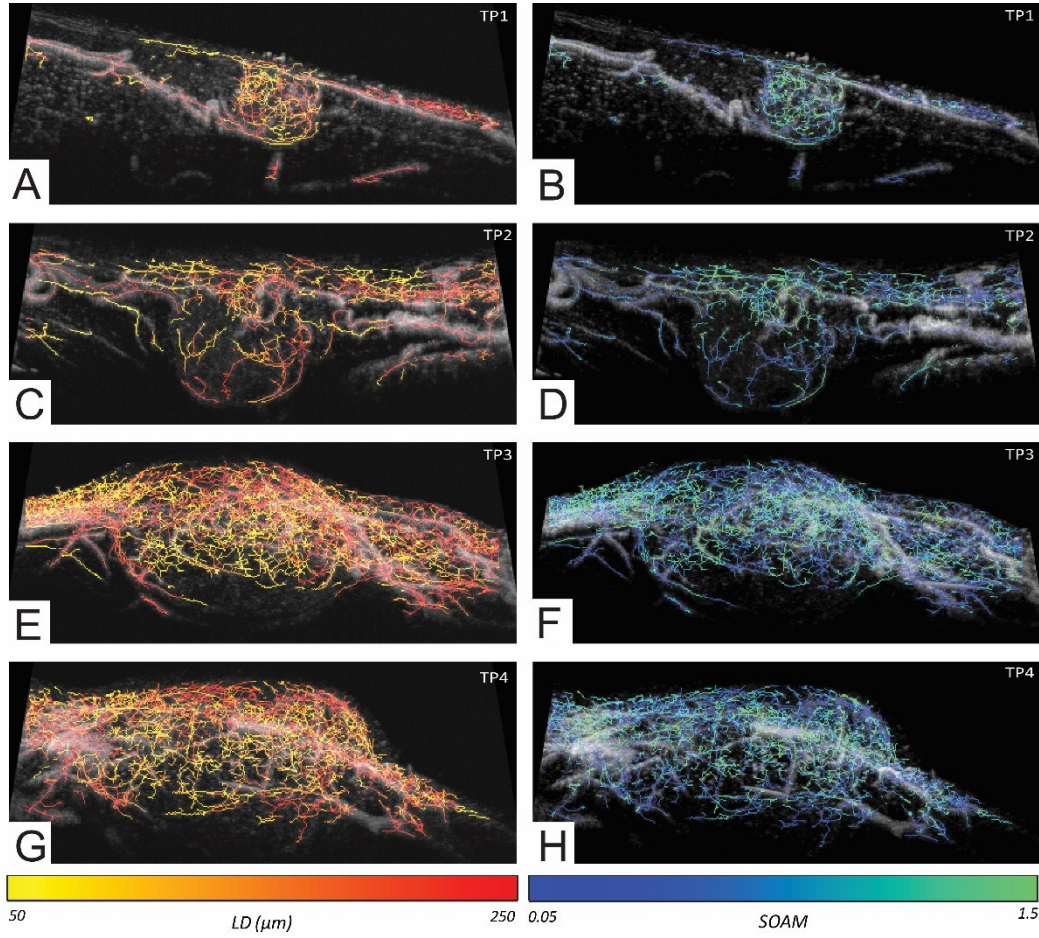


Figure 5. 4: Example of the same fibrosarcoma tumor investigated with AA imaging along the 4 TPs of invasion and growth. Parametric maps for Local Diameter (LD, panels A-C-E-G) and Sum of Angles Metric (SOAM, panels B-D-F-H) are reported in the 3-D representation.

metric which is statistically higher in all the four tumor TPs. Fig 5.5 shows boxplot diagrams of all the seven parameters for the comparison between the control area VOI and the four tumor TPs. Boxplots of tumor VOIs put in evidence the presence of ascending (GNT, GNB) and descending (VVD) trends or constant behavior (LD, DM, ICM, SOAM) of vascular parameters along the four TPs.

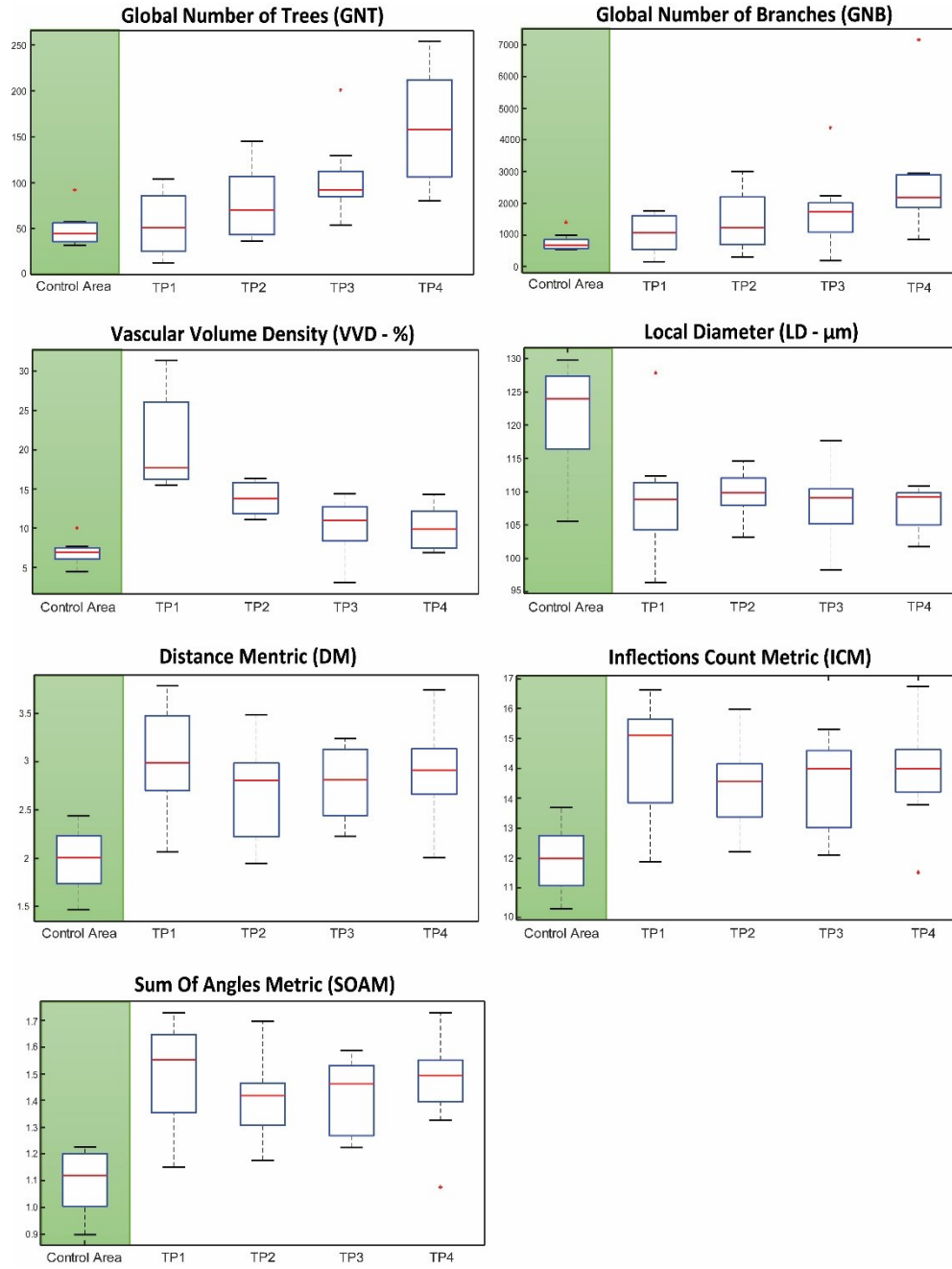


Figure 5. 5: Boxplot diagrams of all the seven parameters for the comparison between the control area VOI and the four tumor TPs in 8 rats.

5.4 Discussion

In this chapter, a quantitative analysis on vascular architecture captured by the AA acquisitions has been proposed. 8 rats with implanted fibrosarcoma tumors underwent ultrasonic high-resolution examination in a 3-days interval study (a total of 24 days between the last acquisition and the tumor implantation); the novelty of this study consists in the application of a new automatic strategy based on multiscale filtering and vascular skeleton computation for vascular features extraction. Vascular architectural parameters (GNT, GNB, VVD, and LD) and tortuosity measurements (DM, ICM and SOAM) have been calculated using the same approach proposed in previous works [2], [3], [18], [22]. The analysis of tortuosity and architecture has been extended to the computation and local mapping (LNT and LNB) by means of the application of the BFS extraction on a moving 3-D window. Statistical analysis has been carried out on tumor and control areas VOIs at different levels of detail and diverse research questions have been answered.

Firstly, a pooled data comparison between tumor and control area VOIs has been made to prove the significant difference of vascular parameters between the two regions; table 5.1 shows how architectural parameters and tortuosity metrics are higher for tumor VOIs compared to the control area, while MR is significantly smaller. These findings confirm the results of previous works in the field of preclinical AA [11], [19] in which VVD, DM and SOAM appeared to be higher in tumor VOIs. Furthermore, this study completes and extends the analysis of tumor angiogenic network to the objective quantification of vascular trees and branches, enabled by the vascular skeleton extraction, and the computation of the local vessel diameter, made possible with the use of a Vesselness scale filter and already used and discussed in [18].

The separate analysis of tumor and control areas VOIs along the TPs shows that the tumor evolution and growth is characterized by the significant raise of GNT and GNB, an almost constant value of LD and a considerable drop of VVD along the

four TPs. These results suggest that tumor angiogenic process, under the vascular endothelia growth factors (VGEFs) stimuli, starts immediately after the implantation [27], [28] and involves a rapid creation of intricate neo-vessels, which branch out from current tumor trees and develop at small constant diameter ($108,6 \pm 5 \mu\text{m}$). Since implanted fibrosarcoma tumors in rat models triplicate their volumes in only 12 days (from around 700 mm^3 up to around 2500 mm^3), but VVD (namely the percentage of space occupied by vessels within the tumor) diminishes constantly along the four TPs (already observed, in a similar ways with the Microvascular Volume Density, MVD, in [23]), we can presume that cancer ischemia and ultimately necrosis, occurring inside out from the first TP and fragmenting the current vascular network in a higher number of trees, progresses constantly as the tumor continues to grow [29], [30], and leads the aggressive angiogenesis to expand around the tumor shell. Similar results were already discussed in Shelton et al. [11], where the authors report an increase of tumor vascular heterogeneity in a longitudinal study with tumors binned according to the size, and within this thesis, in Chapter 4, where malignant thyroid nodules mainly presented a peripheral vasculature. For the architectural parameters, the Fisher post hoc test, conducted on multiple repeated measurements statistics, finds significant comparisons only between tumor VOIs TP1 and the others. This finding might indicate that, for this cancer type, a critical change in tumor evolution occurs less than 12 days from the inoculation.

Considering the vascular architecture of the control area VOIs, we observe that the GNT diminishes in time, GNB and VVD are constant, and LD raises considerably between the first and the subsequent three TPs. These results are in agreement with previous finding on the behavior of tumor's surrounding areas, which are expected to undergo, at the same time of tumor growth, a significant vascular remodeling [29]. As the tumor volume increases, a smaller number of control trees are visible, and vessels mean diameters raises to ease and intensify the

blood flow in carrying oxygen and nutrients towards hyperproliferating cancerous tissues.

Considering the vessels tortuosity inside tumor and control areas VOIs, it has been observed that averaged values of DM, ICM and SOAM metrics do not change significantly in time within the two regions. This result suggests two possible and mutual conclusions: first, tumor and control areas were correctly manually identified, and they maintain a characteristic vascular arrangement, in terms of tortuosity, along the four TPs. Secondly, regarding the tumor VOIs, we can suppose that, with the only availability of fibrosarcoma tumors, that tortuosity is intrinsically related to the cancer type and malignancy grade [31], as it was observed for the characteristic number of vessels and MVD in a previous study [32] and in the assessment of the angiogenic progression in breast cancer stages [33].

The comparisons between the reference control area VOIs and the four tumor VOIs TPs reveals that, although there is only one statistical difference in GNB and GNT between the reference and TP4, VVD shows higher values in tumor TP1 and TP2, as well as the value of LD in reference area is statistically greater compared to tumor TP1, TP3 and TP4. Since this preliminary study was conducted on a small sample set, selecting complementary volumes that changed considerably along the TPs (see Mann Whitney test, first column of table 5.1) and in absence of a ground truth control region (such as the contralateral flank), there is poor scientific evidence supporting the ability of global architectural parameters, as GNB and GNT, in the identification of cancer stages. In fact, global architectural parameters are highly dependent on the VOI size and can be compared only on paired equal sized VOIs, while LNB and LNT maps can be used in qualitative comparisons to identify local regions with higher value of vascular trees and branches (fig. 5.3.A). On the other hand, early cancer stages exhibit substantially higher values of VVD compared to the reference, which fall severely in TP3 and TP4 (fig. 5.5) as soon as the tumor spreads. In the same way, significant differences between the reference

control VOI and three out of four tumor TPs are observed in LD, proving that it can help the detection of cancerous areas in almost every stage.

Finally, table 5.1 and fig 5.5 illustrate that tumor evolution can be characterized better by the tortuosity metrics: even if ICM identifies differences only between the reference and TP1 and TP4, DM adds a significant comparison with TP3 and SOAM values are significantly higher for all the TPs compared to the control area [11]. This result unveils the capability of tortuosity metrics to recognize cancer from the control region at different stages; in particular, SOAM metric has been proven to be the most reliable feature, among the computed seven and for this dataset, in the identification of cancer at any tumor TP.

5.5 Conclusion

In the present study, tumor vasculature in preclinical models investigated with 3-D Acoustic Angiography have been quantitatively analyzed by means of an automated strategy, partly inspired by previous findings in Chapter 4. The proposed strategy enables the objective description of tumor and control area, providing cut-off values for each parameter and malignancy grade at every stage.

In the future, 3-D parametric maps can offer a unique qualitative and quantitative evaluation to the clinician, becoming a ready-to-use technology in new generation CADx systems. Moreover, multi-features extraction can provide minable data useful for prognosis and cancers grow evolution in the worldwide population.

5.6 References

- [1] R. Gessner, M. Lukacs, M. Lee, E. Cherin, F. S. Foster, and P. A. Dayton, "High-resolution, high-contrast ultrasound imaging using a prototype dual-frequency transducer: in vitro and in vivo studies.," *IEEE Trans. Ultrason. Ferroelectr. Freq. Control*, vol. 57, pp. 1772–1781, 2010.
- [2] F. Molinari, A. Mantovani, M. Deandrea, P. Limone, R. Garberoglio, and J. S. Suri, "Characterization of Single Thyroid Nodules by Contrast-Enhanced 3-D Ultrasound," *Ultrasound Med. Biol.*, vol. 36,

- pp. 1616–1625, 2010.
- [3] C. Caresio, M. Caballo, M. Deandrea, R. Garberoglio, A. Mormile, R. Rossetto, P. Limone, and F. Molinari, “Optimized quantification of thyroid nodular vascularization from 3-D contrast-enhanced ultrasound images,” in *European symposium on Ultrasound Contrast Imaging*, 2017.
 - [4] S. F. Huang, R. F. Chang, W. K. Moon, Y. H. Lee, D. R. Chen, and J. S. Suri, “Analysis of Tumor Vascularity Using Ultrasound Images,” *IEEE Trans. Med. Imaging*, vol. 27, pp. 320–330, 2008.
 - [5] J. R. Eisenbrey, N. Joshi, J. K. Dave, and F. Forsberg, “Assessing algorithms for defining vascular architecture in subharmonic images of breast lesions,” *Phys. Med. Biol.*, vol. 56, pp. 919–930, 2011.
 - [6] P. A. Dayton, R. C. Gessner, L. Phillips, S. E. Shelton, K. Heath Martin, M. Lee, and F. S. Foster, “The implementation of acoustic angiography for microvascular and angiogenesis imaging,” in *2014 36th Annual International Conference of the IEEE Engineering in Medicine and Biology Society*, 2014, vol. 2014, pp. 4283–4285.
 - [7] D. H. Turnbull, J. A. Ramsay, G. S. Shivji, T. S. Bloomfield, L. From, D. N. Sauder, and F. S. Foster, “Ultrasound backscatter microscope analysis of mouse melanoma progression,” *Ultrasound Med. Biol.*, vol. 22, pp. 845–853, 1996.
 - [8] J. E. Chomas, R. E. Pollard, A. R. Sadlowski, S. M. Griffey, E. R. Wisner, and K. W. Ferrara, “Contrast-enhanced US of microcirculation of superficially implanted tumors in rats,” *Radiology*, vol. 229, pp. 439–446, 2003.
 - [9] N. Elie, A. Kaliski, P. Péronneau, P. Opolon, A. Roche, and N. Lassau, “Methodology for quantifying interactions between perfusion evaluated by DCE-US and hypoxia throughout tumor growth,” *Ultrasound Med. Biol.*, vol. 33, pp. 549–560, 2007.
 - [10] F. S. Foster, P. N. Burns, D. H. Simpson, S. R. Wilson, D. A. Christopher, and D. E. Goertz, “Ultrasound for the visualization and quantification of tumor microcirculation,” *Cancer Metastasis Rev.*, vol. 19, pp. 131–138, 2000.
 - [11] S. E. Shelton, Y. Z. Lee, M. Lee, E. Cherin, F. S. Foster, S. R. Aylward, and P. A. Dayton, “Quantification of Microvascular Tortuosity during Tumor Evolution Using Acoustic Angiography,” *Ultrasound Med. Biol.*, vol. 41, pp. 1896–1904, 2015.
 - [12] R. C. Gessner, C. B. Frederick, F. S. Foster, and P. A. Dayton, “Acoustic angiography: a new imaging modality for assessing microvasculature architecture,” *Int. J. Biomed. Imaging*, pp. 1–9, 2013.
 - [13] D. E. Kruse and K. W. Ferrara, “A new imaging strategy using wideband transient response of ultrasound contrast agents,” *IEEE Trans. Ultrason. Ferroelectr. Freq. Control*, vol. 52, pp. 1320–1329, 2005.
 - [14] B. D. Lindsey, J. D. Rojas, K. H. Martin, S. E. Shelton, and P. A. Dayton, “Acoustic characterization of contrast-to-tissue ratio and axial resolution for dual-frequency contrast-specific acoustic angiography imaging,” *IEEE Trans. Ultrason. Ferroelectr. Freq. Control*, vol. 61, pp. 1668–1687, Oct. 2014.
 - [15] B. A. Kamen, J. Glod, and P. D. Cole, “Metronomic therapy from a pharmacologist’s view,” *J. Pediatr. Hematol. Oncol.*, vol. 28, pp. 325–327, 2006.
 - [16] R. K. Jain, “Normalization of Tumor Vasculature: An Emerging Concept in Antiangiogenic Therapy,” *Science (80-.)*, vol. 307, pp. 58–62, 2005.
 - [17] J. Silvela and J. Portillo, “Breadth-First Search and Its Application to Image Processing Problems,” *IEEE Trans. Image Process.*, vol. 10, pp. 1194–1199, 2001.
 - [18] K. Meiburger, Y. Nam, E. Chung, L. J. Suggs, S. Y. and Emelianov, and F. Molinari, “Skeletonization algorithm-based blood vessel quantification using in vivo 3D photoacoustic imaging,” *Phys. Med. Biol.*, vol. 61, pp. 7994–8009, 2016.
 - [19] R. C. Gessner, S. R. Aylward, and P. A. Dayton, “Mapping microvasculature with acoustic angiography yields quantifiable differences between healthy and tumor-bearing tissue volumes in a rodent model,” *Radiology*, vol. 264, pp. 733–740, 2012.

- [20] S. R. Rao, S. E. Shelton, and P. A. Dayton, "The 'Fingerprint' of Cancer Extends Beyond Solid Tumor Boundaries: Assessment With a Novel Ultrasound Imaging Approach.," *IEEE Trans. Biomed. Eng.*, vol. 63, pp. 1082–1086, 2016.
- [21] S. R. Aylward and E. Bullitt, "Initialization, noise, singularities, and scale in height ridge traversal for tubular object centerline extraction," *IEEE Trans. Med. Imaging*, vol. 21, pp. 61–75, 2002.
- [22] E. Bullitt, G. Gerig, S. M. Pizer, W. Lin, and S. R. Aylward, "Measuring Tortuosity of the Intracerebral Vasculature from MRA Images," *IEEE Trans Med Imaging*, vol. 22, pp. 1163–1171, 2003.
- [23] A. Panfilova, S. Shelton, R. J. G. van Sloun, C. Caresio, H. Wijkstra, P. Dayton, and M. Mischi, "Which properties of the vascular architecture are reflected by dynamic contrast-enhanced ultrasound imaging of dispersion and wash-in rate? A comparison with acoustic angiography .," in *IEEE International Ultrasonics Symposium*, 2017, pp. 3–6.
- [24] A. F. Frangi, W. J. Niessen, K. L. Vincken, and M. a Viergever, "Multiscale vessel enhancement filtering," *Medial Image Comput. Comput. Intervention - MICCAI'98. Lect. Notes Comput. Sci. vol 1496*, vol. 1496, pp. 130–137, 1998.
- [25] T. Oruganti, J. G. Laufer, and B. E. Treeby, "Vessel filtering of photoacoustic images," in *SPIE 8581, Photons Plus Ultrasound: Imaging and Sensing*, 2013, vol. 85811W, pp. 1–10.
- [26] T. C. Lee, R. L. Kashyap, and C. N. Chu, "Building Skeleton Models via 3-D Medial Surface Axis Thinning Algorithms," *CVGIP Graph. Model. Image Process.*, vol. 56, pp. 462–478, 1994.
- [27] D. Hanahan and R. A. Weinberg, "Hallmarks of cancer: The next generation," *Cell*, vol. 144, pp. 646–674, 2011.
- [28] M. Potente, H. Gerhardt, and P. Carmeliet, "Basic and therapeutic aspects of angiogenesis," *Cell*, vol. 146, pp. 873–887, 2011.
- [29] J. Nagy, S. Chang, A. Dvorak, and D. HF., "Why are tumour blood vessels abnormal and why is it important to know?," *Br. J. Cancer*, vol. 100, pp. 865 – 869, 2009.
- [30] E. LaGory and A. Giacca, "The Ever Expanding Role of HIF in Tumour and Stromal Biology," *Nat Cell Biol*, vol. 18, pp. 356–365, 2014.
- [31] M. De Palma, D. Bizziato, and T. V. Petrova, "Microenvironmental regulation of tumour angiogenesis," *Nat. Rev. Cancer*, no. 8, pp. 457–474, 2017.
- [32] P. Bossi, G. Coggi, G. Viale, G. Viale, R. M. Alfano, A. K. C. Lee, A. K. C. Lee, and S. Bosari, "Angiogenesis in Colorectal Tumors: Microvessel Quantitation in Adenomas and Carcinomas with Clinicopathological Correlations," *Cancer Res.*, vol. 55, pp. 5049–5053, 1995.
- [33] J. E. Bluff, S. R. Menakuru, S. S. Cross, S. E. Higham, S. P. Balasubramanian, N. J. Brown, M. W. Reed, and C. A. Staton, "Angiogenesis is associated with the onset of hyperplasia in human ductal breast disease," *Br. J. Cancer*, vol. 101, pp. 666–672, 2009.

Conclusions and Final Remarks

As stated in the Introduction, scientific research and medical routine practice are continuously seeking for computer-aided schemes that can offer fast, non-invasive and reliable image-based diagnosis. Moreover, looking at the technological trends, future diagnostic procedure will be able to provide personalized medicine based on quantitative semantic and agnostic features, mineable high-dimensional data and prognostic models. Due to its portability, safety and convenience, huge investments are currently made on innovative ultrasound image technologies (such as 3-D/4-D/5-D, ultrafast and super-resolution imaging).

The aim of this work is to present a set of automated strategies in the field of ultrasound image-based diagnosis that can become the “bridge” groundbreaking technology between the state-of-art CADx and the extension of radiomics discipline to the ultrasound imaging.

The strategies proposed in this thesis are scalable, oriented to a wide range of applications, modalities, and dimensions and can effectively lead to the conversion of medical images into data. These automated strategies can provide quantitative and qualitative description of many complex anatomical structures, such as the texture pattern of a skeletal muscle or the 3-dimensional tortuosity parametric map of a tumor.

The work presented in this thesis can have a wide range of applications in clinical and preclinical practice: skeletal muscle ultrasound imaging and the related proposed strategies in architecture and morphology characterization can be applied in rehabilitation and sport medicine to faster the diagnosis process, providing real-time results and muscles progress/evolution. In the future, thyroid tumor assessment via quantitative 3-D CEUS and PDUS imaging can be extended to any other superficial tumors and introduced in cancer screening programs, being rapid, automatic and unexpansive. Acoustic Angiography and 3-D tumor vasculature reconstruction can be improved in future applications to better understand the cancer origin and evolution in other anatomical locations and models.

The automated strategies combine the human cognitive procedures of segmentation and recognition with image information revealed via quantitative high-dimensional features extraction, with the final aim to significantly improve patient's diagnosis, pathologies treatments, and prognosis.

APPENDIX A

Esaote Twice Ultrasound device settings

In the proposed studies, the MyLab™ Twice ultrasound device (Esaote, Genova, Italy) was equipped with a linear-array transducer (code LA533) with variable frequency 3-13 MHz. The gain was set to 50% of the range, dynamic image compression was turned off, and time gain compensation was maintained in the neutral position for all depths. All system-setting parameters were kept constant throughout the study and for each subject, except depth (initially set at 44 mm) that was modified during the examination (range: 44 -59 mm) to visualize the entire muscle thickness. The study was conducted at the Division of Endocrinology, Diabetology and Metabolism, Department of Medical Sciences, University of Turin and the same experienced user performed all the acquisitions. All images were visually inspected and analyzed by the same experienced operator.

APPENDIX B

Ultrasound procedure in skeletal muscle ultrasound imaging

Ultrasound B-mode images of the following five muscles were acquired in each subject during a single experimental session: biceps brachii, rectus femoris, vastus lateralis, tibialis anterior, and medial gastrocnemius. These superficial skeletal muscles have been chosen since they are the most informative in the assessment of neuromuscular disorders and sarcopenia.

The optimal representation of the different muscles was ensured complying with the following criteria: i) biceps brachii and tibialis anterior: we maximized the representation of the bone boundary and of the muscle fascicles ii) rectus femoris: we optimized the representation of the superficial and deep aponeuroses; iii) vastus lateralis and medial gastrocnemius: we optimized the representation of the superficial and deep aponeuroses and of the muscle fascicles.

Images of the medial gastrocnemius were acquired with the subjects in the prone position, whereas for all other muscles subjects were positioned supine.

In all measurements, the lower and upper limb joints were extended and the subject was asked to completely relax his/her muscles. Ultrasound coupling gel was used to ensure optimal image quality and to minimize the transducer pressure on the skin. All scans were performed by placing the transducer in correspondence of the largest muscle diameter at the following anatomical sites: the biceps brachii was measured at two-thirds of the distance from the acromion to the antecubital crease; the rectus femoris was measured half-way along the line from the anterior-superior iliac spine to the superior border of the patella; the vastus lateralis half-way along the line from the anterior-superior iliac spine to the superolateral border of the patella; the tibialis anterior at one-quarter of the distance from the inferior border

of the patella to the lateral malleolus; the medial gastrocnemius from the mid-sagittal line of the muscle, midway between the proximal and distal tendon insertions. For ultrasound scanning convention, the probe was placed in a way that the left part of the image was always pointing to the center of the subject body.

APPENDIX C

Agnostic texture features

First Order Statistic features

First Order texture features are extracted from the 1-D gray histogram of image luminance.

Feature	Description
Integrated Optical Density	$IOD = \sum_{x=1}^M \sum_{y=1}^N I(x, y)$
Mean Echo Intensity	$MEI = \sum_{x=1}^M \sum_{y=1}^N \frac{I(x, y)}{M \times N}$
Standard Deviation	$\sigma = \sqrt{\frac{\sum_{x=1}^M \sum_{y=1}^N [I(x, y) - m]^2}{M \times N}}$
Variance	$\sigma^2 = \frac{\sum_{x=1}^M \sum_{y=1}^N [I(x, y) - m]^2}{M \times N}$
Skewness	$S_k = \frac{1}{M \times N} \frac{\sum_{x=1}^M \sum_{y=1}^N [I(x, y) - m]^3}{\sigma^3}$
Kurtosis	$K_t = \frac{1}{M \times N} \frac{\sum_{x=1}^M \sum_{y=1}^N [I(x, y) - m]^4}{\sigma^4}$
Energy	$E_1 = \sum_{x=1}^M \sum_{y=1}^N I(x, y)^2$

Second Order Statistic Features (Haralick features)

Second Order Statistic Features (Haralick features) are based on the Gray Level Co-occurrence Matrix (GLCM). Let the image be represented by a $M \times N$ gray-scale matrix $I(x,y)$, where each element of the matrix indicates the intensity of a single pixel in the image. The co-occurrence matrix $C(i,j|\Delta x, \Delta y)$ is the second-order probability function estimation. This matrix denotes the rate of occurrence of a pixel pair with gray levels i and j , given the distances between the pixels are Δx and Δy in the x and y directions, respectively. The co-occurrence matrix $C(i,j|\Delta x, \Delta y)$ is defined as

$$C(i,j|\Delta x, \Delta y) = |\{(p, q), (p + \Delta x, q + \Delta y) : I(p, q) = i, I(p + \Delta x, q + \Delta y) = j\}|$$

where $(p, q)(p + \Delta x, q + \Delta y) \in M \times N$, $d = (\Delta x, \Delta y)$, and $|\cdot|$ denotes the cardinality of a set. The probability that a gray level pixel i is at a distance $(\Delta x, \Delta y)$ away from the gray level pixel j is given by

$$P(i,j) = \frac{C(i,j)}{\sum C(i,j)}$$

An element of the GLCM matrix (i, j, d, θ) is defined as the joint probability of the gray levels i and j separated by distance d and along angular direction θ . To reduce the computation burden, we have considered θ as 0° , 45° , 90° , and 135° , and d is defined as the Manhattan or city block distance (i.e. the number of pixels that must be crossed) based on this GLCM. These second order features are mathematically defined in the following table.

Feature	Description
Symmetry	$I_{sym} = \sum_{i=0}^{N-1} \sum_{j=0}^{N-1} i - j P(i, j)$
Contrast	$I_{con} = \sum_{n=0}^{N-1} n^2 \left\{ \sum_{i=0}^{N-1} \sum_{j=0}^{N-1} P(i, j) \right\}$
Homogeneity	$I_{hmg} = \sum_{i=0}^{N-1} \sum_{j=0}^{N-1} \frac{1}{1 + (i - j)^2} P(i, j)$
Entropy	$I_{Entr} = - \sum_{i=0}^{N-1} \sum_{j=0}^{N-1} P(i, j) \log(P(i, j))$
Energy	$I_{Enrg} = \sum_{i=0}^{N-1} \sum_{j=0}^{N-1} P(i, j)^2$
Correlation	$I_{cor}^* = \frac{\sum_{i=0}^{N-1} \sum_{j=0}^{N-1} P(i, j) P(i, j)^2 - \mu_x \mu_y}{\sigma_x \sigma_y}$

* $\sigma_x, \sigma_y, \mu_x, \mu_y$ are the standard deviations and means of P_x, P_y which are the partial probability density functions. $p_x(i) = i^{th}$ entry in the marginal-probability matrix obtained by summing the rows of $P(x, y)$.

High-order Statistic Features (Galloway features)

High-order texture Statistic features (Galloway features) are based on the run length matrix (RLM) R . In a RLM, the pixel $R(i, j)$ contains the number of pixels with run length j and intensity i in a given direction. The RLM has a number of rows equal to the number of gray levels in the image and a number of columns equal to the maximum length of the run length. Mathematical description of the Galloway features. N_g represents the number of gray values in the image (i.e. the number of rows of the matrix R). N_r represents the number of runs (i.e. the number of columns of the R matrix).

Feature	Description
Short Run Emphasis	$SRE = \frac{\sum_{i=1}^{N_g} \sum_{j=1}^{N_r} \frac{R(i, j)}{j^2}}{\sum_{i=1}^{N_g} \sum_{j=1}^{N_r} R(i, j)}$
Long Run Emphasis	$LRE = \frac{\sum_{i=1}^{N_g} \sum_{j=1}^{N_r} j^2 R(i, j)}{\sum_{i=1}^{N_g} \sum_{j=1}^{N_r} R(i, j)}$
Gray Level Non-Uniformity	$GLNU = \frac{\sum_{i=1}^{N_g} (\sum_{j=1}^{N_r} R(i, j))^2}{\sum_{i=1}^{N_g} \sum_{j=1}^{N_r} R(i, j)}$
Run Length Non-Uniformity	$RLNU = \frac{\sum_{j=1}^{N_r} (\sum_{i=1}^{N_g} R(i, j))^2}{\sum_{i=1}^{N_g} \sum_{j=1}^{N_r} R(i, j)}$
Run Length Percentage	$RP = \frac{\sum_{i=1}^{N_g} \sum_{j=1}^{N_r} R(i, j)}{N_g N_r}$

Local Binary Pattern features

The LBP is computed by using the following method:

A circular neighborhood of radius R pixels is considered around a pixel. The pixel is the center of the circular neighborhood and it has intensity equal to I_c .

P points are chosen on the circumference of the circle with radius R such that they are all equidistant. Let $I_p (P = 1, \dots, P)$ be the intensities of the P points on the circumference.

These P pixels are converted into a circular bit-stream of zeros and ones according to whether the gray value of the pixel is less than or greater than I_c .

We considered P equal to 24 pixels and R equal to 3 pixels, in order to consider a relatively large neighborhood. The created neighborhood is then assigned with a uniformity measurement U that counts the number of bit transitions (from 0 to 1 and viceversa) in the circular domain (with reference to fig. 3, the U value would be equal to 4). We assigned to the LBP code only the patterns with $U \leq 2$, so that:

$$LBP(x) = \begin{cases} \sum_{p=1}^P s(I_p - I_c) & U(x) \leq 2 \\ P + 1 & otherwise \end{cases}$$

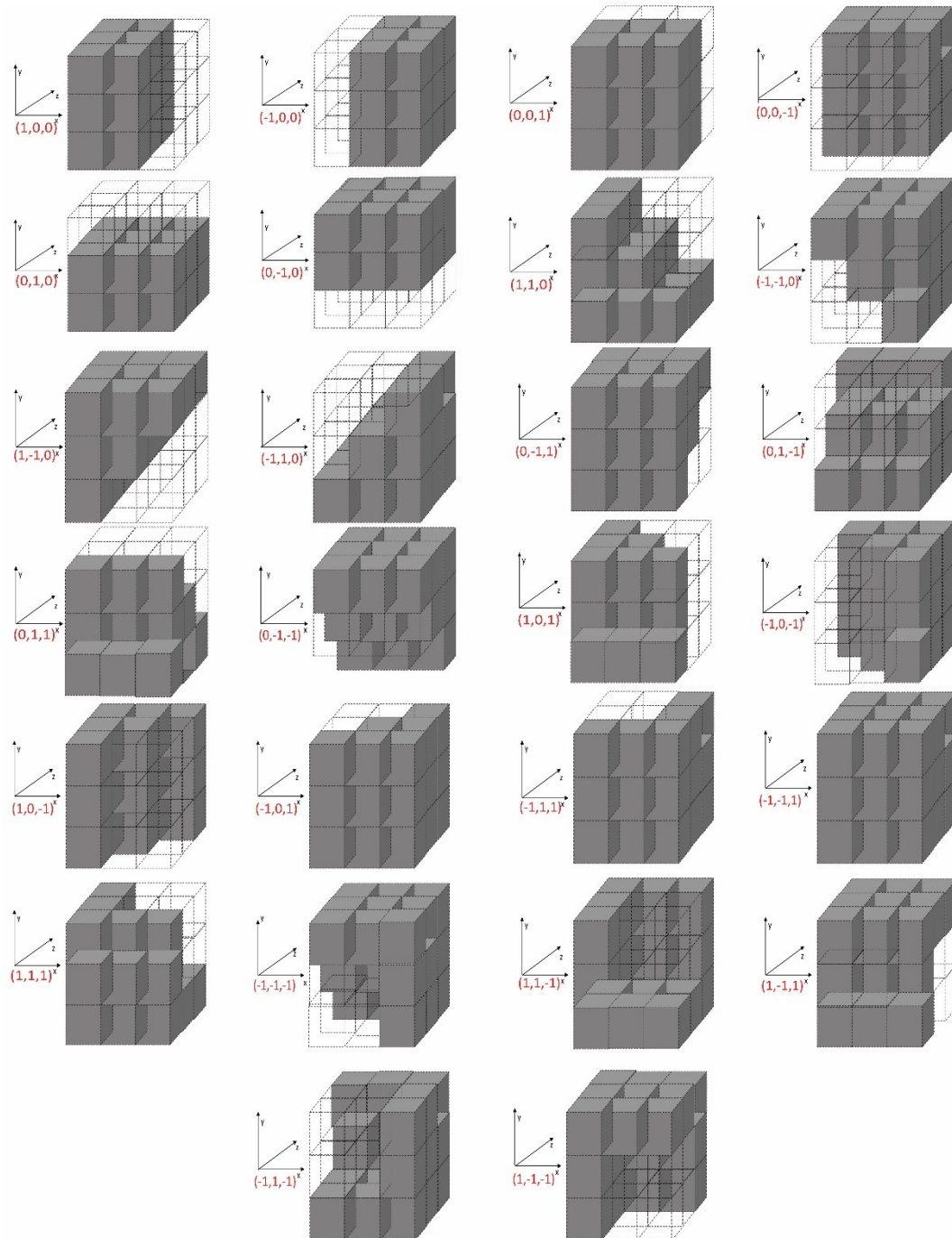
where $s(x)$ is the step function that equals 1 if $x \geq 0$ and is null for $x < 0$. Let's f_i be the relative frequency of the histogram derived from the LBP values of all the image pixels. The LBP energy is defined as:

$$LBP_{energy} = \sum_i f_i^2$$

The LBP entropy can be defined as:

$$LBP_{entropy} = - \sum_i f_i \cdot \log_2(f_i)$$

APPENDIX D



APPENDIX E

Vascular features extraction

The computation of vascular parameters is performed applying an iterative procedure which can isolate vascular trees T according to the position of the nodes:

$$CTree = \{ T_1, T_2, \dots, T_N \}$$

where N is the number of vascular trees.

The vascular architecture parameters are:

1. Number of vascular Trees (NT), which is the number of the vascular networks of the tumor. Since $CTree = \{ T_1, T_2, \dots, T_N \}$ denotes the set of all vascular trees, then

$$NT = N .$$

2. Number of vascular Branches (NB), which takes into the number of branches of the tumor vascular pattern; they are identified by branchpoints.
3. Vascular Volume Density (VVD), which is obtained by the ratio of the total space occupied by the blood vessels and the total tumor size.

Considering each vascular tree T_i as the sequence of m nodes $T_i = \{p_1, p_2, \dots, p_m\}$, the tortuosity metrics are:

4. Distance Metric (DM), which computes the ratio of the length of the vessel and the linear Euclidean distance between its endpoints:

$$DM = \frac{|p_m - p_1|}{\sum_{k=1}^{m-1} |p_{kk} - p_{k+1}|}.$$

This is the simplest tortuosity metric and in case of a perfectly straight vessel the DM value is 1, while it increases as much as the vessel curves. It is suitable for slowly curving vessels which do not change direction along their path.

5. Inflection Count Metric (ICM), which is obtained by the product of the number of inflection points N_{InfP} and the DM, plus 1 (in case of a curve which does not change its curvature direction, the ICM value would be equal to 1):

$$ICM = DM * N_{InfP} + 1.$$

The N_{InfP} value is obtained using the geometrical representation of the Frenet frame. Along the centerline path, each point p_i is considered, in a way that p_{k-1} and p_{k+1} are the neighboring nodes. Defining the velocity vector $\vec{V} = p_{k+1} - p_{k-1}$ and the acceleration vector $\vec{A} = \vec{T}_2 - \vec{T}_1$, where $\vec{T}_1 = p_k - p_{k-1}$ and $\vec{T}_2 = p_{k+1} - p_k$, the principal normal vector \vec{N} can be expressed as

$$\vec{N} = \frac{\vec{V} \times \vec{A} \times \vec{V}}{|\vec{V} \times \vec{A} \times \vec{V}|}$$

An inflection point can be recognized if $\Delta\vec{N} \cdot \Delta\vec{N} > 1$, where $\Delta\vec{N}$ represents the difference of the normal axes \vec{N} associated with point p_k and p_{k+1} .

This parameter is an estimation of the average number of time the vascular tree changes its shape from convex to concave and vice-versa. It is particularly suitable for vessels with high-frequency and high-amplitude curvature changes (inflection points).

6. Sum Of Angles Metric (SOAM), which computes and sums point by point along the vessel's centerline the total curvature angles. This metric is suitable in case of tortuous high-frequency and low-amplitude coils. As before, for

any point p_k , \vec{T}_1 , \vec{T}_2 and $\vec{T}_3 = p_{k+2} - p_{k+1}$ are defined. The in-plane angle at point p_k (IP_k) and the torsion angle TP_k are given by the following equations:

$$IP_k = \cos^{-1} \left(\frac{\vec{T}_1}{|\vec{T}_1|} \cdot \frac{\vec{T}_2}{|\vec{T}_2|} \right)$$

$$TP_k = \cos^{-1} \left(\frac{\vec{T}_1 \times \vec{T}_2}{|\vec{T}_1 \times \vec{T}_2|} \cdot \frac{\vec{T}_2 \times \vec{T}_3}{|\vec{T}_2 \times \vec{T}_3|} \right)$$

The total angle CP_k at point P_k is then

$$CP_k = \sqrt{(IP_k \times IP_k) + (TP_k \times TP_k)}$$

The SOAM metric calculates the total tortuosity of the curve as

$$SOAM = \frac{\sum_{k=1}^{n-3} CP_k}{\sum_{k=1}^{n-1} |p_k - p_{k-1}|}$$

List of Contributions

Journal Articles

- [1] C. Caresio, F. Molinari, G. Emanuel, M.A. Minetto, **Muscle echo intensity: reliability and conditioning factors.**, *Clin. Physiol. Funct. Imaging*, 2015; 35: 393–403.
- [2] F. Molinari, C. Caresio, U.R. Acharya, M.R.K. Mookiah, M.A. Minetto, **Advances in Quantitative Muscle Ultrasonography Using Texture Analysis of Ultrasound Images.**, *Ultrasound Med. Biol.*, 2015; 41: 2520–2532.
- [3] M.A. Minetto, C. Caresio T. Menapace, A. Hajdarevic, A. Marchini, F. Molinari, N.A. Maffiuletti, **Ultrasound-Based Detection of Low Muscle Mass for Diagnosis of Sarcopenia in Older Adults.**, *PM&R*, 2016; 8: 453–462.
- [4] C. Caresio, M. Salvi, F. Molinari, K.M. Meiburger, M.A. Minetto, **Fully Automated Muscle Ultrasound Analysis (MUSA): Robust and Accurate Muscle Thickness Measurement.**, *Ultrasound Med. Biol.*, 2017; 43: 195–205.
- [5] M. Giacchino, C. Caresio, N.E. Gorji, F. Molinari, G. Massazza, M.A. Minetto, **Quantitative analysis of patellar tendon size and structure in asymptomatic professional players: sonographic study.** *Muscle, Ligaments and Tendons Journal*, accepted for publication, 2017.
- [6] M.A. Minetto, C. Caresio, V. D'Angelo, F. Lanfranco, L. Ghizzoni, S. Roatta, E. Arvat, S. Kesari, **Diagnostic work-up in steroid myopathy: case study.** submitted to *Endocrine Research*, 2017.
- [7] R.J.G. van Sloun, L. Demi, S.G. Schalk, C. Caresio, J. Huang, J. Li, A. Postema, C. Mannaerts, F. Molinari, J.C. van der Linden, P. Huang, H. Wijkstra, M. Mischi, **In-vivo contrast-enhanced ultrasound tractography.**, submitted to *Nature Biomedical Engineering*, 2017.
- [8] M.A. Minetto, C. Caresio, V. D'Angelo, N.E. Gorji, F. Molinari, G. Arnaldi, S. Kesari, E. Arvat, **Ultrasound-based detection of glucocorticoid-induced impairments of muscle mass and structure in Cushing's disease.**, paper in preparation.
- [9] M.A. Minetto, G. Gamberro, G. Gays, S. Vigo, C. Caresio, N.E. Gorgji, G. Massazza, **Effectiveness of an innovative mattress overlay for improving rehabilitation in low back pain: a pilot randomized controlled study.**, paper in preparation.

- [10] C. Caresio, M. Caballo, M. Deandrea, R. Garberoglio, R. Mormile, R. Rossetto, P. Limone, F. Molinari, **Analysis of thyroid tumor vascularity: A quantitative comparison between 3-D Contrast-Enhanced Ultrasound and 3-D Power Doppler for the differential diagnosis of benign and malignant thyroid nodules.**, paper in preparation.
- [11] A. Panfilova, S. Shelton, C. Caresio, F. Molinari, P. Dayton, M. Mischi, **On the relationship between dynamic contrast -enhanced ultrasound features and the underlying vascular architecture extracted from acoustic angiography.**, paper in preparation.

Conference papers and oral presentations

- [12] C. Caresio, M. Caballo, F. Molinari, **Quantitative analysis and optimized rendering of 3-D Cancer Vascular Patterns.**, *Enabling Technologies in 3-D Cancer Organoids*, March 8th-9th, 2016, Molecular Biology Center, Turin.
- [13] C. Caresio, **Optimized assessment of thyroid nodules vascularization from 3-D multimodal ultrasound images.**, *Dutch Society of Medical Ultrasound*, November 2nd, 2016, Radbound University, Nijmegen Medical Center, Nijmegen, The Netherlands.
- [14] C. Caresio, M. Caballo, M. Deandrea, R. Garberoglio, R. Mormile, R. Rossetto, P. Limone, F. Molinari, **Optimized quantification of thyroid nodular vascularization from 3-D contrast enhanced ultrasound images.**, *The 22nd European Symposium on Ultrasound Contrast Imaging*, January 19-20th, 2017, Rotterdam, The Netherlands.
- [15] C. Caresio, C. Blank, N.P.M. Kuijsters, F. Sammali, M. Mischi, F. Molinari, B.C. Schoot, **Objective assessment of uterine peristalsis outside pregnancy by high-order texture analysis of ultrasound images.**, *27th World Congress on Ultrasound in Obstetrics and Gynecology*, September 16-19th 2017, Vienna, Austria.
- [16] A. Panfilova, S. Shelton, R.J.G. van Sloun, C. Caresio, H. Wijkstra, P. Dayton, M. Mischi, **Which properties of the vascular architecture are reflected by dynamic contrast-enhanced ultrasound imaging of dispersion and wash-in rate? A comparison with acoustic angiography.**, *IEEE Proceedings IUS 2017*, September 6-9th, 2017 Washington, D.C., USA.